University of South-Eastern Norway
Faculty of Technology, Natural Sciences and Maritime Studies

Doctoral dissertation no. 49
2019

Laxma Reddy Billa

Simulation and microfabrication of MEMS vacuum electronic devices for terahertz technology

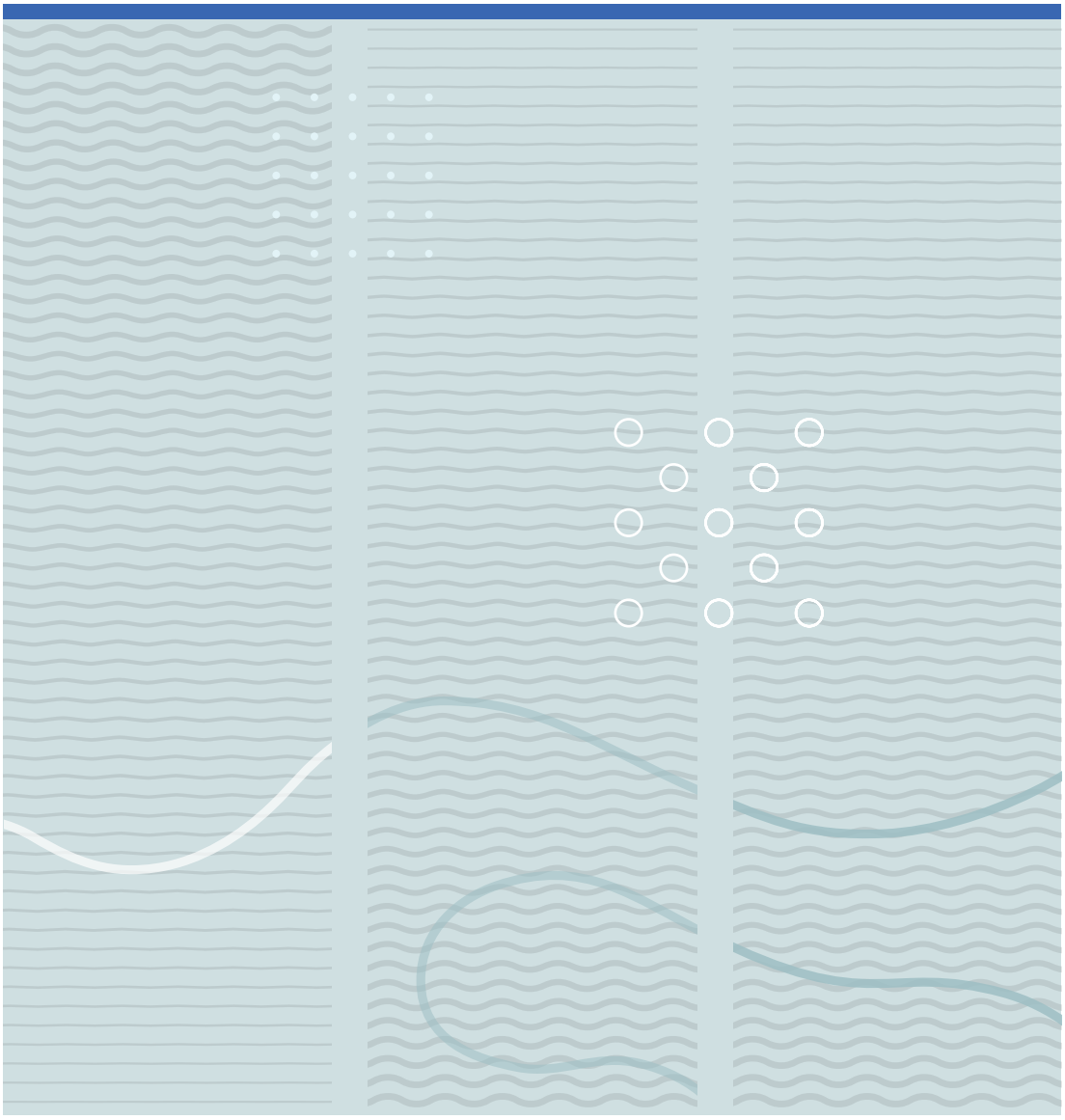

Laxma Reddy Billa

Simulation and microfabrication of MEMS vacuum electronic devices for terahertz technology

A PhD dissertation in
Applied Micro- and Nanosystems

© Laxma Reddy Billa 2019

Faculty of Technology, Natural Sciences and Maritime Studies
University of South-Eastern Norway
Horten, 2019

Doctoral dissertations at the University of South-Eastern Norway no. 49

ISSN: 2535-5244(print)
ISSN: 2535-5252 (online)

ISBN: 978-82-7860-398-7 (print)
ISBN: 978-82-7860-399-4 (online)

This publication is licensed with a Creative Commons license. You may copy and redistribute the material in any medium or format. You must give appropriate credit, provide a link to the license, and indicate if changes were made. Complete license terms at https://creativecommons.org/licenses/by-nc-sa/4.0/deed.en

Print: University of South-Eastern Norway

Dedicated to my beloved parents, brother, sister, brother-in-law and sister-in-law for their love, trust and motivations

Preface

This thesis is submitted in partial fulfilment of the requirements for the degree of Philosophise Doctor from Department of Microsystems Technology at University of South-Eastern Norway.

This doctoral work has been conducted at the Department of Microsystems Technology (IMST), Faculty of Technology and Maritime Science, University of South-Eastern Norway, Horten, Norway, under the supervision of Professor Xuyuan Chen and Professor Muhmmud Nadeem Akram.

Financial support was provided by the Ministry of Education, Norway. The Research Council of Norway is acknowledged for the support to the Norwegian Micro- and Nano-fabrication facility, NorFab (245963/F50) and the Norwegian Ph.D. Network on Nanotechnology for Microsystems, Nano-Network (221860/F40).

Acknowledgements

First of all, I would like to express my appreciation and sincere gratitude to my supervisors, Professor Xuyuan Chen and Professor Nadeem Akram for guidance and support throughout my PhD research. Their advice and encouragement have been valuable for the success of my PhD work.

I would like to thank my colleagues at USN for a meaningful contribution to my PhD work. Thanks also to lab engineers: Zekija Ramic, Muhmmad Tayib, Antuan, Rangnar Dahl Johanseen, Thomas Martisen for their support in the laboratory.

The Norwegian research council is thankfully acknowledged for the financial support for this PhD work. The Norwegian PhD Network on Nanotechnology for the Microsystems is also deeply acknowledged for grating travel support to international conferences and the laboratory fee.

I would like to thank the department of Microsystem technology for giving me the opportunities for performing this work, the thank to Kristin Skjold Granerød and Aina Enstad for their support with administration work.

Finally, I would like to thank my family and friends for their support, understanding and encouragement during these years.

Abstract

Keywords: Terahertz, Millimetre-wave, Vacuum electron technology, Slow-wave structure, Traveling wave tube, Microfabrication

Numerous applications explore the scarcely used terahertz (THz) band in the electromagnetic spectrum. However, widespread utilization of the THz band is technically challenging, due to the lack of power sources. The power level of the signal generators drastically drops as the frequency approaches the THz frequencies. Moreover, at this frequency range, the attenuation level of electromagnetic waves in the earth atmosphere increases. In vacuum electronics family, traveling wave tube (TWT) has gained particular interest for millimetre-wave and THz signal amplification for high-power and wideband applications. The characteristics of the TWT are mainly represented by the performance of a slow-wave structure (SWS). The SWS in TWT is used to facilitate the input THz signal which gets amplified by the process of the beam-wave interaction. Therefore, an efficient and reliable SWS is an essential aspect of a powerful TWT design.

This thesis proposes a novel SWS, which consists of metal corrugations in the H-plane and E-plane of the rectangular waveguide operated in the fundamental mode. The concept of H-plane and E-plane load shows potential benefits to the THz TWTs, such as excellent linear characteristics, an increased interaction impedance, ultra-wide bandwidth, and high-power output. Furthermore, the geometry of the SWS made the fabrication easier by using the available microfabrication techniques. The thesis involves all elements of development from device design, simulations, through material growth and interactive device fabrication to extensive characterization, along with the prototype cold-testing of the scaled-up device.

The proposed SWS is investigated for TWT working at 400 GHz central frequency. The design and simulation of TWT involve three stages, which are high frequency electromagnetic study of a unit cell of the SWS using Eigenmode simulations, scattering parameters or S-parameters analysis of coupler design with the SWS using

time-domain transient simulations, and beam-wave interaction study using particle-in-cell (PiC). The PiC simulations found that this tube can produce an excess of 25 dB small-signal gain with 60 GHz 3-dB bandwidth at 400 GHz central frequency. The LIGA technique was employed to fabricate the 400-GHz E-plane and H-plane loaded SWS. In particular, the KMPR negative tone photoresist was used in the fabrication process. The KMPR mold produced the nearly perfect features of the mask designs, tolerance within the ±2.5 μm of the lateral features and maximum deviation of 2^0 in the vertical profiles. The experiments for surface roughness study revealed that the interior sidewall roughness of the LIGA-fabricated metal parts was achieved about 20 nm. A diffusion bonding method was employed to attach the two LIGA-fabricated copper parts of the SWS, producing a bonding strength of 25 MPa at 400 ^{0}C bonding temperature and with a void-free bonding interface.

A scale-up model of the H-plane and E-plane SWS together with input and output couplers at W-band (85-110 GHz) was designed, manufactured using CNC milling, and verified the electromagnetic characteristics experimentally. The test results of S-parameters agreed with the simulations, S_{11}<-15 dB over a frequency range of 85 GHz - 98 GHz. PiC simulations were also performed to the 93.5-mm length SWS, demonstrating a gain about 24 dB over 89 GHz – 101 GHz. To mitigate the diocotron instability in the sheet-beam transmission, a modified geometry of the sheet beam was employed and analysed through PiC simulations. The robust design and high performance from the H-plane and E-plane loaded SWS suggests that this is a promising candidate for high-power and wideband TWT development in the millimetre and THz frequency ranges.

List of papers

Papers omitted from the online publication due to publisher's restrictions

The thesis includes the following articles

1. **H-plane and E-plane loaded rectangular slow-wave structure for terahertz TWT amplifier,** Laxma Reddy Billa, Muhammad Nadeem Akram and Xuyuan Chen, IEEE Transactions on Electron Devices, Vol. 63, 2016.

2. **Improved design and microfabrication of H-plane and E-plane loaded rectangular slow-wave structure for THz amplifier** Laxma Reddy Billa, Xianbao Shi, Muhammad Nadeem Akram and Xuyuan Chen, IEEE Transactions on Electron Devices, Vol. 64, 2017

3. **UV-LIGA microfabricated THz slow-wave structures for vacuum electronics devices using KMPR photoresist,** Laxma Reddy Billa, Muhammad Nadeem Akram and Xuyuan Chen, IOP Journal of Micromechanics and Microengineering. (manuscript submitted).

4. **H- and E-plane loaded slow-wave structure slow-wave structure for W-band TWT,** Laxma Reddy Billa, Muhammad Nadeem Akram, Claudio Paoloni, and Xuyuan Chen, IEEE Transactions on Electron Devices. (manuscript accepted)

The following articles are conference proceedings

1. **Novel rectangular slow-wave circuit for terahertz traveling wave tubes,** Laxma Reddy Billa, Muhammad Nadeem Akram and Xuyuan Chen, 8th UK, Europe, China Millimeter Waves and THz Technology Workshop (UCMMT), in the UK, 2015.

2. **Modified corrugated rectangular slow-wave structure for terahertz traveling wave tube amplifier,** Laxma Reddy Billa, Xianbao Shi, Muhammad Nadeem Akram and Xuyuan Chen, IEEE International Vacuum Electronics Conference (IVEC), in USA, 2016.

3. **E-plane bending input/output coupler in staggered double vane TWT amplifier,** Xianbao Shi, Laxma Reddy Billa, Muhammad Nadeem Akram and Xuyuan Chen, IEEE International Vacuum Electronics Conference (IVEC), in USA, 2016.

4. **COMSOL Multiphysics modeling and simulation of traveling wave tube amplifier,** Laxma Reddy Billa, Muhammad Nadeem Akram and Xuyuan Chen, 8th UK, Europe, China Millimeter Waves and THz Technology Workshop (UCMMT), in China, 2016.

5. **MEMS fabrication of H-plane and E-plane loaded 400 GHz TWT amplifier,** Laxma Reddy Billa, Xianbao Shi, Muhammad Nadeem Akram and Xuyuan Chen, IEEE International Vacuum Electronics Conference (IVEC) , in the UK, 2017.

6. **Cold-test analysis of H-plane and E-plane loaded rectangular slow-wave structure,** Laxma Reddy Billa, Muhammad Nadeem Akram and Xuyuan Chen, 8th UK, Europe, China Millimeter Waves and THz technology Workshop (UCMMT), in the UK, 2017.

Papers summary

1. H-plane and E-plane loaded rectangular slow-wave structure for TWT amplifier

In this paper, a novel miniaturized rectangular slow-wave structure (SWS) is proposed for sub-millimetre or THz vacuum electron traveling wave tube (TWT) amplifier. The SWS is composed of both H-plane and E-plane corrugations in the rectangular waveguide. The advantage of this SWS was investigated using three-dimensional (3D) simulators. The SWS permits design flexibility to achieve wider bandwidth, high output power, and easy fabrication by utilizing the available microfabrication techniques. The preliminary particle-in-cell (PiC) simulations have shown promising TWT amplifier performance such as 80 GHz instantaneous bandwidth, the maximum gain of 19.5 dB at 400 GHz for a defined moderate beam voltage of 17 kV and 20 mA beam current. The large-signal simulations have predicted a saturated output power of 19.3 W for 400 GHz CW excitation.

Author contribution:
Literature review, device proposal, investigation of the proposed device, simulations, analysis of the results and manuscript preparation.

2. Improved design and microfabrication of H-plane and E-plane loaded rectangular slow-wave structure for THz TWT

This paper explains the design optimization of the H-plane and E-plane loaded SWS for 400-GHz TWT. An improved coupler was devised in order to enable the same LIGA process used for fabricating the SWS as well as for utilizing the full intrinsic bandwidth of the SWS. The coupler showed excellent impedance wave matching characteristics and a low reflection coefficient, S11 < -15 dB over a frequency range of 360 GHz –460 GHz. By implementing the phase velocity tapering technique, an increase of 60% in the saturated output power across the 80 GHz instantaneous bandwidth was achieved. The study of fabrication tolerance of the individual geometrical parameters on the device performance was studied in detail. The feasibility of KMPR UV-LIGA technique was verified through preliminary fabrication runs.

Author contribution:

Literature review, design and simulations, analysis of the results, device fabrication and characterization, and manuscript preparation.

3. UV-LIGA microfabricated THz slow-wave structure for vacuum electronics devices using KMPR photoresist

A negative tone photoresist KMPR was used as mold material in the device fabrication using UV-LIGA technique, for easing the removal of mold. A customized UV-LIGA process was proposed, whose critical process parameters were optimized to achieve a high structural quality. An optical microscope and scanning electron microscope (SEM) analysis showed that the dimensional accuracy of copper metal structures is less than 2 μm and sidewall verticality is $90^0 \pm 1^0$. From the surface roughness study, it was revealed that a sidewall surface roughness of copper metal structure of about 20 nm was achieved, which met the desired electromagnetic propagation property (skin-depth) in the THz devices. Homogenous and excellent bonding mechanism between the copper-copper interface of the SWS parts was achieved, with the bonding strength of about 12 MPa at 400 ˚C bonding temperature.

Author contribution:

Literature review, process flow design, process parameter optimization, device characterization and analysis and manuscript preparation.

4. H- and E-plane loaded Slow-wave structure for W-band TWT

For fast verification of the design concept of the proposed SWS for the THz TWTs, a scale-up model was designed at W-band. The scaled device was manufactured using advanced CNC milling. The test results of S-parameters agreed with the simulations, S_{11}<-15 dB over a frequency range of 91 GHz – 98 GHz and showed a very good electromagnetic propagation characteristics. The PiC simulations demonstrated the W-band TWT using the H-plane and E-plane loaded SWS, predicting a gain of 24 dB over 91 GHz – 98 GHz, for given 85-periods length SWS. The prototype device showed that the

proposed SWS, H-plane and E-plane loaded SWS, a viable alternative for high-power and wideband millimetre-wave and THz TWT development.

Author contribution:

Literature review, design and simulations, device S-parameters measurements, analysis of the results and manuscript preparation.

Table of contents

Chapter 1

Introduction

1.1 Motivation

In recent years the study and research on signal sources in the terahertz (THz) region of the electromagnetic spectrum have surged [1, 2]. The THz region is roughly defined in the electromagnetic spectrum ranging from 100 GHz to 10 THz, which is between the technological domains of electronics and photonics [2]. In terms of the wavelength, it corresponds to the range of 3 mm - 0.03 mm. The interest is due to the unique properties of the THz radiation that led to a wide range of applications in military and commercial systems. Those properties are listed below:

- Penetration— THz signals penetrate non-metallic and non-polarizing materials such as semiconductors, textiles and plastics. This helps to reveal hidden objects inside these materials [3, 4].
- High-resolution imaging— imaging systems operating THz regions can provide better spatial resolutions and image qualities than the imaging systems at microwave regions [4, 5].
- Spectroscopy— plenty of materials exhibit their spectral characteristics in the THz domain, among them being semiconductors, ferroelectrics, dielectrics, high-temperature superconductors, gases and liquids [6, 7].
- Non-ionization— THz radiation is nonionizing in contract to the ionizing radiation by X-ray, and it can penetrate through skin, hair, teeth or dried biological samples. Hence, biological tissues and genetics can be monitored by THz signal in medical imaging application for detection of infected tissues [8, 9]. However, the deep penetration of THz radiation inside the body due to the water content in any cell is very poor.

- Less scattering—due to the longer wavelength of the THz signals compared to visible light, the THz signals allows the visualization of objects in granular materials.
- Intensity— THz signals are much easier to focus and collimate than radio waves.

During the 1980s and 1990s, sensing and imaging were the leading applications in the field of spectroscopy [10] and radio astronomy [11] as they utilized the THz signals. Since then, revolutionary advancements in the THz device development that pave the way for attractive applications extended from fundamental science to real-world applications in different sectors, such as semiconductor, medical, manufacturing, defence, wireless communications, agriculture and many other industries. For most applications, this usually involves the transmission and detection of signals in free space in either a short range or a medium range. However, the attenuation of the electromagnetic waves in the earth atmosphere and scattering from atmospheric particulates are serious obstacles that prevent extensive usage of the THz spectrum [12]. Figure 1.1 shows that the specific transmission windows in which the spectrum exhibits with minimum attenuation, are roughly located at 140 GHz, 300 GHz, 350 GHz, 410 GHz, 670 GHz, and 850 GHz. The atmospheric attenuation varies under different weather conditions. The level of attenuation raises as the frequency moves from the low-frequency band to the higher end of the spectrum. The high degree of attenuation, as approaching the higher frequency bands, imposes a challenge in exploring THz band for applications that need propagation over a longer distance.

Currently, the THz sources which are commercially available are, either developed by using solid-state technology or photonics technology. The family of III-V semiconductor materials (for example, GaN, InP and GaAs) which are used to develop powerful monolithic integrated circuit (MMIC) power amplifiers for generating RF signals in the lower end of the THz spectrum [13]. The wide-bandgap

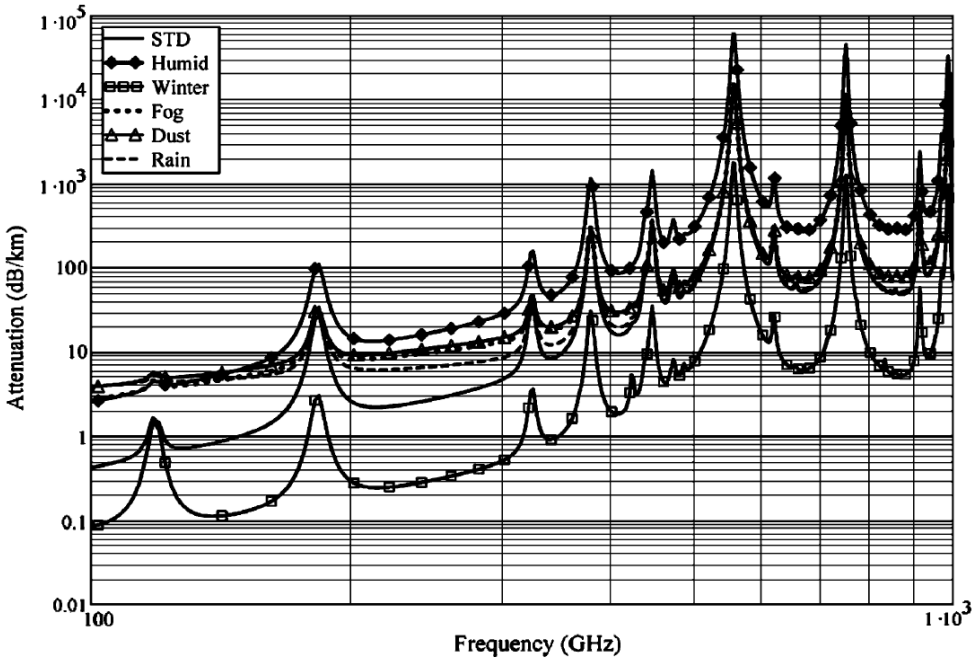

Figure 1.1: Atmospheric attenuation of electromagnetic waves in the THz spectrum [12].

semiconductors materials offer a high breakdown voltage and low mean carrier velocity. InP HBT and GaN HEMT can produce approximately 1 W saturated output power at 100-GHz [14]. Gunn diodes using GaN and GaAs are proved high power signal sources in the microwave band, which works on the principle of negative differential resistance [15, 16]. This can generate a few hundreds of mW around 100 GHz. However, if the number of power modules is increased and connected in cascaded to enhance the output power levels of the solid-state power amplifier, the device performance deteriorates with the thermal management.

Nevertheless, the operating frequency beyond 300-GHz, solid-state signal sources suffer from short transit-time, resistance-capacitance effect, and the presence of spurious signals from harmonic frequencies which arise from multiplied sources. These drawbacks limit the available power capability well below the milliwatt-level and only offer a very narrow bandwidth [17].

Quantum cascade lasers (QCL), comprises of a series of thin layers of GaAs/AlGaAs heterostructures and, can also be used for generating THz radiation. Although the

advancement shown in this field, is still required to operate at cryogenic temperatures (for example,199.5 K), which is a serious drawback of this technology [18].

An encouraging technique is nonlinear photo-mixing in which the different wavelength of lasers is mixed and down-converted to the wavelength of THz radiation. The main disadvantages of the photo-mixing technique, for frequencies below 1 THz, are low output power, very low conversion efficiency and a bulky optical system [19]. This is due to a lack of reliability, compactness, and high cost, the category of THz signal sources available until now, which have deprived the full-fledged utilization of THz region for innovative application areas.

The most promising and established technology for high power electromagnetic signal generators is vacuum electronic tubes [20]. Historically, these devices were developed in the microwave band, mainly for space and military applications. For high power applications, the vacuum electronic tubes have been found to have an excellent thermal management system and a high-power handling capability over solid-state technology. Therefore, a good approach is to realize the compact THz signal generators or amplifiers by promoting the operation frequency of existing vacuum electron devices in the microwave to THz frequencies [21, 22]. Thereby the vacuum electronics-based THz sources can offer a much higher power and broader bandwidth than other counterparts. In vacuum electronics technology, the parts of the tube must be scaled with the wavelength of the operating frequency. Therefore, according to the physical scaling law, the critical features of the vacuum tube's parts must be in the range of hundreds of millimetres to tens of microns in the THz frequency range. The miniaturised parts demand stringent dimensional accuracy and a very tight alignment for assembly. Furthermore, the Ohmic loss, due to the surface currents in the SWS, increases rapidly as the frequency approaches THz frequency band [23, 24]. This is due to RF currents passing through on the surface of skin-depth, proportional to $1 / \sqrt{(frequency\text{^}2)}$. Hence the surface quality of the SWS should be within a fraction of skin-depth, for example, the skip depth at 220 GHz is 120nm. Conventional milling techniques are the main obstacle to realizing THz tube parts. To deal with these issues, the application of

microfabrication techniques shows the possible solutions for manufacturing the miniaturized THz tube parts. In recent years research advancement in THz vacuum devices have encouraged the scientific community to develop robust and affordable THz systems [1].

1.2 THz traveling wave tube

In vacuum electronics technology, the traveling wave tube (TWT) is widely used as a microwave power amplifier in radar, satellite communication, spacecraft transmitter and electronic warfare systems. This device has a unique combination of features such as high power, high gain and broad bandwidth, together with being relatively small in size, compared with other vacuum electron device types. Therefore, it meets the requirement of most applications that are commercialized. Rapid research progress in improving device performance has been made since the invention of the helix TWT by N.E.Lindenblad and Rudolf Kompfner in the1940's [25, 26]. A detailed analysis with the improved performance the first-ever TWT was made by J. R. Pierce and L.M. Field in 1947 [27, 28]. In subsequent years the advances in the research were credited to innovations in device design, and the enhancement of underlying theories and modelling methods to understand the device principle.

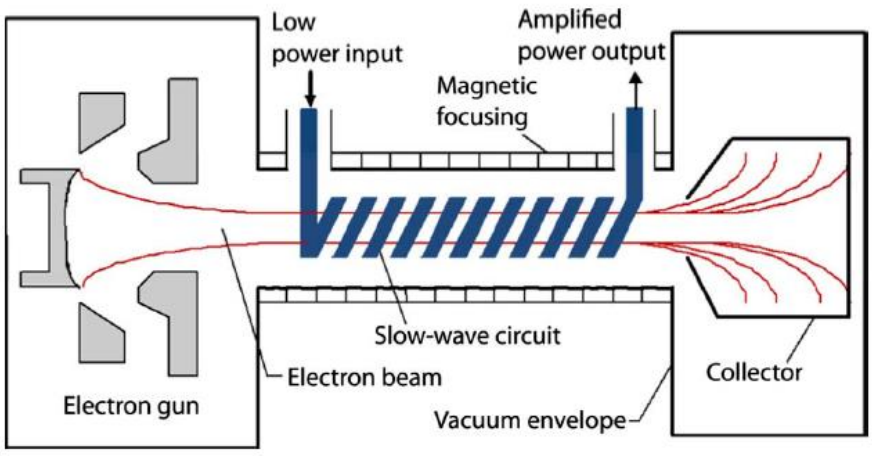

Figure 1.2: Schematic of the TWT [29].

TWT can be defined as a vacuum envelope, inside which an electron beam interacts with an electromagnetic wave. This interaction means that the electron beam transfers part of its kinetic energy to the electromagnetic wave, thereby amplifying the wave. Therefore, to facilitate the interaction process in the vacuum envelope, TWT required several parts, such as an electron gun, a guiding structure, a magnetic focusing system, a collector and vacuum windows, as shown in figure 1.2.

A condition for the energy transfer in the tube is that the velocity of the electron beam must be approximately equal to the phase velocity of the electromagnetic wave. However, the electron velocity in a vacuum is less than the speed of light in free space. The guiding structure does the job of slowing down the axial phase velocity of electromagnetic waves so that they are approximately equal to the velocity of electrons. Hence, the guiding structure is also called a slow-wave circuit or slow-wave structure (SWS). The characteristics of the TWT is mainly represented by the performance of the SWS that has to be facilitated for maximum energy conversion rate. The various SWSs of their millimetre-wave and THz version are given in details in the subsequent section.

The electron gun produces electron particles into the SWS, which is commonly consisted of a cathode, focusing electrodes and anode. The cathode, where the electrons particles emerge, is extremely difficult to machine due to miniaturization. The focus electrodes, the control electrodes, and the anode help to create the desired electron beam contour that is emanated from the cathode surface area and directed to the SWS [30, 31]. Moreover, the assembling of gun parts presents a challenging task in the process of gun making due to the stringent tolerances required between them. It is a fact that the operating temperature and robustness of cathode surface directly affect the lifetime and reliability of the product. Dispenser cathodes [32], nanocomposite dispenser cathodes [33], and scandate dispenser cathodes [34] have been proven effective for the millimetre-wave and THz TWTs. It was reported that a 750 A/cm^2 current density of sheet beam with corresponding to cathode loading of 56 A/cm^2 using Scandate cathode is achievable [35].

The beam focusing system provides an axial magnetic field to compensate the repulsive radial space charge forces in the electron beam, thereby maintaining the electron beam transmission in its axis during the interaction process. Unlike the traditional bulky solenoid magnetic system, period permanent magnetic (PPM) configuration can drastically reduce the size of the beam focusing system, which results in lowering the entire tube size and weight [36-38]. Further, it can provide an excess of 6000 Gauss magnitude of a uniform magnetic field, for the collimation of both beam geometries like sheet beam and circle beam, for the entire length of beam transmission, for millimetre-wave and THz TWTs [31, 39].

At the tail end of the SWS, the collector is placed to collect the all spent electron beam. A multistage depressed configuration of collector design, like three-stage and five-stage, is used to recover the spent electron beam power to enhance the intrinsic efficiency of the tube by up to order of magnitude [40, 41]. The higher the number of depressed voltage levels used the better the management of thermal cooling, and the more recovery of the beam energy is possible, also avoiding secondary emissions [42]. Vacuum windows which are, usually the type of component used in either of pillbox windows [42] or diamond windows [43], are transparent to electromagnetic waves as an interface between the high-vacuum region and ambient environment for the RF signal feeding into the tube and drawing from the tube. All subparts of the TWT should be assembled precisely within micron range accuracy and to be vacuum-sealed, to make a full working device.

1.3 State of the art THz SWSs

As mentioned in the previous section the SWS does the job of slowing down the propagating electromagnetic waves to match with the velocity of the electron beam, therefore there are two possible approaches in the design of SWS to perform their job. First approach is to delay the axial electric field components of the input electromagnetic waves in the guiding structure in which transverse fields propagate with their initial velocity. Helix structures are known to support this kind of wave propagation. The second approach is to create a load periodically to the electromagnetic

waves in the cavity waveguide which establishes slow electromagnetic waves. Examples that come under the second approach are corrugated waveguides and dielectric loaded waveguides. Any SWS design discussed in this section follows either of the above two approaches.

Furthermore, SWS exhibits either positive dispersion or negative dispersion characteristics (shown in figure 1.3). Positive dispersion means the phase velocity of the wave increases with an increasing wave-number for wavelength from 0 to 1π radian or in the fundamental space harmonics (blue line). It is the opposite case for the negative dispersive SWS where the phase velocity of the wave decreases with the increasing wave-number (yellow line). When a slope of the beamline intersects the forward-wave dispersion curve region, it indicates the synchronization condition for the forward wave interaction with an electron beam. The interaction allows the input wave gets amplified as it propagates from the input port to the output port. This operation is utilized in the TWT operation, in which the input port and output port are located at the gun side and collector sides, respectively.

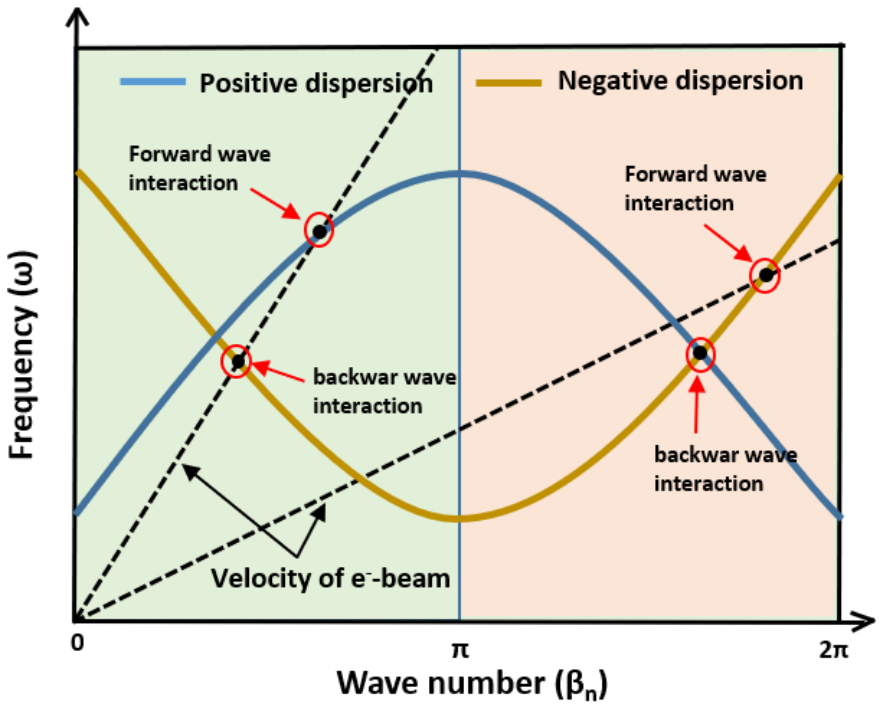

Figure 1.3: Frequency vs. wave-number or dispersion diagram of the fundamental propagating mode in a SWS.

On the other hand, if the slope of the electron beamline intersects the backward-wave dispersion regions, the backward waves constructively become built up in the tube, which originates from the collector end of the tube and propagates towards the gun side, where the stable backward waves are collected from the tube. This type of tube operation works as a signal generator without RF input, and so is called as a backward wave oscillator (BWO). This type of oscillators can inherently be used for wideband operation, especially with an electronic tuning by changing the beam voltage. Another approach is designing an oscillator using SWS by using the TWT feedback concept. Here the output of the TWT is connected back to the input through an external feedback path, which is called as a regenerative oscillator. The best method for oscillator design is the earlier method of using backward wave oscillations.

The SWS design metrics for the TWT and BWO operation are different. For amplifier design, the SWS must exhibit nondispersive characteristics over the intended frequency range. Therefore, such a TWT design can be operated with a constant beam voltage over the frequency range, thereby achieving a flat gain curve in the operation range. Whereas in the case of BWO operation, the SWS should exhibit dispersive characteristics over the desired frequency range. As a result, fine electronic tuning can be achieved by varying the beam voltage for generating RF signals with high resolution. For the best performance of a tube, positive-dispersive SWS for TWT design and negative-dispersive SWS for BWO design are the preferred choice. In subsequent sections, we will collectively discuss the two types of SWSs used for TWT and/or BWO in the millimetre-wave and the THz frequency band.

1.3.1 Planar helix SWS

The helical SWS based TWTs are a widely used power source in the microwave band since it has a high energy conversion efficiency and broad bandwidth. This is the fact that difficulties arise when realizing tiny helix structures using milling methods for frequencies beyond the 40 GHz which derivatives of the conventional helix are reinvented to be compatible with lithography-based microfabrication techniques.

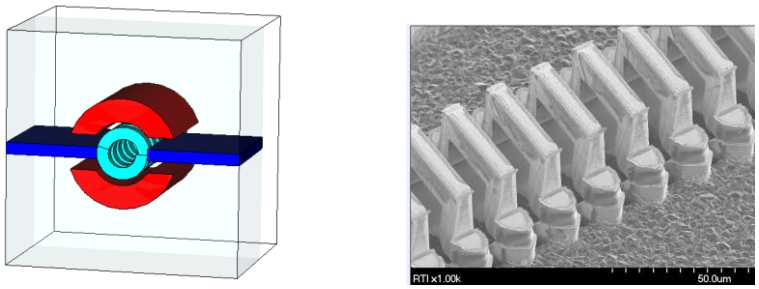

Figure 1.4: THz Helical SWSs to support: (a) circular beam [44], and (b) the rectangular beam [45].

The Teraphysics Corporation proposed a hexagonal-shaped helix tube operated by passing an electron beam as two semi-circular beamlets around the outside of the helix rather than passing through the centre which is generally used a conventional way, as shown in figure 1.4(a) [44]. The planar helix was fabricated to develop a 650 GHz signal source in the backward regime operating as an oscillator [45, 46]. The other parts of the tube were built and precisely assembled with the helix to make the prototype device working. The preliminary test results showed that the output power was 60 mW when operated with a beam voltage of 7 kV and 7 mA beam current and the predicated start oscillations were at 3.5 mA current [47]. Later, based on the 650-GHz helix TWT design, they developed a tube at around 95 GHz frequency range. It was predicted that the output power of 25 W would result in a 60% overall efficiency [48, 49]. Despite the successful attempt, the fabrication of planar helix involves a complicated fabrication process along with a need for diamond housing.

Another kind of helix circuit compatible with the microfabrication techniques was proposed, which is a planar helix with straight-edge connections derived from a rectangular helix configuration [50]. Due to the planarity of the circuit, this is more suitable for sheet beam configuration, as it passes through the inner side of the helix, similar to the conventional helix tubes used. A CPW (coplanar waveguide) transmission feed was employed to connect the helix with external circuitry. The UV-LIGA-like fabrication was proposed for fabricating the high frequency planar helix, and the cold-test results of fabricated W-band helix were reported [51]. More research on different configurations, such as a connected pair of a planar helix with straight-edge connections

[52], and a vane loaded planar helix with straight-edge connections [53], has been conducted for improving the planar helix design. The advantage of such a planar helix is that it can retain the broadband width nature of the conventional helix tube. However, it suffers from poor thermal dissipation, and it is rated as having low power levels.

1.3.2 Folded waveguide SWS

G. Dolher has made an initial demonstration of a working folded waveguide (FWG) TWT for operating in millimetre-wave frequency band [54]. The FWG is formed by bending 180^0 circularly the E-plane of rectangular waveguide in a serpentine pattern, as shown in figure 1.5.

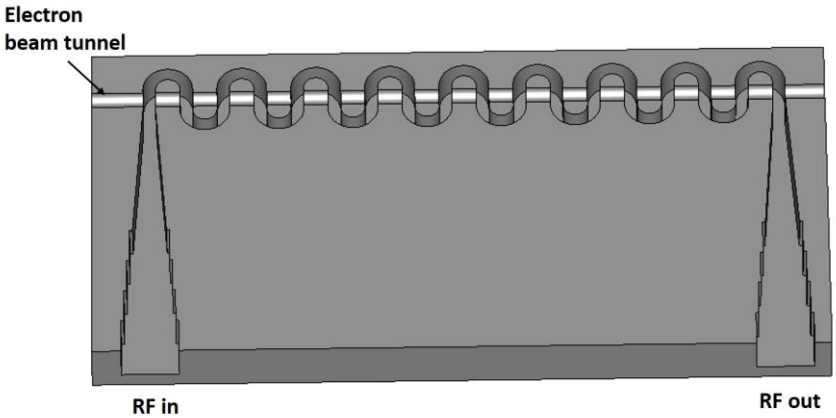

Figure 1.5: Schematic of FWG SWS.

A beam tunnel is formed by piercing through the broad-wall of the waveguide. The FWG is generally operated at a fundamental mode, TE_{10}, and the wave propagates along the serpentine pattern. However, the electron beam travels straight along the axis of the folded waveguide. Due to the wave propagating along the serpentine path, the electron beam encounters the reduced axial phase velocity of the wave. Thus, the benefit of the folded waveguide, in this case, is that it does not change the wave mode and uses its transverse electric field to interact with the electron beam. Following the initial proposal, the experimental studies on FWG TWTs surged across several research groups and institutions, and the FWG circuits were fabricated using conventional CNC mechanical milling [55-58]. Driven by the advancement in CNC milling capabilities and

electron discharge method (EDM), the fabrication of FWG circuits was done for submillimeter-wave frequency operation, such as 95-GHz (W-band) and 140-GHz (D-band) [59-63]. Besides, 220-GHz FWG TWTs were designed and fabricated using photolithography techniques [64-66].

A configuration of a multi-beamlets gun and single collector with each beamlet passes through an individual FWG circuit, was designed to enhance the output power of the TWT [67]. An integrated coupler was designed for this TWT to split the input drive signal equally for each of the FWG circuits and recombined the amplified signals at the output into a single output signal. In this way, at the same time, the individual beam thermal loading reduces with the number of beamlets used. 233-GHz [68] and 320-GHz [69] FWG TWTs were manufactured using high precision nano-CNC milling. To develop the 0.67-THz signal source, Northrop Grumman utilized the FWG in the regenerative principle to operate as an oscillator [70]. The 0.67-THz-FWG circuit was fabricated using DRIE (deep reactive ion etching) technique, and the test results showed 21.5 dB gain and 15 GHz operational bandwidth [71]. Northrop Grumman also developed 0.85-THz TWT amplifier based FWG, which is based on the previously developed 0.67-THz regenerate TWT [72]. This tube can produce an output power of 39.4 mW at 0.85 GHz, with an instantaneous bandwidth of 11 GHz [73].

1.3.3 Derived folded waveguide SWS

FWG-SWSs are inherently narrow-band structures whose bandwidth is limited to a maximum of 30%. Moreover, the efficiency of electron interaction is also low due to the low value of interaction impedance in conventional FWG-SWS. Thus, there is a need to explore the possibility of enhancing both the bandwidth and interaction impedance in the structure.

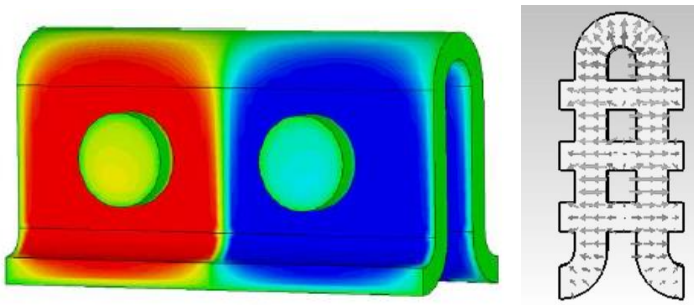

(a) (b)

Figure 1.6: (a) Over-moded FWG [74], and (b) Multibeam FWG [74].

FWG are generally designed to operate in the fundamental mode with single beam tunnel that cannot hold the large beam current for supporting high beam power. The FWG operating at the higher-order mode or over-moded can be suitable for multiple beam configuration. This facilitates an increase in the beam current while maintaining the same beam current density for each beam channel (figure 1.6(a)) [75-77]. In [77] the FWG TWT was designed to operate in the TE_{20} higher order mode with two-beam channels. The simulation results predicted that this type of over-moded FWG TWT can provide an increased electron efficiency of 5.4% as compared to the 1.8% by conventional FWG TWT operating in the TE_{10} mode. The over-moded FWG TWT suffers from the mode competition, band-edge oscillations, low bandwidth, and decreased the interaction field, as well as needing excessive beam voltage. The additional complexity of the over-moded FWG is due to the multiple beam configuration of the electron gun and the magnetic focusing system.

In contrast to the over-moded multi-beam FWG TWT, another approach for multi-beam configuration was proposed by splitting the sizeable single beam channel into multiple-beam channels in the fundamental mode operation itself, as shown in figure 1.6(b) [78, 79]. With multi-beam configuration, there is an increased electron efficiency of 7.4% from 1.06% by the single beam FWG TWT at 140 GHz, at the same time maintaining the same bandwidth [79]. However, the multi-beam configuration enhances the electron efficiency that results in a higher power output which then; restrains the amount a beam current can hold by an individual beam channel. A linear array of FWG each containing single-beam channel mitigates the adverse effects from high current density in the

single-beam-single-FWG TWTs [67]. Because the multiple FWG approach lowers the beam current required in the individual FWG circuit, this results in a lower beam tunnel fill factor and thus a lower total thermal load compared to a single-beam device. Furthermore, it collects the power from each FWG at the output section, thus there is overall more output power in the device.

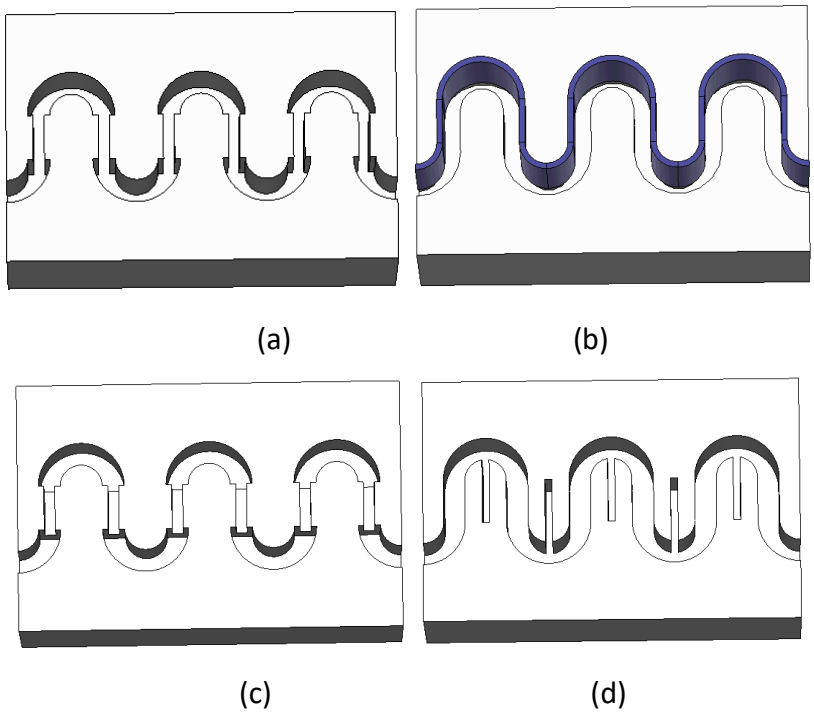

Figure 1.7: Modified configuration of FWG slow-wave circuit: (a) short range ridge-loaded FWG, (b) long range ridge-loaded FWG, (c) ridge and vane loaded FWG, and (d) grooved loaded FWG.

One of the inherent drawbacks of the FWG TWT is the band-edge instability causing unwanted oscillations, particularly from the first-stop band [80, 81]. The band-edge instability is due to the proximity of the fundamental mode with next higher-order mode, as well as arising from the fabrication tolerances and beam channel imperfections. Enlarging the portion of circular bend and narrowing the straight segment of the FWG is to alleviate the 3π-stop-band band-edge instability. This modification also helps to enhance the electric field in the beam channel [82]. In this paper [83] has investigated the methods to suppress the 3π-stop-band band-edge instability.

A ridge-loaded FWG TWT [84] was proposed to enhance the beam-wave interaction, where the ridge load is applied to the straight segment, shown in figure 1.7(a) [84]. The concept was developed for the W-band TWT that can produce an output power excess of 25 W for the frequency from 93.1 GHz to 94.8 GHz with a gain of over a 23 dB [85]. To enhance the bandwidth of the FWG TWT, a similar kind of the ridge-loaded FWG was proposed, where the ridge is inserted in one of the broad walls of the FWG over an entire length as shown in figure 1.7(b) [86]. The behaviour of the ridge-loaded FWG was studied using different analytical methods, such as the equivalent circuit analysis, parametric analysis, and a quasi-TEM analysis, for dispersion and interaction impedance characteristics. Moreover, the analytical studies were verified against results from 3-D electromagnetic simulations and cold-test experimental data.

A more complex geometry of FGW, which includes ridges along the horizontal and vertical sides of the straight segment of the FWG, was proposed (figure 1.7(c)) [87]. The simulation results predicted the increased interaction impedance compared to the conventional FWG. The more complexity in the geometry, the more challenges to the fabrication phase. The fabrication could be done either using a milling method or a photolithography process.

When the width of the ridge increases the effective length of beam-wave interaction in the beam channel decreases. To avoid this type of loading, incorporation of a groove between two straight segments helps to increase the interaction impedance and to improve the linearity of the dispersion curve, but at the cost of reducing the bandwidth [88, 89].

The concept of the frequency multiplier was implemented in the TWT, by dividing the SWS into three sections: fundamental section, drift section and harmonic section [90, 91]. A source frequency is excited into the fundamental section to modulate the injected electron beam. The modulated beam passes through the drift tube further into the harmonic section, where the beam is tuned to the desired harmonic frequency of the input signal frequency, according to the harmonic section designed. The harmonic frequency is then amplified through the beam-wave interaction process in the harmonic

section before it is collected at the output port. In contrast to the circular beam FWG TWT, FWG was utilized to support the sheet beam with a rectangular beam tunnel [92-94].

1.3.4 Sheet-beam corrugated SWS

A SWS, composed of periodically loaded metal corrugations or vanes transverse to the broader side in a rectangular waveguide along the axial direction, is more viable to fabricate operating from the microwave frequencies up to THz frequency bands. It also offers mechanical robustness and a high thermal dissipation capability. This type of SWSs is suitable for sheet-beam tube types.

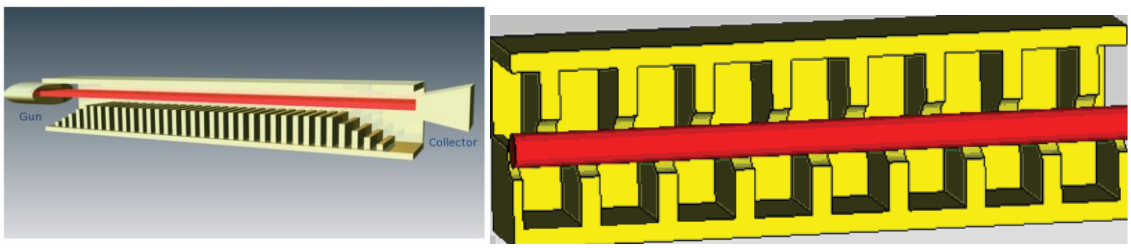

(a) (b)

Figure 1.8: Sheet-beam corrugated SWS: (a) single corrugation SWS [95] , and (b) double-staggered corrugated SWS [96].

A simple design of a metal corrugation transverse to the broader side of the rectangular waveguide was conceived as a SWS for TWTs and BWOs (shown in figure 1.8(a)) [95]. An electron beam sends over the corrugation for the beam-wave interaction process. The SWS was used to design a 220-GHz TWT amplifier with an estimated growth of 33 dB/cm at 211.3 GHz [96]. The LIGA technique was applied to fabricate the SWS and validates the electromagnetic characteristics using S-parameters measurements. [97]. By reducing the width of corrugations, the SWS can provide more interaction fields available for energy transfer [98, 99]. A 1-THz BWO was designed using the narrow-corrugated SWS [99, 100].

Young-Min Shin proposed a SWS which is composed of a pair of half-period staggered corrugations in a rectangular waveguide, for THz TWTs, as shown in figure 1.8(b) [101].

It offers strong axial electric fields in the beam channel which is the region between the two opposite rows of corrugations. The SWS was applied to design a 220-GHz sheet beam TWT [102, 103]. Various microfabrication techniques, like LIGA, DRIE and nano-CNC milling, were used to explore the feasibility of fabricating the SWS [104]. The test results of the prototype device demonstrated an output power of 107 W with 6 GHz 3-dB bandwidth centred at 200 GHz [105]. Later, the SWS was considered at various frequency bands for the TWT [106, 107] and BWO [108]. A modified version of staggered double corrugated SWS was proposed, with a sinusoidal geometry [109]. A large signal code for staggered double vane SWS was developed [110]. With the help of this code, the analysis can be done quickly in comparison with the commercial three-dimensional (3D) software tools.

1.3.5 Circular-beam corrugated SWS

C. Paoloni proposed a novel rectangular waveguide assisted SWS that supports a circulated beam [111]. It is composed of two rows of corrugations across the transverse plane in the axial direction, called as a DCW (double corrugated waveguide) SWS, as shown in figure 1.9. The distance parting the two rows of corrugations defines the beam tunnel, which is the region where electric fields are used for interacting with the circular-electron beam. This SWS offers easy fabrication using either the mechanical milling methods and lithography based techniques, making it promising for THz tubes [24].

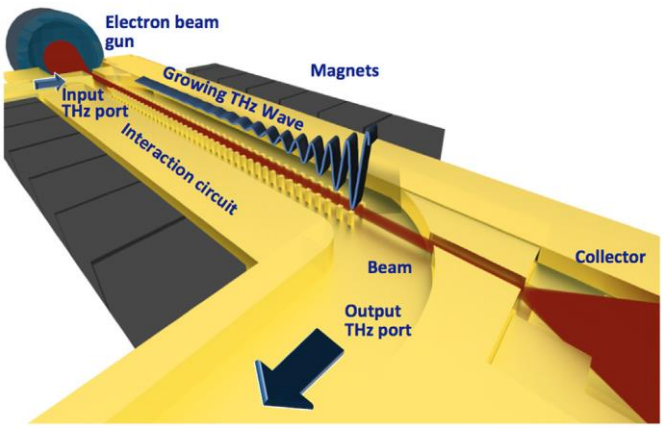

Figure 1.9: DCW SWS for supporting a circular beam [1].

Initially, DCW SWS was used to operate in the backward region for THz BWOs. A 1-THz backward wave the amplifier (BWA) using the DCW SWS was designed [112] and fabricated using the PMMA DXRL (deep X-ray lithography) process. The DCW SWS was also used to operate in a forward wave regime for 0.22-THz TWT [113]. Later it was adopted to design a Ka-Band TWT [114], 71-76-GHz TWT [115], and 0.346-TH BWO [74].

1.3.6 Meander-line SWS

The meander-line based SWSs, uses a dielectric substrate, allowing the tube to operate at a very low beam voltage. The low beam voltage operation makes the size of a tube compact, thereby reducing the cost. A planar type, bipolar interdigital SWS was proposed for 300-GHz and 600-GHz BWOs, as shown in figure 1.10(a) [116]. The bipolar interdigital circuit was conceived by placing the two sets of fingers in a parallel configuration through which the RF signal propagates. The space between the two sets of fingers defines the beam tunnel. The bipolar interdigital line was fabricated using the DRIE technique on a SOI wafer with diamond coated structures [117]. It was reported that the output power could be in the range of 20 mW to 25 mW over a 20% bandwidth at a centre frequency of 300 GHz. The interdigital lines were designed on different configurations of the substrate (shown in figure 1.10(b)) [118]. The modification of substrate beneath the fingers was done in order to realize the membrane-type interdigital lines and freestanding-type interdigital lines, which are useful in reducing the effective dielectric constant, thereby providing an increased mode field in the electron beam region. The configurations were employed for developing the 1-THz BWOs [118]. The test results reported that the substrate interdigital line based BWO can be delivered an approximate power of 0.5 mW at 0.3 THz. The interdigital SWSs are negative-dispersive SWS, and they present high slow-wave factor and very high interaction impedance.

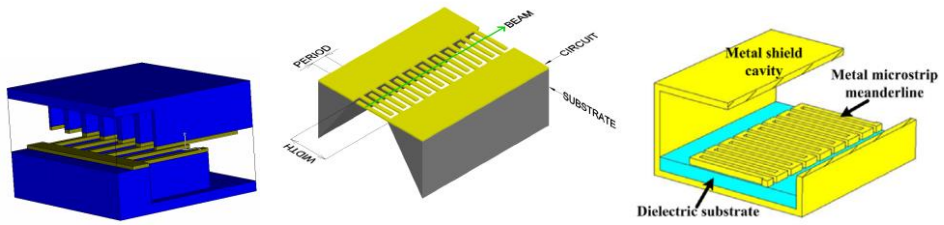

(a) (b) (c)

Figure 1.10: Planar SWSs: (a) bipolar interdigital SWS [116], (b) free interdigital line SWS [118], and (c) microstrip meander line SWS [119].

Another meander line-type planar SWS was proposed for TWTs and BWOs, shown in figure 1.10(c). Similar to interdigital SWSs, it also operates at a low beam voltage at the same time making it easy to fabricate [119]. Various versions of the meander line SWSs were reported in the literature, such as V-shaped meander line [120, 121], a symmetric double V-shaped meander line [122], a ring-shaped strip line [123], and sheath structure [124]. The advantages of these type of planar structures are that they do not require growing the thick metal structures using photolithography processes [125]. The meander line structures usually needed tens of micron or less metal pattern on the dielectric substrate, which can be done by easy photolithographic process steps [126]. Few of these SWSs were tested using verifying of s-parameters experimentally [119, 126, 127]. This type of SWSs provides a narrow bandwidth.

1.4 Microfabrication techniques for THz SWS

When the operating frequency pushes towards the THz, the dimensions of the SWS shrink to hundreds of microns or even less, and fabrication tolerances at these frequency ranges are very demanding. It is impractical to produce such micron level features using traditional machining techniques. In recent years, research has been focused on attempting the fabrication of those micro-sized SWSs for THz TWTs and BWOs using various microfabrication techniques. These microfabrication methods are also useful for manufacturing the other parts of the THz tubes. This section discusses the possible micromachining techniques for fabricating THz SWSs.

1.4.1 LIGA

LIGA, German abbreviation of Lithographe, Galvonoformung, und Abfornung (in English, lithography, electroplating, and micro-molding), is a lithography process in conjunction with electroplating. The LIGA technique can produce metal structures that can be a few millimetres tall and extremely small features in the micron range [128, 129]. As shown in figure 1.11, the necessary fabrication sequences are photoresist deposition, pattern transfer through a mask, mold development, electroplating of metal into the mold and finally stripping of mold or metal parts [130]. The surface of the substrate base must be conductive in order to facilitate a current path for the electroplating.

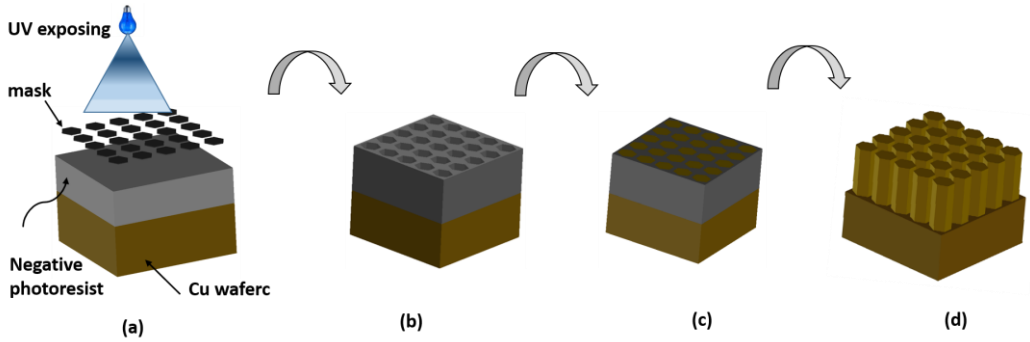

Figure 1.11: LIGA fabrication process flow: (a) UV expose on to photoresist, (b) photoresist development, (c) electroplating, and (d) photoresist removal.

The LIGA process uses X-ray radiation from a synchrotronic source to expose into photoresist through a metallic mask [129]. A commonly used photoresist material that reacts with X-ray radiation is Ploy-methylmethacrylate (PMMA) [131]. It is a positive photoresist type whose exposed areas are dissolved in the developer. An X-ray LIGA using PMMA can produce a metal parts aspect ratio up to 100:1 of about 3 mm height. Ka-band [132, 133] and W-band [134] copper electroplated FWG was fabricated using X-ray LIGA using PMMA photoresist. In [134], a two-step LIGA was used to make a beam tunnel in the FWG, which provides better fabrication tolerance (< 2µm) than machining methods. The PMMA X-ray LIGA requires a very long exposure time and takes a long time to develop, for example, it takes several tens of hours for fabricating 1-mm-thick photoresist mold [135]. This is because the sensitivity of PMMA photoresist to the X-ray

radiation is very weak. Besides, X-ray LIGA needs an expensive gold mask. It was proven that this process produces an undercut in the PMMA mold due to backscattering from the substrate. SU-8 photoresist was developed as an alternative to the PMMA for LIGA applications. The SU-8 is a negative photoresist, so the exposed areas remain after etching. The benefits of using the SU-8 compared to the PMMA are that the photo absorption to x-ray radiation is 200 times more, better tolerance control, and it does not require an expensive gold-mask [135].

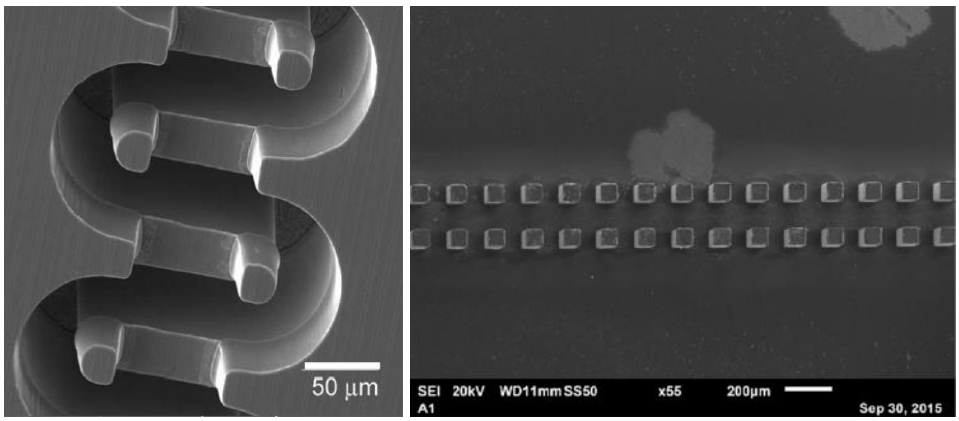

(a) (b)

Figure 1.12: SU-8 LIGA-fabricated SWSs: (a) 670-GHz FWG [136], (b) 300-GHz DCW SWS [137].

An ultraviolet (UV) radiation to SU-8 requires less exposure time compared to an X-ray. A SU-8 UV-LIGA can produce a good mold quality with perfectly vertical sidewall profiles [138, 139]. The UV-LIGA using SU-8 was applied to fabricate several millimetre-wave and THz SWSs for TWT and BWO developments. Examples are shown in figure 1.12. The folded waveguide SWS was made using the SU-8 UV-LIGA technique for the various band of frequencies, such as 95 GHz [140, 141], 140 GHz [142], 220 GHz [143-146], 670 GHz [136]. A polymer filament was used in the LIGA process to make a beam tunnel in the FWG SWS, avoiding the need for the two-step LIGA [143]. The choice of filament material must be compatible with the SU-8 process and electroplating solution. Furthermore, the diameter of the filament must be equal to the tunnel width. This method is more critical for frequency over the 220 GHz, due to the shrinking of the beam tunnel size makes challenging for using the filament. The DCW SWS [137], and sheet

beam based SWS [97, 147] were fabricated using the SU-8 UV-LIGA technique with single-step LIGA. These SWSs do not require additional fabrication steps to make the beam tunnel. It is a fact that the etching of cross-linked SU-8 poses difficulties [148]. Several approaches have been explored to find the best solution for stripping the cross-linked SU-8 [97]. A KMPR photoresist is a promising choice of mold material for UV-LIGA application, which is similar to SU-8.

The KMPR UV-LIGA process was employed to fabricate the 340-GHz FWG SWS [149] and the 220-GHz staggered double vane SWS [150]. It revealed that compared to SU-8, the KMPR photoresist is much easier to lift-off after the electroplating step. The sidewall surface roughness of LIGA-fabricated SWSs is mainly dependant on the quality of the photoresist mold and the electroplating process conditions. The photoresist molds can produce very smooth surfaces, < 20 nm. However, the process conditions must be optimized for there are any changes in the design, which is not favourable. The LIGA technique is limited to producing 2D geometries. But, the modified versions of LIGA techniques could fabricate 3D geometries.

1.4.2 DRIE

DRIE is a subtractive process where a portion of the silicon substrate is etched away for producing high aspect ratio structures, while LIGA is an additive process. Both techniques utilize the photolithography process to create a mold pattern. The process flow of DRIE is described in figure 1.13. The first step is to oxidization of the silicon surface and followed by a thin deposition of photoresist. The photoresist is exposed to UV radiation through a mask and develops photoresist to make a SiO_2 pattern on silicon. Then fluorine-based gases are used to etch the silicon where the regions are not covered with SiO_2. An anisotropy etching of silicon can be improved by ion impact assistance coupled with sidewall passivation. Etch and passivation process steps are repeated until the desired etch depth is achieved. After Si etch, the SiO_2 pattern is removed. Finally, the DRIE fabricated Si mold is metal coated with a thickness multiple times the RF skin-depth.

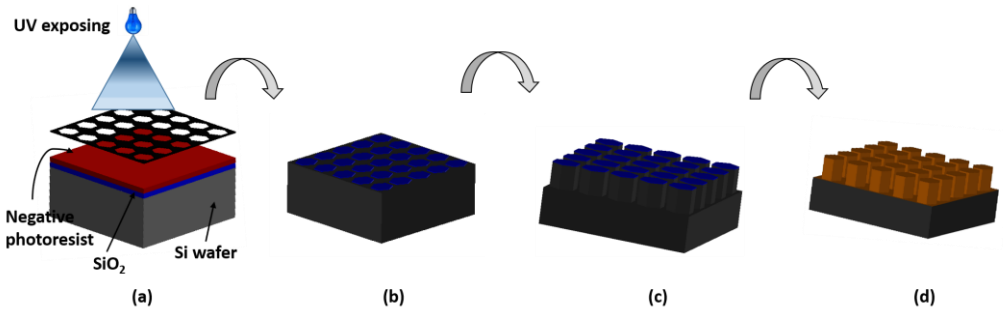

Figure 1.13: DRIE fabrication process flow: (a) UV expose on to photoresist, (b) photoresist development, (c) Si electing using DRIE, and (d) photoresist removal and metal coating.

The DRIE technique was used to fabricate the SWSs for the THz TWTs and BWOs. 600-µm depth trenches in the Si were made to fabricate a 220-GHz sheet-beam SWS, shown in figure 1.14 [147]. The FWG SWSs were built using Si-DRIE process for W-band [141] and 650-GHz frequency band [151]. The SOI wafers which follow the two-level etch using DRIE process were used to fabricate FWG SWSs with beam tunnel for 220 GHz [152], 670 GHz [71], and 850 GHz [153] TWT sources. The thin metal film deposition on Si mold by physical vapour deposition can produce nanoscale surface planes. However, the drawback of the DRIE technique used for the tube operation is that the thermal dissipation by Si wafer is very poor.

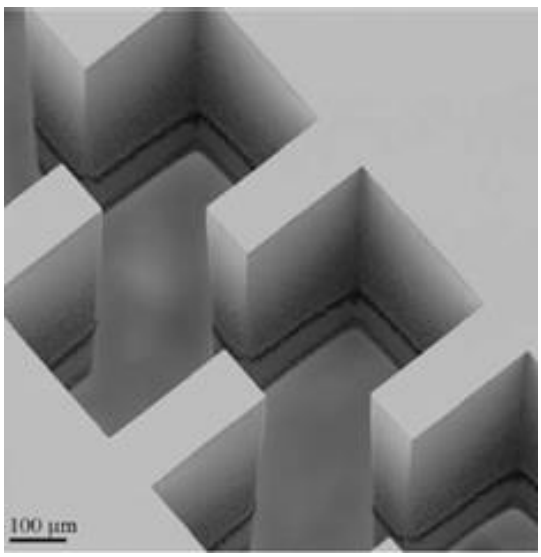

Figure 1.14: Si DRIE-fabricated 220-GHz double-staggered corrugated SWS [147].

1.4.3 Electrical discharge machining

Electrical discharge machining (EDM) methods are used to remove material from the workpiece through the erosion process to manufacture the desired shape. The removal process makes use of electrical energy between the workpiece and an electrode and turns it into thermal energy through a series of discrete electrical discharges between them in deionized (DI) water or dielectric medium. Figure 1.15 shows the schematic of EDM and the process of material removal mechanism [154]. The wire EDM (WEDM) technique uses water-based dielectric replacing the hydrogen oils used in conventional EDM, which is environmentally safe. It can manufacture the structures with a tolerance as low as 1-2 µm. The WEDM uses the electrodes, such as brass, molybdenum or tungsten wire with a diameter ranging 0.02-0.40 mm. Compared to hydrocarbon oil-based conventional EDM, the water-based EDM can produce a better surface finish. The minimum achievable size and internal corner radii are limited to the wire radius and plasma discharge thickness. The quality of machined parts is also limited to the type of structures manufactured by cutting through a given chord of the workpiece.

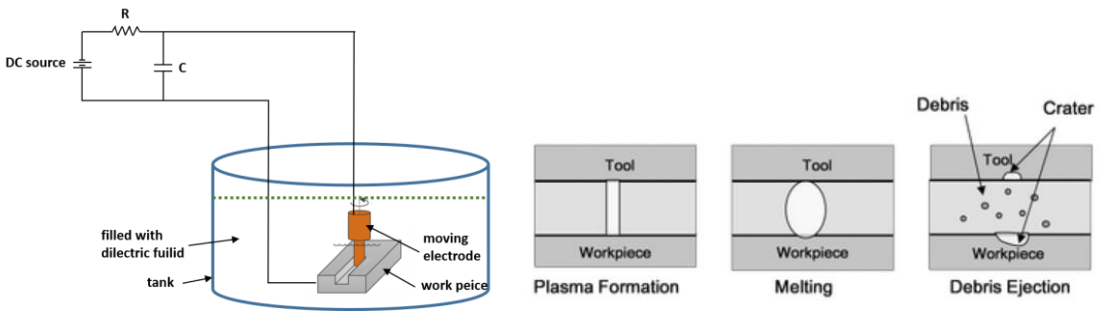

Figure 1.15: EDM working principle: (a) simplified schematic view, and (b) material removal mechanism [154].

In the case of micro-EDM, it can manufacture micro-holes and micro-shafts into high-aspect-ratio three directional structures, regardless of the hardness of the conductive materials [155]. The EDM method was used to build a W-band FWG SWS [74]. This manufacturing method produced the submicron-scale surface finish on the FWG SWS internal walls on copper workpiece [154]. The EDM was also employed to make a beam

tunnel on the LIGA–fabricated FWG SWS [64]. The achievable resolution and surface finish by the EDM methods are not suitable for the SWS operating beyond W-band [156].

1.4.4 CNC milling

A CNC (computer numerical controlled) milling machine can aid the removal of material from the workpiece due to an extra degree of freedom in motion and by the use of automatic functional features to manufactured 3D structures in a controlled manner. Using CNC mills, the RF structures up to the Ka-band has been reported [54-56, 103]. The conventional CNC mills are limited to a resolution a ten of microns, and a poor surface finish capability. Hence, the manufacturing of the RF structures beyond the W-band is impossible. A recent demonstration of advanced CNC mills so-called nano-CNC mills which can produce a resolution of around ~1-5 um and the nanoscale surface finishing. The advanced CNC mills have been utilized to manufacture several submillimetre-wave SWSs: 95-GHz FWG [62], 140-GHz FWG [59, 63], 220-GHz FWG [68, 157], 320-GHz FWG [69], 95-GHz DCW, 220-GHz staggered double vane SWS [105]. Figure 1.16 shows the CNC-milled FWG for G-band TWT [68]. The CNC milling can feasibly be used for prototype devices at these frequency ranges. However, it cannot be applicable for mass production.

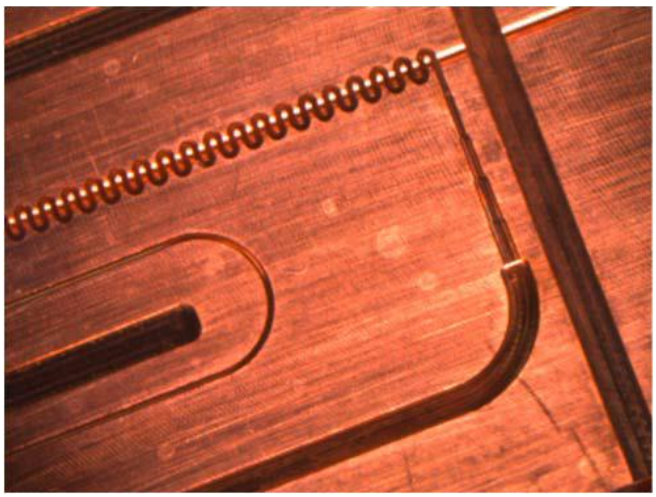

Figure 1.16: CNC-milled G-band FWG SWS [68].

1.4.5 3-D printing

3-D printing, also known as additive manufacturing, has found widespread applications in the rapid prototype and production of geometrically complex components. The interest of additive manufacturing has been explored for passive and active RF components [158]. Recently an exploration of the additive manufacturing for SWSs has been begun [159, 160]. A 95-GHz FWG SWS was fabricated using 3D-printing technology [161].

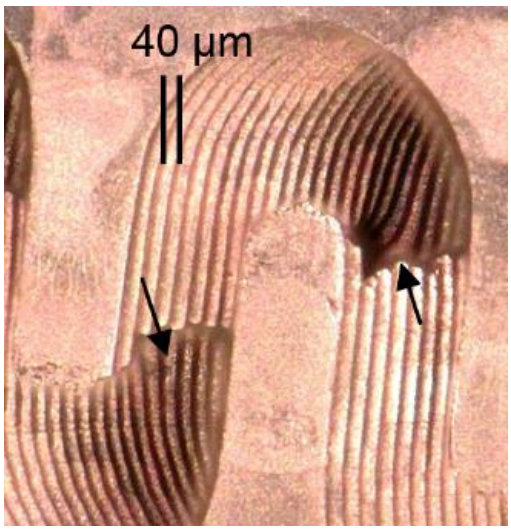

Figure 1.17: Surface morphology of 3D-printed electroplated copper FWG SWS [162].

The inverse of the FWG was 3D printed using a polymer material on copper substrate. Then, copper was electroplated into the plastic mold. Finally, the plastic material was removed completely using downstream chemical etching, leaving only the copper microstructure on the copper substrate. The layer natured of the 3D printed mold in the z-direction produced 40 µm depth corrugations imprinted in the copper structures, which severely affects the THz signal propagation, as shown in figure 1.17 [162]. The kind of surface quality limits the use of the 3-D printing technology to manufacture SWSs for frequencies over 300-GHz. The corrugation imprints could be minimized by adjusting the process settings of the 3D printer, the use of different mold materials and their processing approach.

1.5 Scope of the thesis

This thesis proposes a new design of a slow-wave structure, called H-plane and E-plane loaded SWS, for developing a THz TWTs. Such a new design assists in easy fabrication by using available microfabrication techniques, and it can also provide a high gain-bandwidth product. Chapter-1 consists of an explanation of the basic principle of TWT and literature on the THz SWSs and their possible microfabrication methods. The proposed H-plane and E-plane loaded SWS design is analysed and simulated for 400-GHz TWT which reported in chapter-2. The simulations are divided into three steps: Eigenmode simulations, transient simulations, and PiC simulations. Eigenmode simulations are used to extract the electromagnetic characteristics of the SWS, which will be utilised for next stage simulations. By using time-domain transient solver, a coupler design for the new SWS is devised, which can be fabricated as an integral part of the SWS by applying the same fabrication method employed for the SWS. The TWT performance based on the H-plane and E-plane loaded SWS, such as gain, 3-dB bandwidth and power, is predicted using PiC simulations. Chapter-3 presents the experimental studies on the KMPR-based LIGA technique for the H-plane and H-plane loaded SWS fabrication. It includes the optimization of the KMPR lithography process parameters, electroplating and diffusion bonding of the LIGA-fabricated parts. A quantitative structural study of the fabricated samples was conducted, for examining fabrication tolerances and their process conditions. A study of surface morphology of the electroplated copper structures was studied. The quality of bonding strength between the LIGA fabricated copper structures was analysed at different experimental conditions, by scanning electron microscope (SEM) inspection and shear test methods. Chapter-4 emphasis the test results of the H-plane and E-plane loaded SWS at W-band. The W-band SWS was manufactured using the CNC milling. This chapter also reported the simulations results of the SWS at W-band. At the end of the thesis, journal papers are attached, which give an insight into the research findings from the Ph.D. work.

Chapter 2

2 Design and simulation of H-plane and E-plane loaded SWS for 400-GHz TWT

The discovery of a new type of SWS is the way to improve the performance levels of the tube, which is the first and most important performance decider of the TWT. Therefore, a variant and a robust design that is H-plane and E-plane loaded SWS has been proposed for the THz TWTs. This chapter focuses on investigating the performance of 400-GHz TWT amplifier using proposed SWS by utilizing the analytical method and numerical simulations. Pierce linear theory is used for an approximate estimation of small-signal gain. The computer simulations are first used to investigate the electromagnetic characteristics of the SWS, and then performed the beam-wave interaction simulations. A coupler for proposed SWS is devised for efficient use of intrinsic bandwidth of the SWS without losing RF power during wave transition. Finally, this chapter discusses the phase velocity technique employed to extend the performance level of the tube.

2.1 Analytical theory of SWS

The classic small-signal theory of interaction of an electron beam with a traveling-wave is presented, which was developed by J.R. Pierce. To discuss any TWT design, the parameters he derived are considered as standard metrics, and this will also be applied for designing this TWT. Pierce's theory is built up by finding an electronic equation and the current equation. The electronic equation referred to the AC current is caused by an axial electric field, whereas the circuit equation referred to the field in the circuit due to an AC current in the beam. The circuit equation and electronics equation can be combined to form the determinantal equation whose solutions are for all possible propagation modes.

2.1.1 Electronics equation

First, we will derive the equation of AC current of the beam from the axial electric field. Due to the electric field force, it is assumed that there are small variations in the velocity, current, and density of the electron beam:

$$v = v_0 + \bar{v}, \tag{2.1}$$

$$i = -I_0 + \bar{i}, \tag{2.2}$$

$$\rho = -\rho_0 + \bar{\rho}, \tag{2.3}$$

The indication of a subscript of zero and the bar above the variable are for the initial quantities and the quantities that small perturbation proportional to $e^{[j(\omega t-\beta z)]}$, respectively. First, we introduce the current density, which is defined as a product of the electron density and velocity of the electrons, and the current density is substituted by electron current over the beam cross-section, A:

$$J = \frac{i}{A} = \rho v \tag{2.4}$$

Then we substitute equations (2.1), (2.2) and (2.3) into equation (2.4) and expand out the terms replacing $\bar{\rho}\bar{v} = 0$ which reduce the equation to a second-order equation:

$$\bar{i} = \left(\bar{\rho} v_o - \rho_0 \bar{v}\right) A \tag{2.5}$$

It is worth considering the continuity equation $\nabla . J = -\partial\rho / \partial t$, and the derivatives that can be reduced after the substitution of the perturbation of quantities with $e^{[j(\omega t-\beta z)]}$,

$$\bar{\imath} = \frac{A\omega\bar{\rho}}{\beta} \tag{2.6}$$

Combining equation (2.5) and continuity equation, forms the perturbed current and velocity equations,

$$\bar{i} = \left(\frac{\beta v_0 \bar{i}}{\omega A} - \rho_0 \bar{v} \right) A \tag{2.7}$$

$$\bar{v} = \frac{-\bar{i}}{\omega \rho_0 A} \left(\omega - \beta v_0\right) \tag{2.8}$$

In the presence of the electric field, $E_z = E_1 e^{j(\omega t - \beta z)}$, the electrons accelerate as

$$\frac{dv}{dt} = \frac{-e}{m} E_z \tag{2.9}$$

Partial derivatives of equation (2.9),

$$\frac{dv}{dt} = \frac{\partial v}{\partial t} + \frac{\partial v}{\partial z}\frac{\partial z}{\partial t} \tag{2.10}$$

With $\frac{\partial z}{\partial t} = v_0$, the partial derivatives can be evaluated with the perturbed quantities,

$$\bar{v}(j\omega - j\beta v_0) = \frac{e}{m} E_z \tag{2.11}$$

Finally combining equations (2.8) and (2.11) and considering the$\beta_e = {\omega}/{v_0}$, $I_0 = \rho_0 v A$, and $V_0 = {mv^2}/{2e}$, establishes a relationship between current and electric field.

$$\bar{i} = \frac{j\beta_e I_0 E_z}{2V_0(\beta_e - \beta)^2} \tag{2.12}$$

Where *I0* and *V0* are the current and voltage operation conditions of the electron gun.

Including the space charge field effect, $E_{sc} = j\frac{m\omega_q^2}{e\rho_0\omega A}\bar{i}$, $\omega_q = R\omega_p$, the equation (2.12) becomes

$$\bar{i} = \frac{j\beta_e I_0 E_z}{2V_0(\beta_e - \beta)^2 + \frac{w_q^2}{v_0^2}} \tag{2.13}$$

2.1.2 Circuit equation

The SWS is modelled as a distributed transmission line in Pierce's theory, in which it is assumed that the same slow-wave behaviour in the transmission line model as well.

Therefore, the AC current on the beam is then coupled with the transmission line and induces fields to be added to the fields already present in the transmission line.

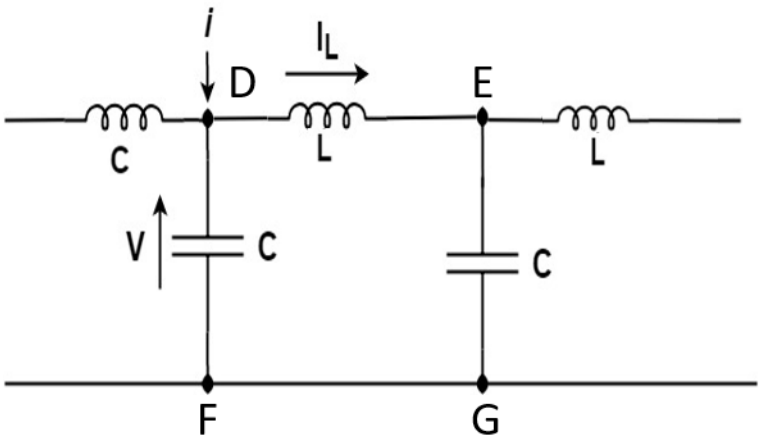

Figure 2.1: The equivalent transmission line model of a SWS.

Figure 2.1 shows the equivalent transmission line model of the SWS, assuming to have a distributed inductance, L, and capacitance, C, per unit length. The circuit analysis begins by considering an electron beam with AC current, i, passes close to the circuit inducing a current, Δi, onto the transmission line. The induced current is injected into the transmission line at each node between inductors. The voltage and current changes between each node can be written as $\frac{\partial V}{\partial z}\Delta z$, respectively $\frac{\partial I_L}{\partial z}\Delta z$. Now applying Kirchoff's current law at node D and Kirchoff's voltage law around DEFG, the quantities of i, I_L and V are small quantities that perturbate with the quantity $e^{[j(\omega t-\beta z)]}$, assuming $\Delta z \to 0$ we get:

$$j\beta i = -j\omega CV + j\beta I_L \qquad (2.15)$$

$$-j\omega V = j\omega L I_L \qquad (2.16)$$

Solving the equations (2.15) and (2.16) for voltage equation,

$$V = \frac{\beta\omega L i_z}{\beta^2 - \omega^2 LC} \qquad (2.17)$$

Now we assume as before that the electrons pass close to the transmission line, then the change in voltage between nodes of the transmission line will be an electric field on the electron beam.

$$E_z = -\nabla.V = -\frac{dV}{\partial z} = j\frac{\beta^2 \omega L}{(\beta^2 - \omega^2 LC)} i \qquad (2.18)$$

Phase velocity and the interaction impedance of the circuit are defined with circuit constants, L and C:

$$v_p = \left(\frac{1}{LC}\right)^{1/2} \text{and } K = \left(\frac{L}{C}\right)^{1/2} \qquad (2.19)$$

By rewriting the electric field equation (2.18) we get the following form:

$$E_z = j\frac{\beta^2 \beta_c K}{\beta^2 - \beta_c{}^2} i \qquad (2.20)$$

For microwave the circuit impedance is related to power travelling on the circuit by

$$Z = \frac{|V|^2}{2P} \qquad (2.21)$$

And from (2.18):

$$E = V\beta_c \qquad (2.22)$$

We get the following for the interaction impedance:

$$K = \frac{|E_n|^2}{2\beta_c^2 P} \qquad (2.23)$$

Where subscription *n* refers to space harmonic of the electric field, the fields that would be by the electron beam. According to the Floquet's theorem

$$E_n(x,y) = \frac{1}{P}\int_0^L E(x,y,z) e^{j(\frac{2\pi n}{P})z} dz \quad \text{and } \beta_n = \beta_0 + \frac{2\pi n}{P} \qquad (2.24)$$

Where *p* is the total length of integration. Coupling impedance is only based on axial electric fields travelling with the electron beam. E_n is found by taking the spatial Fourier transformation. For these calculations, it is assumed that β_n is the axial velocity of the circuits and first space harmonic. Calculating the value of E_n in 3D electromagnetic simulations is not straight forward. E_n shows the integration of the total electric field in the *z*-direction multiplied by a phase, where both terms will have real and imaginary parts. The simulation software does not allow one to integrate non-real numbers; therefore, the following formulas are used in a post solver run to find the square magnitude of E_n :

$$E_n(x,y) = \frac{1}{P}\int_0^L Re(E(x,y,z)\, e^{j\left(\frac{2\pi n}{P}\right)z})dz + j\frac{1}{P}\int_0^L Im(E(x,y,z)\, e^{j\left(\frac{2\pi n}{P}\right)z})dz \quad (2.25)$$

$$|E_n(x,y)|^2 = \left(\frac{1}{P}\int_0^L Re(E(x,y,z)\, e^{j\left(\frac{2\pi n}{P}\right)z})dz\right)^2 - \left(\frac{1}{P}\int_0^L Im(E(x,y,z)\, e^{j\left(\frac{2\pi n}{P}\right)z})dz\right)^2 \quad (2.26)$$

2.1.3 Determinantal equation

The two equations from the electronics and circuits methods of analysis, (12) and (20), can be combined to arrive at the dispersion relation, without space-charge.

$$\frac{\beta_e}{(\beta_e-\beta)^2}\frac{\beta^2\beta_e}{\left(\beta_c^{\,2}-\beta^2\right)}2C^3 = 1 \quad (2.27)$$

The pierce parameter, C, has been introduced, which establishes an easy relationship between the beam parameter, I_0 and V_0 and the circuit coupling impedance, K.

$$C = \frac{KI_0}{4V_0} \quad (2.28)$$

With space charge,

$$\frac{\beta_e}{\left[(\beta_e-\beta)^2 + \frac{\omega_q^2}{v_0^2}\right]}\frac{\beta^2\beta_e}{\left(\beta_c^{\,2}-\beta^2\right)}2C^3 = 1 \quad (2.29)$$

2.1.4 Gain equation

The determinantal equation (2.29), a fourth-order polynomial equation for *b,* is used to determine the gain in the circuit. The determinantal equation will have four solutions, corresponding to four modes of the circuit. The solution of the determinantal equation is considered under synchronous operation, such that $\beta_c = \beta_e$. The two modes travel slower than the speed of the light: one has an exponential growing nature and another a decaying exponential. The remaining two modes travel with the speed of light: one forward wave and another backward wave. By solving the boundary and initial condition, Pierce shows the gain, G, in a TWT which is a result of the slow forward growing wave,

$$G = 10\log_{10}\left(\frac{1}{3}e^{\frac{\sqrt{3}}{2}C2\pi N}\right)^2 \quad \text{[dB]} \qquad (2.30)$$

where, $N = 2/(\pi\beta_e)$ is the number of longitudinal wavelengths in the circuit and C is the Pierce parameter. The fraction amplitude scaling of $1/3$ results from the fact that only one-third of the wave couples into the slow forward growing wave. The other $2/3$ is lost to the decaying slow-wave and forward fast-wave.

2.2 H-plane and E-plane loaded SWS

Having discussed in the chapter-1, the reported SWSs have been found to have drawbacks either due to manufacturing difficulties or the lack of high-performance levels. The pros and cons of those SWSs are described in section (1.3) and section (1.4). The imaging and spectroscopy applications demand reasonable power from 0.1 W to tens of watts in the THz frequencies, particularly in the 400-GHz band.

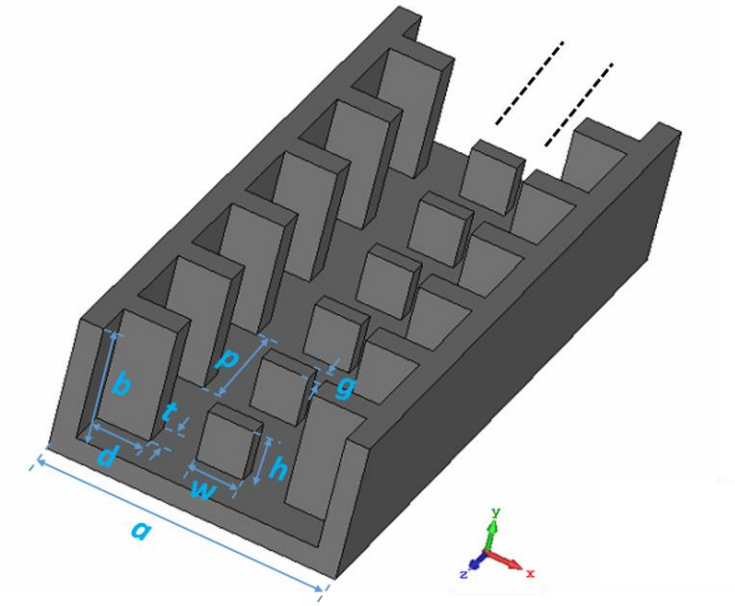

Figure 2.2: H-plane and E-plane loaded SWS for 400-GHz TWT (top metal cover is not shown).

Aiming for a robust design and easy to be fabricated, a novel SWS based H-plane and E-plane loaded is proposed for THz TWT. It is a variant design of existed E-plane corrugated SWSs. The additional H-plane load brings potential benefits to the THz TWT, such as its ability to support large beam current, the availability of more interaction fields to the electron beam, high output power, a wide bandwidth operation, and an easy fabrication by using available microfabrication methods together with this is all-metal structure. This type of all-metal structure can provide excellent thermal dissipation in the tube. It is a rectangular waveguide periodically loaded with metal corrugations, as shown in figure 2.2. Figure 2.3 shows the transverse field patterns of the rectangular waveguide when it is excited with the fundamental mode i.e. TE_{10}. The TE_{10} mode does not have a longitudinal electric field (here, the axial field), existing only in longitudinal magnetic fields. The axial electric fields are the only useful field component for the beam-wave interaction process in the TWT. A metal corrugation, which is on the broadside side ('*a*') of waveguide loads the transverse electric fields and creates a capacitive loading to the electromagnetic waves, which is called an E-plane load. Another metal corrugation, which is on the shorter side ('*b*') of the waveguide loads the transverse magnetic fields and creates an inductive load to the electromagnetic waves, is called an H-plane load. Due to the periodic loading, the fundamental mode becomes a hybrid

mode, which provides axial electric fields in the waveguide. Further, the loading effect causes the slowing down of the electromagnetic waves to catch up the electron beam travelling with a velocity less than the speed of the light.

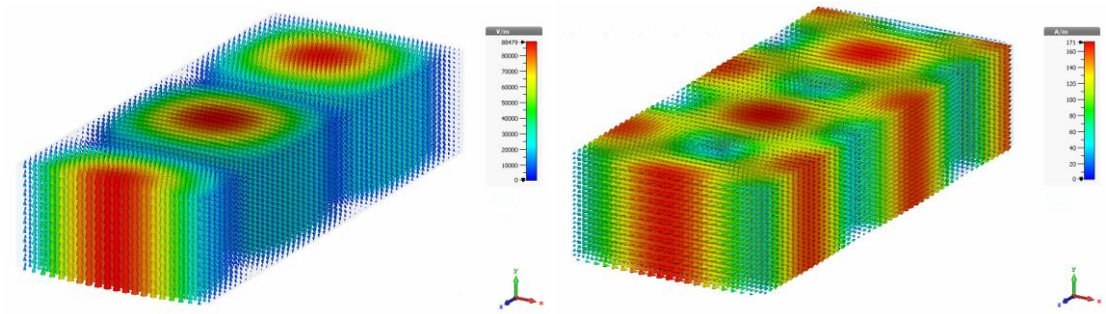

(a) (b)

Figure 2.3: Rectangular waveguide TE_{10} mode field pattern (a) transverse electric field, (b) transverse magnetic field.

The proposed H-plane and E-plane loaded SWS is designed for 400-GHz TWT. The design and performance of the SWS are discussed in the next section.

2.3 Electromagnetic analysis

2.3.1 Eigenmode simulations

To begin, a unit cell of the truncated H-plane and E-plane loaded SWS is considered for electromagnetic analysis. An Eigenmode solver of microwave studio module of CST software is utilized. From this simulation, the electromagnetic properties of the SWS can be analysed, such as Eigenmodes, field contour, dispersion behaviour and interaction impedance. These are all necessary parameters for further investigation of TWT performance. Since a unit cell of the periodic structure is considered, Fluent boundary condition i.e. periodic boundary condition is applied to the direction of the repetition side (figure 2.4).

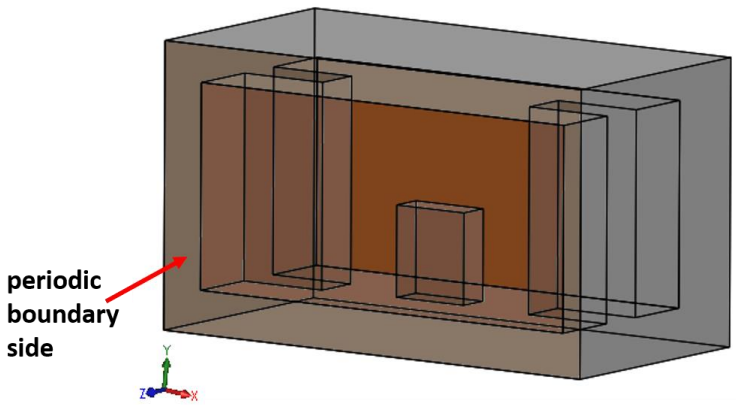

Figure 2.4: Unit cell of truncated H-plane and E-plane loaded SWS.

Table 2.1: Design parameters of the unit period of the SWS for 400-GHz TWT.

Parameters	Dimensions (μm)
a	520
b	254
p	240
w	100
g	40
h	113
d	115
t	60

By sweeping the phase difference between the repetition sides, the solver calculated the Eigenmodes and provided the electromagnetic field values to those Eigenmodes. The parameters of the SWS are tailored in order to obtain linear dispersive characteristics at around 400 GHz centre frequency. Table 1 is given the optimized parameters of the SWS. Firstly, the two modes of SWS is shown in figure 2.5. The fundamental mode (TE_{x10}) is obtained from 345 GHz to 455 GHz, whereas the next higher-order mode (TE_{x20}) from 581 GHz to 692 GHz. It is a clear advantage that a large bandgap of 126 GHz between these two modes avoids band edge instabilities. The fundamental mode typically supports a larger power and wider bandwidth than the higher-order modes. It can also avoid the mode competition when the

tube operates in the fundamental mode. In order to operate at lower supply voltage and with optimum performance, the first space harmonic mode from 2π radian to 3π radian (forward wave) is chosen to be used for the wave amplification. A beamline is superimposed on the dispersion curve using the below equation (2.31):

$$V_e = \sqrt{\frac{2eV_b}{m}}, \omega = \frac{\varphi.5.93.10^5\sqrt{V_b}}{p} \qquad (2.31)$$

whereas, *Ve* is the electron velocity, *e* is the electron charge, V_b is the beam voltage, *m* is the mass of the electron, ω is the frequency, φ is the phase difference, and *p* is the length of period.

An ultra-wide range of overlap between the dispersion curve from 350 GHz to 440 GHz with that of beam-line assures synchronization condition for energy transfer from the electron beam to the wave. This overlap can predict the instantaneous bandwidth of the amplifier.

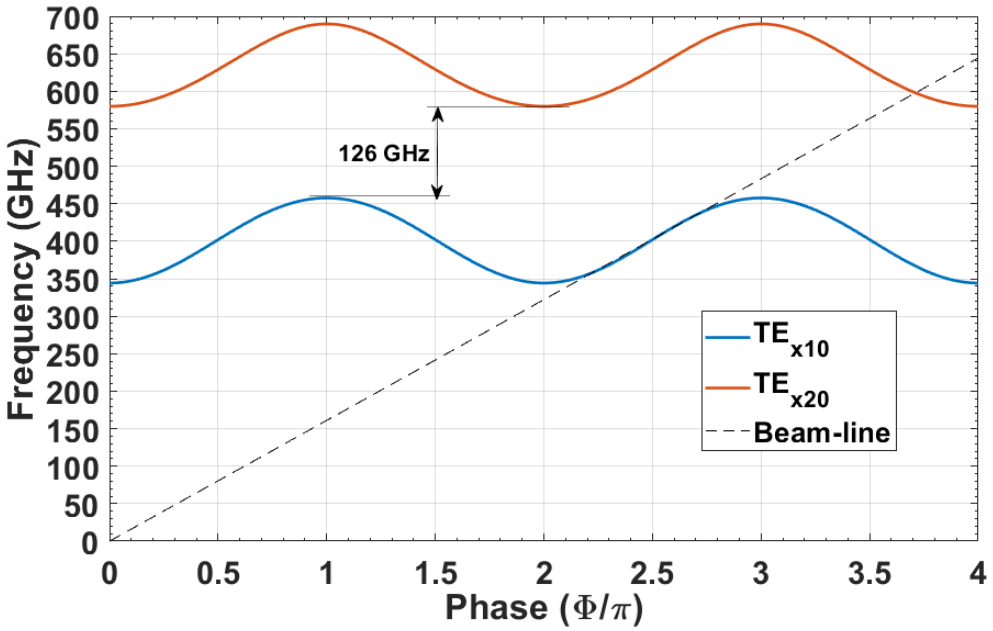

Figure 2.5: Dispersion curves corresponding to the fundamental mode (TE_{x10}) and higher order mode (TE_{x20}).

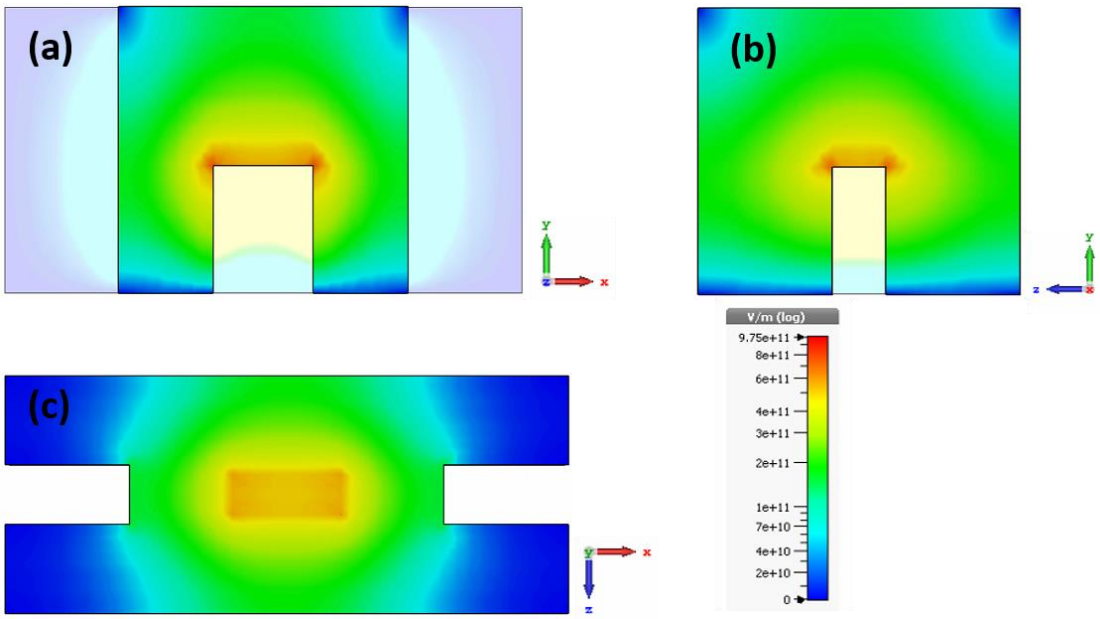

Figure 2. 6: Longitudinal electric field (E_z) distribution in the unit cell of the truncated SWS: (a) front view, (b) side view, and (c) top view.

The interaction impedance is an important trait in TWT design, which measures how much of the electromagnetic field is available for the beam-wave interaction for given SWS. The interaction impedance is calculated using an equation (2.23). The parameters, such as axial electric field, power flow, group velocities, are obtained from the post-processing of the Eigenmode simulation.

Figure 2.6 shows the longitudinal (axial) electric field distribution in the unit cell of the SWS, which reveals that the concentrated electric field over the tip of the E-plane corrugation can be used for the beam-wave interaction. Thus, the placing of an electron gun is considered above the E-plane corrugation so that the electron beam transmits over the E-plane corrugations. Figure 2.7 shows the surface current in the unit cell of the truncated SWS.

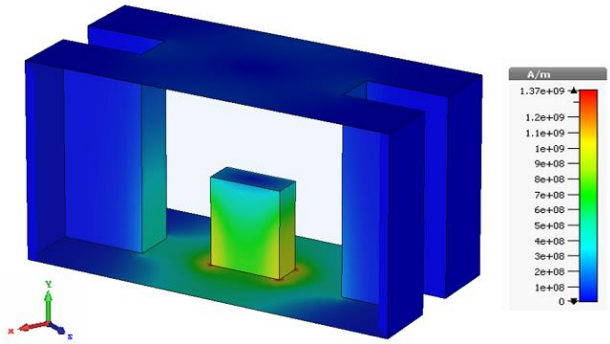

Figure 2.7: Surface current in the unit cell of the truncated SWS.

According to the electric field availability, the cross-section of the electron beam emission is chosen as 100 µm × 60 µm, which is a distance of 40 µm from the tip of E-plane corrugation to the axis of the electron beam. The harmonic space component of the axial electric fields is calculated over a cross-section area for calculating the interaction impedance. The interaction impedance is studied for different values of the parameters of the H-plane corrugation such as width '*d*' and thickness '*t*', shown in figure 2.8. It is noted that interaction impedance is improving for increasing the value of '*d*' and '*t*'. This is due to the incorporation of addition H-plane corrugation to the E-plane corrugated SWS. Hence the higher the interaction impedance indicates a better energy transfer occurs in the TWT, resulting in higher power output.

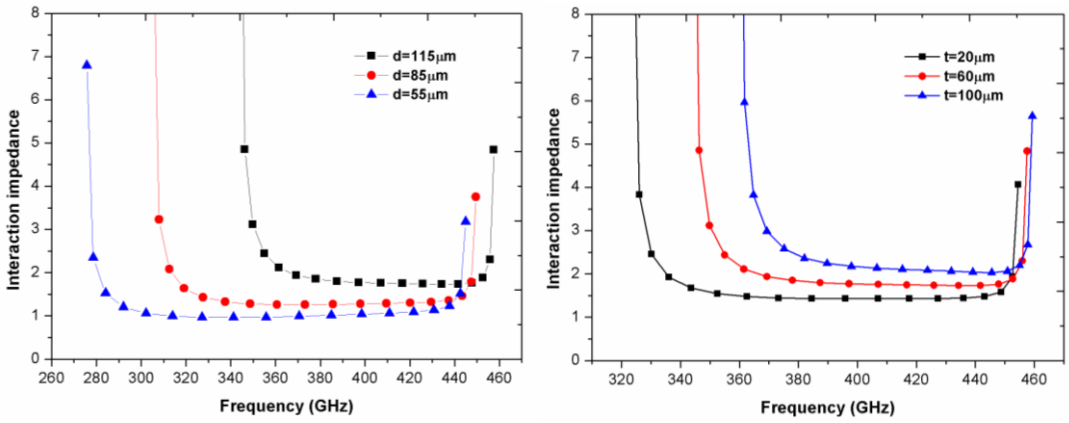

(a) (b)

Figure 2.8: Interaction impedance of the SWS, (a) for changing '*d*', and (b) for changing '*t*'.

For instance, the skin depth of the electromagnetic wave of tube operating frequency at an upper frequency, 455 GHz, is 97 nm, assuming OFHC (Oxygen-free high conductivity) copper. The surface roughness of the conductive planes within the fraction of the skin-depth or more explains the RF power loss in the SWS. Due to the practicalities of the tube application, no microfabrication technique can produce the ideal surface planes (for example, >10 nm). Therefore, using the equation (2.32), the effective conductivity of copper for different values of surface roughness is plotted, as shown in figure 2.9.

$$\sigma_{\text{eff}} = \frac{\sigma}{\left(1+\exp\left(-\left(\frac{\delta}{2R_q}\right)^{1.6}\right)\right)^2} \tag{2.32}$$

Where, δ the skin depth, R_q is rms surface roughness, and σ is the conductivity of the pure metal.

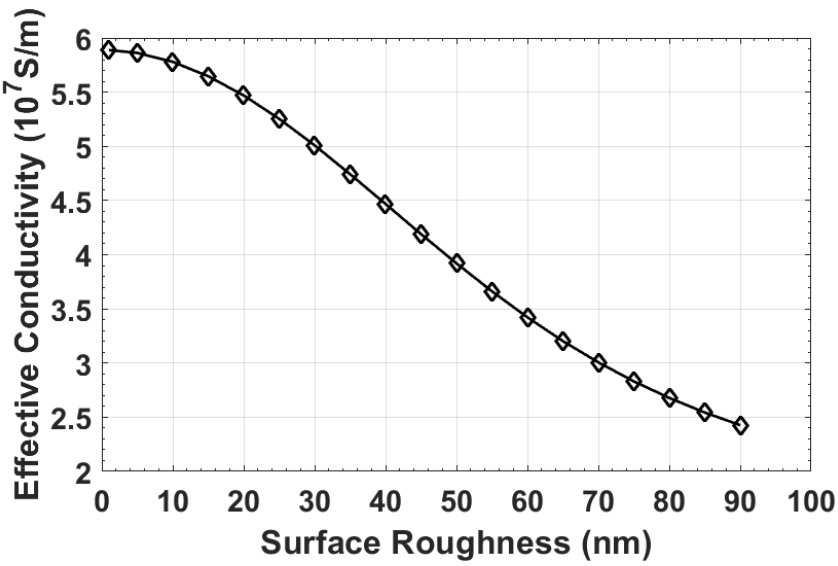

Figure 2.9: Effective conductivity of copper for changing in surface roughnesses.

The effective conductive value, 3.6×10^7 S/m, instead of OFHC copper (5.89×10^7 S/m) is chosen for PiC simulations, which corresponds to surface roughness of 56 nm.

2.3.2 Coupler design

The external circuitry of the THz TWT is fed through the rectangular waveguide. It is not possible to connect the SWS directly to the external rectangular waveguide connector because there is always a wave-impedance mismatch at the interface. A transition structure or a coupler is essential to transform the fundamental mode of the waveguide connector to the slow-wave mode in the SWS at the input side and vice versa at the output side. The coupler should ideally retain full intrinsic bandwidth of the SWS.

The coupler geometry is shown in figure 2.10 (a). However, this design posed complexity in fabricating the coupler along with the SWS in a single LIGA step. This is because it has vertical transitions in the E-plane corrugations. In order to avoid alignment problems associated with the assembling of the couplers to the SWS, the coupler is designed such that both the couplers and SWS can be easily fabricated using the same MEMS fabrication technique and with the same number of process steps in a single substrate. The modified coupler geometry is shown in figure 2.10 (b).

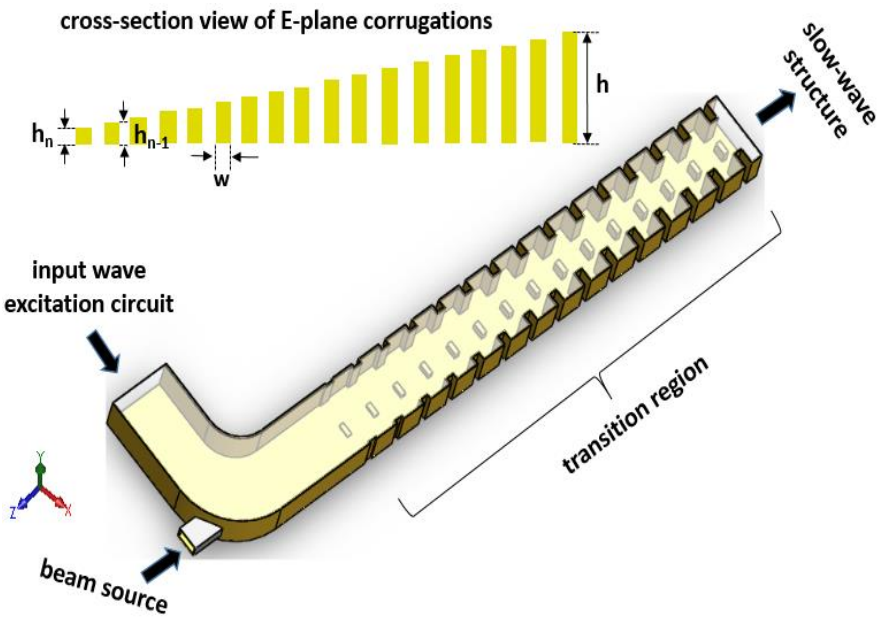

(a)

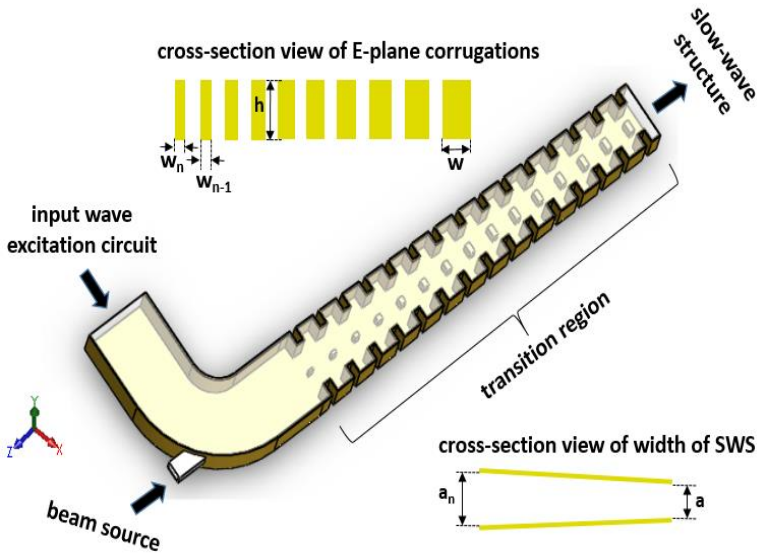

(b)

Figure 2.10: Schematic of Coupler designs: (a) design-1 and (b) design-2.

The modified coupler has two different structural transitions: a transition in the E-plane corrugation width '*w*' and another transition in the broadside of waveguide width '*a*'. The difference in width between the successive E-plane corrugations is 10 µm ($w_n - w_{n-1}$) and the extreme ends of tapered SWS broadside widths are '*a*' and 'a_n = 1.25a'. The height of the coupler and the SWS are the same, 254 µm, which is chosen according to the WR-02 waveguide flange [1]. The structural transitions at the input side smoothly converge the rectangular waveguide mode of RF excitation to the slow-wave mode in the interaction section. Similarly, in the output section, it happens in reverse order. If it is not matching perfectly, the signal is reflected back to the input. A 90° H-plane bend is implemented in the coupler design to isolate the electromagnetic wave excitation and the electron beam source. Similarly, a bend is used at the output coupler to isolate the beam collector and the wave extract port. For the coupler study, 10 uniform periods are considered and assumed an ideal conductor.

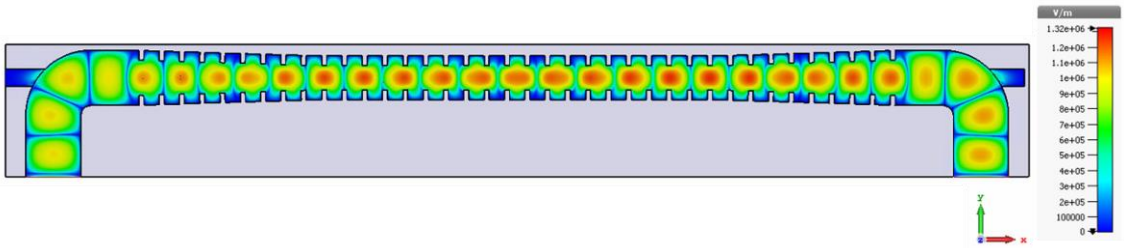

Figure 2.11: Electric field contour inside the coupler along with the SWS.

A time-domain transient solver in the CST microwave studio is used to investigate the coupler characteristics. The electric field contour of the coupler is shown in figure 2.11, which reveals the wave transition at the tapered configuration. Figure 2.12 shows the S-parameters of the coupler integrated with SWS. The modified coupler design (design-2) showed the best coupling property over the initial design. The reflection coefficient, S_{11}, is less than -15 dB over operating band 360 GHz – 440 GHz, which assures 100% power coupling for intended frequency bandwidth. Therefore, this design showed an excellent wave matching property for 80% of the intrinsic bandwidth. The transmission coefficient, $S_{21,}$ reveals a very good transmission over the operating band.

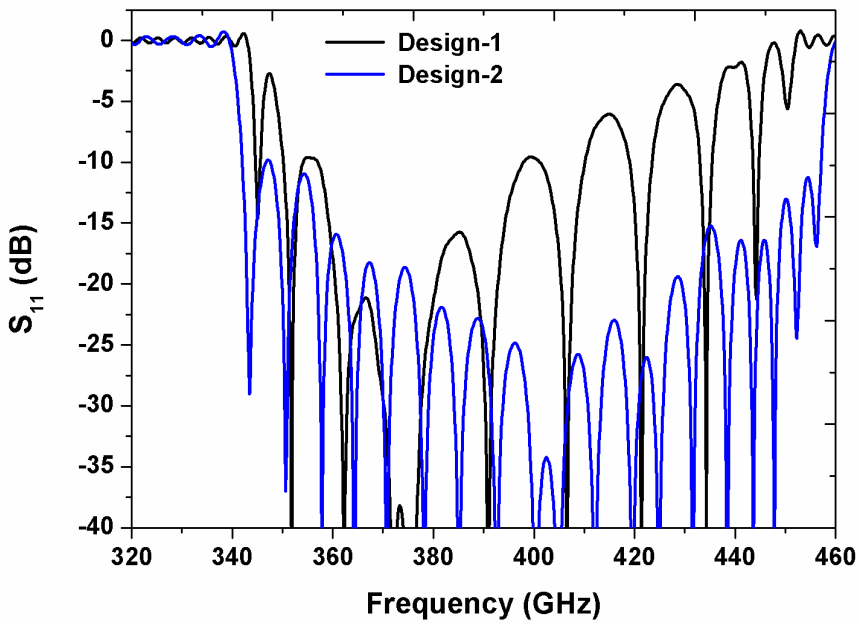

(a)

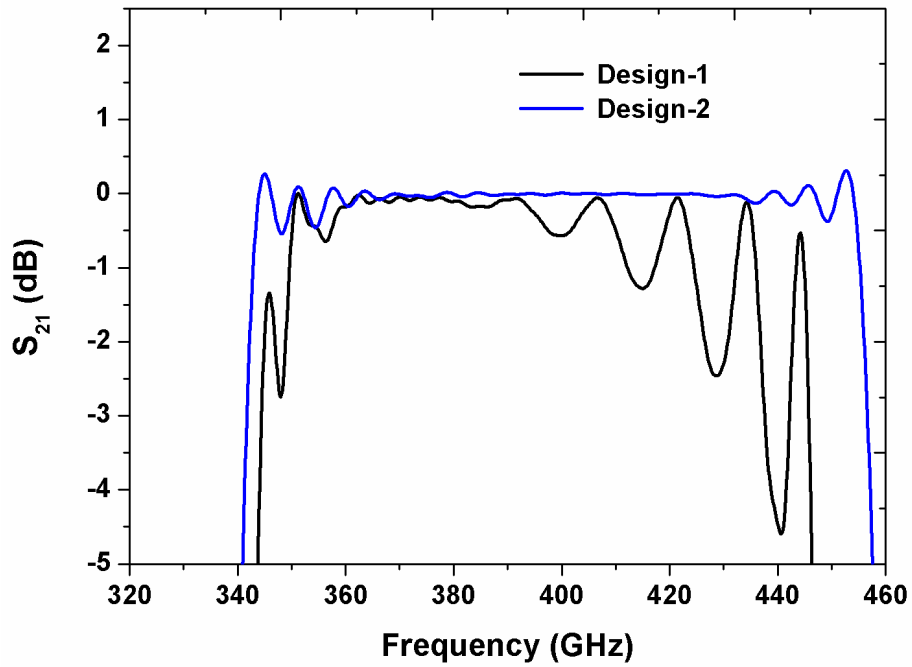

(b)

Figure 2.12: S-parameters of the Couplers: (a) reflection coefficient, S_{11}, (b) transmission coefficient, S_{21}.

2.4 Particle-in-cell simulations

A PiC solver of the particle studio in the CST is used to analyze the TWT performance based on H-plane and E-plane loaded SWS including the electron beam source, and focusing magnetic field. The PiC solver solves Maxwell's equations and the Newton-Lorentz equation for reaching the electron particle self-consistently. The electron particles exist in a continuum space and interact with electromagnetic fields through discrete mesh points using interpolation. The solver altogether includes the electron beam dynamics and non-linear effects in the simulation domain.

From the electromagnetic analysis or beam-absent study of the SWS, a set of structural parameters and coupler design were obtained. These were the basis for undertaking further investigation of the beam-wave interaction to demonstrate the TWT performance accurately.

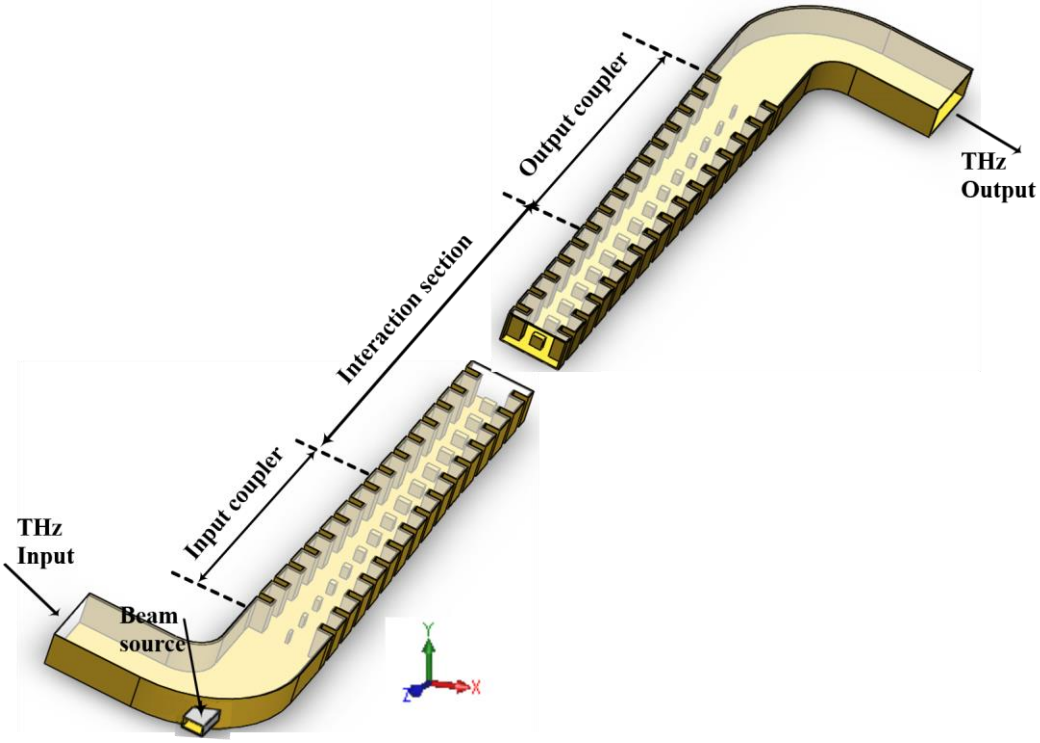

Figure 2.13: TWT amplifier model for PiC simulations.

For PiC simulations, the simulation model comprises a complete setup of TWT, such as the electron beam source, the SWS, input coupler, output coupler, collector, input and output port definition and magnetic focusing setup, as shown in figure 2.13. The dimensions of the SWS and the coupler designs are adopted from the preceding sections. A reduced conductivity of OFHC copper, 3.6×10^7 S/m, is assumed by accounting for the attribution of the surface roughness from the fabrication. A conducting surface is modeled as an electron beam emission source from where electron particles are launched and entered the SWS region. The dimension of the electron-emitting surface is the same as the value used for the interaction impedance calculation, 100µm × 60µm. The properties of the electron beam source are defined with a current of 20 mA (current density of 333 A/cm^2) and a voltage of about 17 kV. A 0.6 T uniform magnetic field in the axial direction is defined as a focusing field to confine the electron beam in its defined path during the interaction process. The value of magnetic field chosen is twice the Brillouin value. Brillouin's formula is given in the equation below:

$$B_{bri} = \sqrt{\frac{\sqrt{2}I_0}{wt\gamma\varepsilon_0\eta^{3/2}V_0^{1/2}}} \tag{2.33}$$

where I_0 is the beam current, V_0 is the beam voltage, ε_0 is the permittivity in a vacuum, η is the electron charge mass ration, γ is the relativistic factor, and w and t are the width and thickness of the sheet beam, respectively. The spent electron particles are collected at the tail end of the SWS. The mesh optimization is performed with respect to the longitudinal electric field, compromising the simulation accuracy and computer resource utilization. The mesh optimization is also done to the electron emission surface, which decides the number of emission points in the simulation run. It is noted that the 57×10^6 particles are used at each time step in the PiC simulations. The small-signal PiC simulations are performed with an input continuous sinusoidal signal peak power of 50 mW at 400 GHz frequency.

2.4.1 Uniform profile configuration

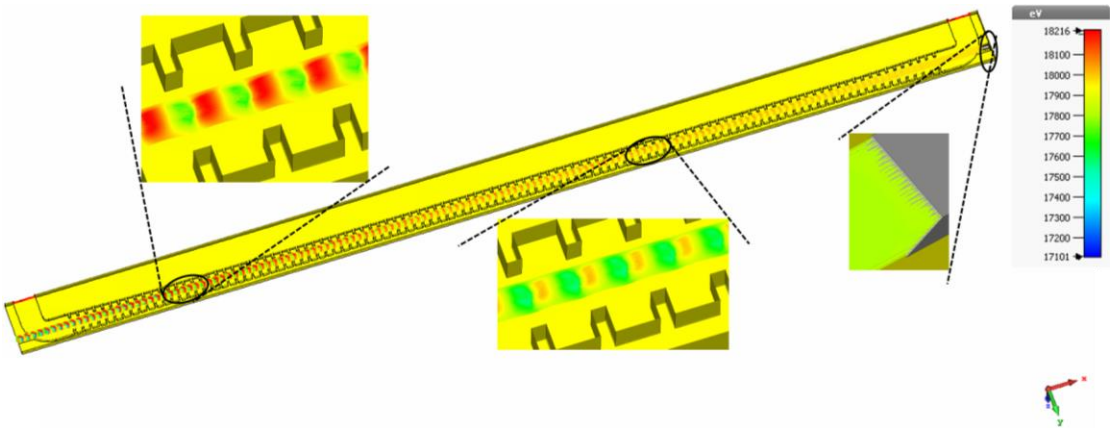

Figure 2.14: Electron beam trajectory in the SWS.

Figure 2.14 shows the electron beam trajectory in the SWS. It can be observed that the progression of the velocity modulation of the electron as it travels from the input end to output end increases. The bunching of electrons gets intensified as it travels. The bunched electrons transfer part of their kinetic energy to the electromagnetic wave during the decelerating phase of the wave.

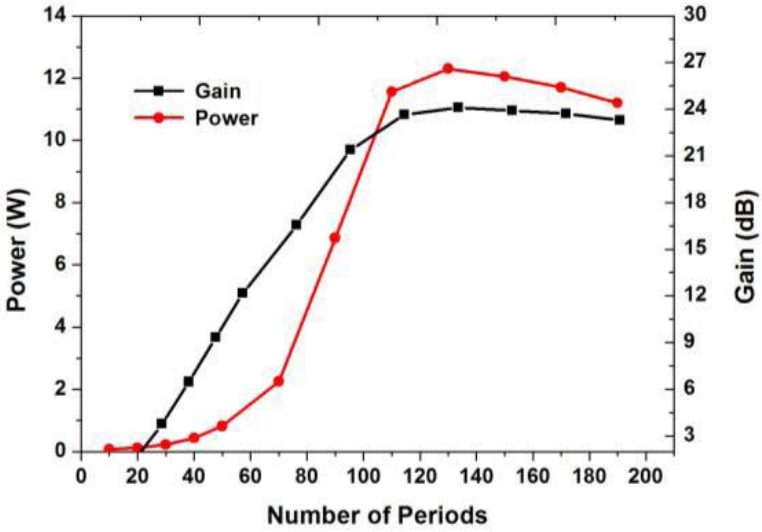

Figure 2.15: Output power and gain vs. length of the SWS.

Figures 2.15 shows the power and gain of the TWT with respect to the length of the SWS. A gain of 23 dB is achieved for the length of 130 periods. It is observed that after the 130-periods length of the SWS there is a decline in the gain and the output power. The periodic interaction process causes the retardation of the moving electron beam after giving up part of its kinetic energy to the wave. This retarded electron beam starts to see an accelerating phase of the wave, where the acquired wave energy gives back to the electron beam. This means that the synchronism condition between the electron beam and the wave no longer exists.

2.4.2 Phase velocity tapering

The phase velocity tapering technique is employed to resynchronize the velocity match. This technique is used to tailor the phase of the electromagnetic wave to match with the electron beam velocity. To provide the phase matching, the profile of the unit period length is changed in the end part of the tube, from where the wave amplification starts to decline. The period configuration is shown in figure 2.16.

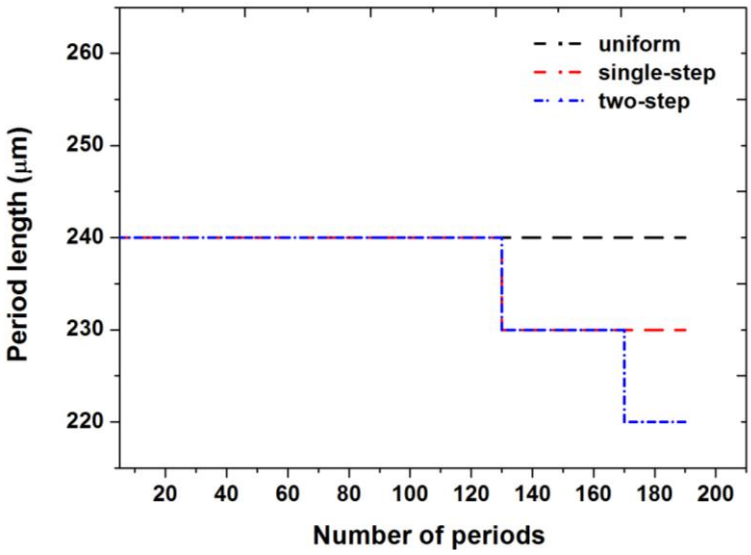

Figure 2.16: Period profile of the phase velocity tapering.

Two configurations are implemented: single-step and two-step. The single-step tapered configuration has a period length of 230 μm starting from 130-periods length of the interaction structure and continues until the end of the tube. In the case of the two-step tapered configuration, the period changes in two instances, at the 130-periods length and the 170-periods length with the period length of p = 230 μm and p = 220 μm, respectively. Compared to the uniform period, the tapered structure further extends the interaction of the velocity modulated beam with the traveling wave. The tapered configurations are optimized at the centre frequency of 400 GHz. An improved output power from 12.10 to 18.70 W with 54.55% increment is obtained with the single-step tapered configuration as compared to the uniform profile configuration. In the case of two-step tapered configuration, an increment of 67.35% in the output power is achieved with respect to the uniform period configuration and with the maximum output power and a small-signal gain up to 20.25 W and 25.92 dB, respectively. Between the two tapered configurations, the two-step tapered configured shows better performance in the beam wave interaction. This is because of extending the presence of phase-match phenomena between the beam and the wave by the change in the period length of p = 220 μm at the distance of 170th period. Hence, the simulations are performed for analysing the full bandwidth.

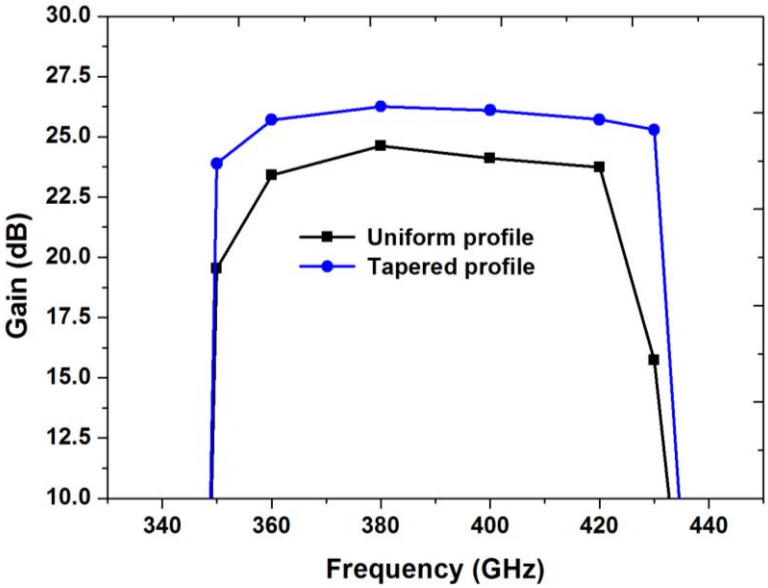

(a)

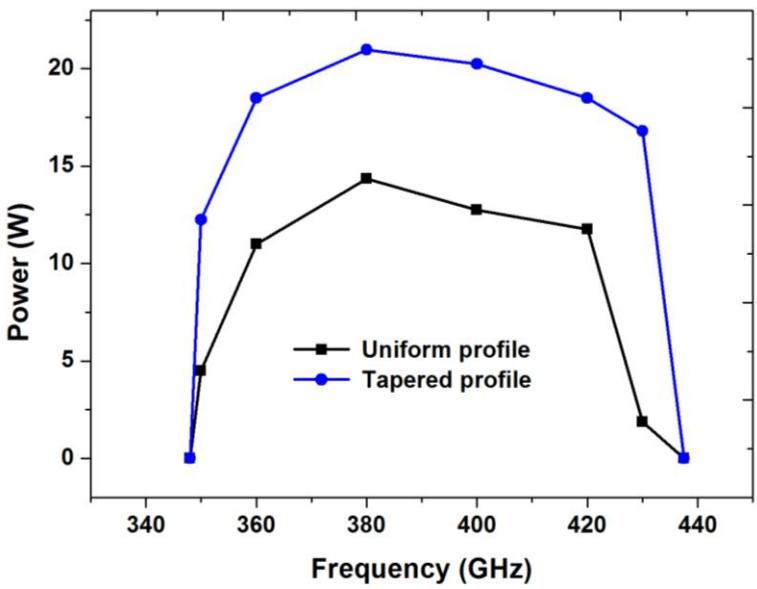

(b)

Figure 2.17: TWT performance comparison between the uniform profile and the tapered profile configuration: (a) gain vs. frequency, and (b) power vs. frequency.

Figure 2.17 plots the small-signal gain and output power over the operating band at 50 mW input power. As observed, more than 60% of the improvement in the output power is obtained in the frequency range 350 - 430 GHz for the two-step tapered configuration as compared to the uniform period configuration. An instantaneous bandwidth of 80 GHz with a small-signal gain of more than 25 dB is obtained. The large abrupt fall in gain

and power of the TWT at the lower and the higher frequencies is due to the mismatch between the velocity of the beam and the phase velocity of the wave.

Chapter 3

3 LIGA microfabricated H-plane and E-plane loaded SWS

The fully controlled and optimized parameters of applied fabrication technique is vital for the successful fabrication of SWS in the THz regime since the THz SWSs demand stringent fabrication requirements. This chapter presents the complete fabrication flow of UV-LIGA for fabricating 400-GHz H-plane and E-plane loaded SWS, from bare silicon to photolithography and electroplating, together with the post-processing of the processed samples. The critical fabrication conditions of KMPR photolithography will be discussed. A detailed study on KMPR mold, the morphology of copper microstructures, and an examination of diffusion bonded microstructures are included.

3.1 Process description

THz components demand very tight fabrication tolerances, and fine quality surface walls in order to achieve the desired wave propagation in the device. Skin effect loss has a detrimental effect at higher frequencies. In chapter-1, the different microfabrication techniques for THz TWTs were discussed. It was found that MEMS techniques are the best solutions, as they can produce nearly perfect geometries in terms of aspect ratio, vertical profiles, pattern precisions and the quality of sidewalls. In particular, UV-LIGA is an attractive technique to realize the features from a millimetre down to a few microns for very thick metal structures. This technique uses a UV light source for the photolithographic process in conjunction with the electroplating. In the LIGA technique, as said in the chapter-1, the SU-8 had been widely used as a structural layer and a mold material for micro-metal components. Due to its of mechanical stability, the SU-8 is more suitable as a construction material or an active device layer rather than mold material. In the application of SU-8 as the mold material, it is very cumbersome to dissolve or remove cross-linked SU-8 after electroplating. Hence, SU-8 is not a

favourable choice of material where the very thick metal microstructures making are needed.

A KMPR photoresist is a negative tone epoxy resit which is a chemically modified version of SU-8. The cross-linked KMPR photoresist is more vulnerable to dissolving in solvents. Therefore, it is potentially attractive in the micro-metal electroplating fabrication processes. Conceptually, the KMPR process for electroplating applications is similar to the SU-8 process, only differing in material properties so that the KMPR process requires optimization of a multitude of process parameters for the best photolithography results. The process parameters strongly depend on the type of geometry being fabricated, the minimum feature size and thickness of the film.

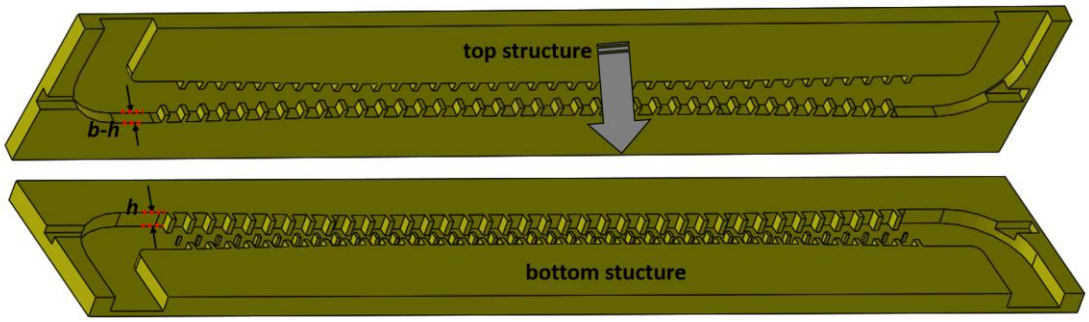

Figure 3.1: Schematic representation of the SWS parts divided into two for LIGA fabrication.

The design of the H-plane and E-plane loaded SWS has two distinct heights of topology, and that including the top of the structure has to be enclosed with flat metal (figure 3.1). A step feature of *E*-plane corrugation height (‘*h’)* of 113 μm is one, and the other is the height of the *H*-plane corrugation and the associated waveguide walls *b=254* μm. A two-level LIGA process is required for this type of distinct height structure fabrication. The two-level LIGA process includes repetition of the entire LIGA procedure, and the additional requirement of aligning the first and the second layer is necessary. The first layer is for realizing the structure features up to a height of h=113 μm and the remaining features height of $b - h$ = 141 μm which can be done by a second level LIGA procedure.

The two-level LIGA presents severe challenges. The KMPR mold created from the first-level LIGA can become hard-baked during the heat treatment in the second LIGA procedure. The hard-baked KMPR mold is hard to strip during the photoresist removal phase. In order to obtain precise alignment between the two layers, the surface of the first-level-LIGA-fabricated wafer must be smooth and levelled for the subsequent fabrication step. An alternative approach is considered to make the fabrication process easier. In this approach, the features of the two distinct heights are fabricated in separate wafers, and each follows the same LIGA procedure. Finally, face-to-face features are bonded for completing the full device fabrication, as shown in figure 3.1. Figure 3.2 illustrates the UV-LIGA fabrication process flow to be implemented.

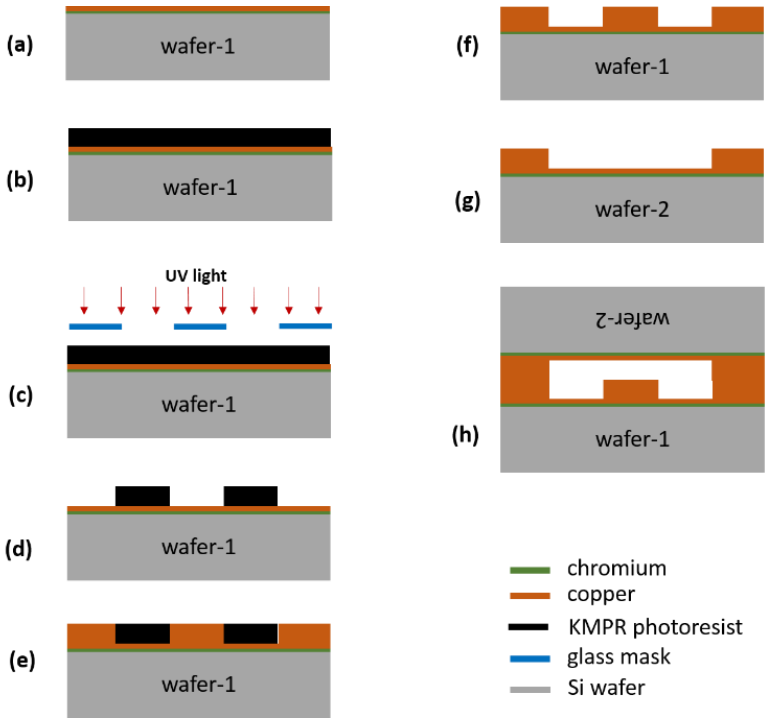

Figure 3.2: Fabrication flow diagram of SWS for LIGA technology.

The required process steps are described as follows:

(a) The first step is the metallization of the silicon wafer (wafer-1) with copper thin film and aluminium used as a seed layer between Si and copper. Before that metal coating, the Si wafer was carried with a standard cleaning process.

(b) KMPR photoresist is applied onto the wafer and spun with appropriate speed. The spin speed is determined by the type of photoresist series used, and the desired thickness of the film. The Si wafer with deposited photoresist is then subjected to a soft bake on a levelled hot plate to drive off the solvent.
(c) The KMPR photoresist is then exposed under UV light through a glass mask that defines a 2-D pattern of the SWS. By projecting UV light, the pattern is transferred from the mask to the photoresist.
(d) A post-exposure bake process, typically for the negative photoresist, is performed to produce cross-linking reactions. These cross-linked regions will be insoluble in the developer. Development is then employed to remove unwanted KMPR.
(e) The electroplating experiment is conducted to deposit metal around the open region of the mold and up to the height of the mold. The processed wafer was diced, and the individual dices were lapped and polished to the desired thickness.
(f) Then the KMPR is etched from the electroplated samples to obtain the bottom metal structure of the SWS.
(g) The steps from (a) to (f) are repeated on another Si wafer (wafer-2) with a different photomask, which has 2D patterns of the top structure of the SWS.
(h) Diffusion bonding is employed to attach the top and bottom structures of the SWS to realize the full device.

3.2 Fabrication conditions

The process parameters of KMPR lithography are quite different from the protocols suggested by the manufacturer. The parameters are totally dependent on the geometry of the structure, cleanroom conditions and equipment used. In this section, detailed process conditions are discussed.

3.2.1 KMPR process

Particle-free wafer surfaces is an essential requisite for successful fabrication. Therefore, before the KMPR process begins, wafer pre-treatment must be carried out. Wafers were first cleaned with solvents to rid of the organic residues and later treated

to a plasma environment to improve the adhesion between the Si and stack of thin metal films deposited in the subsequent process. In the cleaning phase, wafers were cleaned with acetone and isopropanol, then rinsed with DI water and finally blown wit N_2 gas.

3.2.1.1 Metallization

Copper was chosen as a material for the conductive path, and it also serves as a bottom conductive layer for the device. Therefore, copper must be deposited several skin-depths of the highest device operating frequency, 450 GHz. Chromium has excellent adhesion properties to many metals including copper. Therefore, it is used as a buffer layer between Si and copper thin film to improve the adhesion. The quality of the thin films and uniformity of deposition much depends on the physical mode of operation. Besides this, the rate of deposition is also significantly influenced. Two different approaches were used for the thin metal film deposition. One is by using the thermal evaporation (Moorfield Minilab T25M) for depositing the chromium and copper. Another approach is by using a Sputter system (AJA sputter 4050) from AJA International Inc., which has an integrated sputter and e-beam system. The sputter and e-beam sources of AJA sputter 5050 were used for the copper and chromium deposition, respectively. The depositions were performed in a single go through rather than in separate time steps.

The deposition rate of chromium was 0.2 Å/sec for a thickness of 20 nm. Initially, the deposition of copper was performed at a low rate of 0.75 Å/sec for 50 nm thick for attributing strong binding between copper and chromium. Later the deposition rate was increased to 0.75 Å/sec up to a thickness of 250 nm. It was noticed that deposition by the DC sputter exhibited a superior quality over the thermal evaporation, which was verified by the scratch test. Peeling off the copper thin film from Si wafer from some of the experimental runs was observed, which were deposited by thermal evaporation, as shown in figure 3.3.

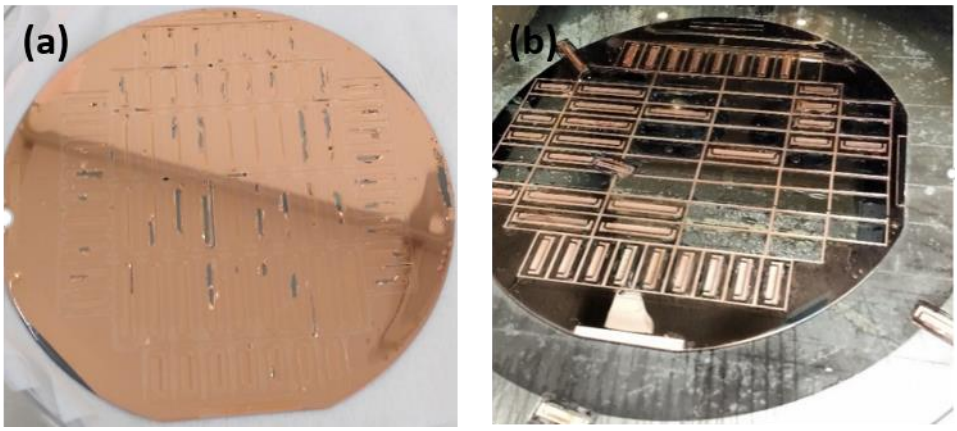

Figure 3.3: Peeling off of the copper thin film from Si wafer: (a) after KMPR developed, and, (b) after copper electroplated.

3.2.1.2 KMPR Deposition

The photoresist used for device fabrication is the KMPR-1050 series, which is the highest viscous photoresist in the KMPR series, developed by MicroChem. The photoresist must be stored in the freezer at the temperature of -15 ˚C. It then has to be kept outside the freezer for 24 hours to bring the photoresist temperature to room temperature before use.

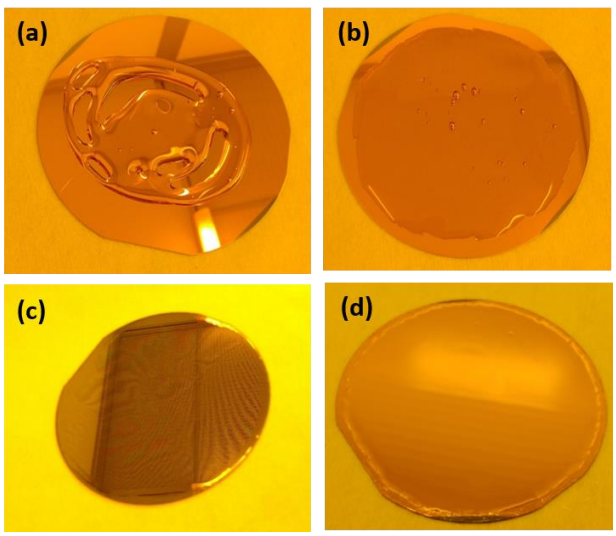

Figure 3.4: KMPR photoresist deposition process : (a) KMPR dispensed on the wafer, (b) KMPR covered 90% surface area, (c) after spin coating, and (d) after edge bead removal.

The spin coating method was employed to deposit a KMPR thick film, which is the more controlled method for achieving the desired thickness level than the casting approach in this case. The process of spin coating is shown in figure 3.4. A weight of approximate 4 ml of photoresist was poured manually on the wafer in a spiral pattern to cover most of the wafer surface. In order to improve the homogeneity, the wafer was tilted with an angle of 60° - 75° to spread the photoresist to cover 90% of the wafer surface before placing the wafer on a spinning chuck. To obtain a desired thickness of the photoresist coating, the final speed and time of the spinner were optimized. Subsequently, the wafer was rested for 30 min on the levelled surface to reflow the photoresist to enhance the homogeneity. It was noted after the soft-bake step that the edge of the wafer was protruding with the photoresist coating approximately 20-30 µm more than the rest of the wafer, which is called edge beading.

The presence of the edge beading creates an air gap between the photoresist and the mask, which causes a diffraction effect of the UV light during the exposing (shown in figure 3.5 (a)). Due to light diffraction, it deteriorates the pattern transfer and the lithographic resolution. The edge bead can be eliminated by solvents spreading over the extruded area while spinning the wafer at a very low speed in a separate spin step. It is a complex process to make an additional setup in the spinner for the application of solvent over the edge of the wafer. A simple method of manual removal was adopted, in which photoresist was removed over a 5-10% diameter area on the periphery of the wafer. The pattern of the deposited photoresist and its thickness profile before and after the edge bead is shown in figure 3.5 (b). It worked well at the laboratory level but is not attractive enough for the industrial process.

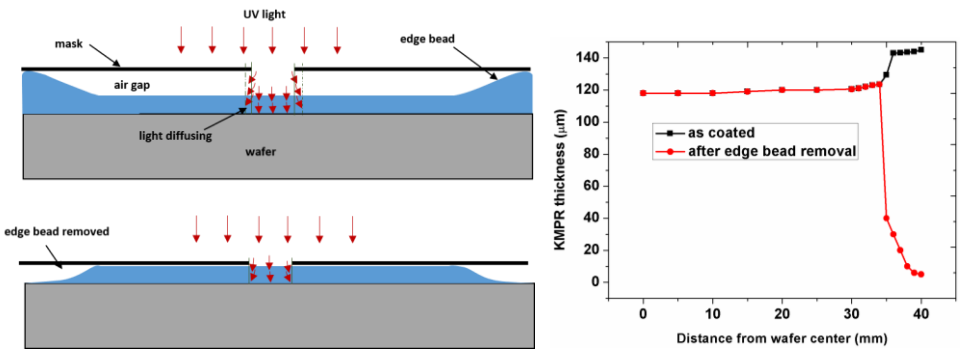

(a) (b)

Figure 3.5: KMPR film thickness study with edge bead and with EBR: (a) Light diffusion effect, and (b) edge bead effect from spin coating for 120µm thick KMPR film.

A single spin deposition was used for the bottom structure of the SWS, to obtain a 120 µm thick film. For the top structure of the SWS, a double spin deposition was used to obtain a 150 µm thick film, which is a stack of 30 µm and 120 µm film thicknesses. The spin parameters are summarized in Table 3.2.

Table 3.2: Spin parameters for the bottom and top structures of the SWS.

Deposition method	Final spin parameters		Structure
	Speed (rpm)	Time (sec)	
Single deposition	1100	30	bottom structure
Double deposition	3600	30	top structure
	1100	30	

3.2.1.3 Soft-bake

As the coated photoresist film is wet, it must be baked to evaporate the solvent content. The right amount of solvent content is required to avoid adhesion to the contact mask during the UV exposure and to enhance the photolithography performance by reducing the diffusion of the photo-initiator. A two-level procedure of baking was adapted unlike the one temperature level recommended by the manufacturer. In the first step, the photoresist is baked at 65 ˚C for a short duration to reflow the photoresist for improving the homogeneity. The second step baking was done at 95 ˚C for a more extended period to evaporate the solvents. Following this, the wafer was allowed to cool down for 30 min until it reached room temperature, which helps the photoresist be dried and the diffusion of heat in the photoresist. The peeling of the photoresist mold was observed during the development step when the wafer was baked longer than the sufficient time due to the contest of solvents being too low, as shown in figure 3.3(a). On the other

hand, the shorter the duration, the more the protrusions in the structures during the development was observed, as shown in figure 3.6.

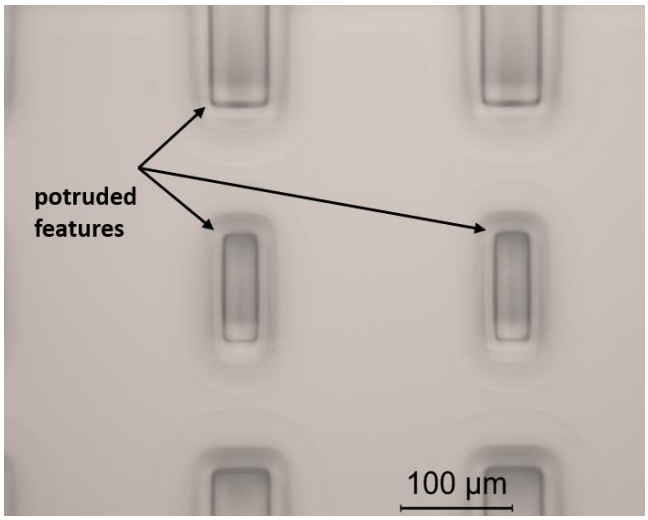

Figure 3.6: Optical microscopic image of protruded features of KMPR mold bottom structure of the SWS.

3.2.1.4 UV Exposure

A subsequent step in the photolithography after spin coat and soft bake is exposure of the UV-light onto the photoresist which initiates the cross-linking process. The photoresist is patterned by exposure through a mask that contains the features of the SWS. The mask was made in the form of a thin chrome layer on a glass substrate. Since KMPR is a negative tone resist, the regions where the photoresist is to be left on the wafer must be open on the mask. The exposing process was done using an EVG 620 mask aligner equipped with a mercury UV lamp.

The right amount exposing energy dose is essential for transferring the mask features into the photoresist. Furthermore, the choice of exposure light wavelength and the type of contact mode are also important. The amount of the required energy dose depends on the nature of the material beneath the photoresist, the thickness of the film, and the feature size of the mask pattern. The KMPR photoresist has a higher absorption rate near the 365 nm wavelength so an i-line filter was fitted into the Mask Aligner, which passes only 365 nm wavelength. Consequently, the filter enables a better

photolithography resolution. The soft-contact mode was utilized for UV exposing, where the wafer is pressed into contact with the mask. The lamp power was kept constant, and in which exposure duration was adjusted to apply the required energy. The UV intensity was measured as 15 mW/cm^2. In order to find the optimum energy for desired thicknesses, the experiments were conducted with different durations of exposure time. SEM was used to verify the KMPR mold vertical profile features. Figure 3.7 and figure 3.8 show the SEM images of the cross-section view of the mold of bottom structure and top structure of the SWS, respectively (obtained after development step).

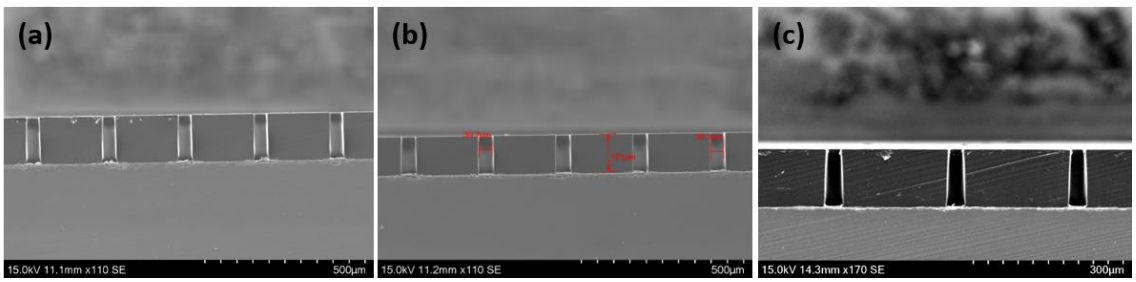

Figure 3.7: SEM images of the 120-µm thick KMPR mold of the bottom part of SWS: (a) 1500 mJ/cm^2, (b) 2000 mJ/cm^2, and (c) 2500 mJ/cm^2.

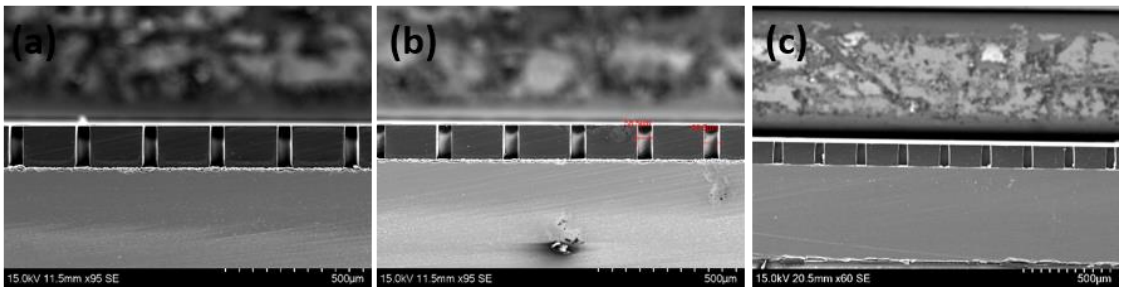

Figure 3.8: SEM images of the 150-µm thick KMPR mold of the top part of SWS: (a) 2500 mJ/cm^2, (b) 2750 mJ/cm^2, and (c) 3000 mJ/cm^2.

The energy dose of the 2000 mJ/cm^2 for bottom structure and 2750 mJ/cm^2 for the top structure was found to be optimum, since which it can provide nearly perfect 90^0 vertical structures. When applied energy was lower than the optimum value, a wider opening space at the bottom of the mold was obtained or looked like an undercut, as shown in figure 3.7(a) and 3.8(a). Moreover, because of insufficient energy, the bottom side layer

of the mold pattern was dissolved during the development process. Whereas when it was overexposed, a behaviour of T-topping was observed, as shown in figure 3.7(c) and 3.8(c). The T-topping was due to receiving more energy near the top portion of the photoresist layer than required and the diffraction of the UV light around edges of the pattern.

The initiated cross-linking reaction in the exposed regions by UV exposing was further energised by the thermal treatment in the post expose bake step. The cross-linked regions will be insoluble in the developer. The baking was done on a hot plate at a temperature of 90 ˚C. The parameters of both the UV exposure and post-exposure bake must be adjusted to receive enough energy for cross-linking reaction. The optimum parameters also help to avoid the resist delamination and deformation during the development. The wafer was rested for 30 min for thermal stress relaxation in the photoresist before the development step.

The non-cross-linked regions of the KMPR film were dissolved in the developer solution which is PGMEA (Propylene glycol methyl ether acetate). In the development process, two solution baths were used. The first developer, the coarse developer, was designed to remove the bulk of the uncross-linked KMPR. This bath usually has a relatively high content of KMPR. The second bath, the fine developer, was an aggressive cleaner. It was designed to develop small features, such as narrow trenches. After the final development step, the wafer was rinsed with Isopropyl alcohol (IPA) and bowled with N_2. The duration of the development was found by inspecting the wafers on the optical microscope at specific times during the development process. The large feature regions were dissolved quicker than the small features for a given thickness. It was observed that the time required for developing was increased when the post-exposure bake was done at an elevated temperature beyond 95 ˚C. It also caused difficulty in removing the photoresist in the small feature regions, and the large features result in undercuts. Pre-development relaxation time mitigates the generation of large cracks on the KMPR mold during development. It also minimizes the distortion of the shape of the features. Figure 3.9 shows the cracks generated in the KMPR molds due to the PEB at the high-

temperature and for a longer duration. The optimized KMPR process parameters for the bottom structure and the top structure are summarized in table 3.3.

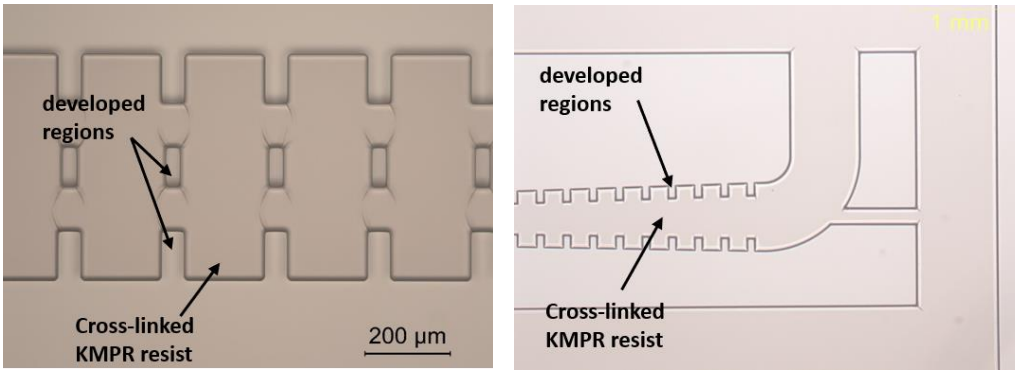

(a) (b)

Figure 3.9: Optical microscopic image of KMPR molds: (a) the bottom structure, and (b) the top structure.

Table 3.3: KMPR lithography process parameters for both the bottom and the top structures of the SWS.

	Soft-bake				UV exposure	PEB		Develo-pment
	Level-1		Level-2		Energy (mJ/cm^2)	Temp. (˚C)	Time (min)	Time (min)
	Temp. (˚C)	Time (min)	Temp. (˚C)	Time (min)				
Bottom structure	60	5	95	45	2000	90	8	13
Top structure	60	5	95	15	2750	90	8	16
	60	10	95	55				

3.2.2 Electroplating and KMPR removal

Electroplating is the preferred deposition technique for making thick micro-metallic parts. It is an electrochemical process in which the dissolved metal ions electrolytically transport from the anode through an electrolyte onto the cathode surface to be

deposited as a metal film. In the context of THz vacuum electronics, the choice of the metal for SWS fabrication needs to be copper. This is because copper is vacuum compatible, and it offers high electrical and thermal conductivity. The electroplating process is not routinely depositing metal to fill around the mold opening regions. The copper deposition must be lower porosity, purity of polycrystalline film, and with finer grain size, which effects the resistivity of metallization. Pulse electroplating plating can improve these properties compared to the traditional DC electroplating technique. In pulse electroplating, the current is alternated swiftly between two different values (figure 3.10(a)). Alternative ON and OFF periods of the constant current supply between the two values in pulse electroplating produces much better ions transfer into the cathode surface compared to the DC plating. In electroplating, a negatively charged layer is formed around the cathode as the process continues. When using the DC supply, this layer charges to a defined thickness and then it obstructs the ions from reaching the part. Pulse electroplating significantly increases the number of grains per unit area, which results in finer grain deposition with better quality than DC plating. Pulse electroplating can provide better control over the deposition process, by regulating the pulse amplitude, and ON and OFF widths.

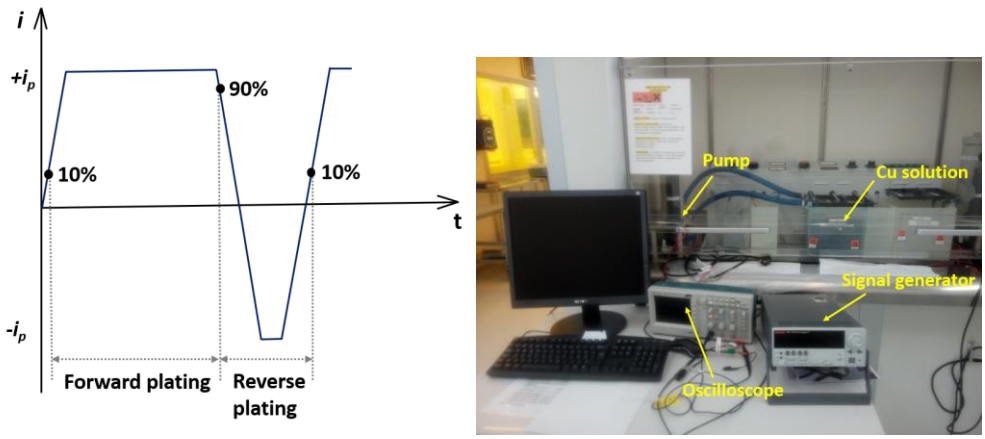

(a) (b)

Figure 3.10: (a) Shape of current pulse used in copper electroplating, and (b) Pulse electroplating setup.

A commercially available electrolyte solution from Dr.M.Kampschulte GmbH & Co. KG was used for the pulse electroplating experiments. The solution is a mixture of copper sulphate ($CuSO_4$), sulphuric acid (H_2SO_4) and copper chloride ($CuCl_2$), balanced with DI water. Also, solvent-free additives were added for bright copper plating and for eliminating voids. The electroplating set-up was equipped with a filter and agitator to move the electrodes laterally (figure 3.10(b)). The electrolyte solution circulates continuously through the filter using a pump. The electroplating experiments were done at room temperature. The cycle duration of the pulse was kept remain constant, 20 ms for a forward plating and 400 µs for a reverse plating for all experimental runs.

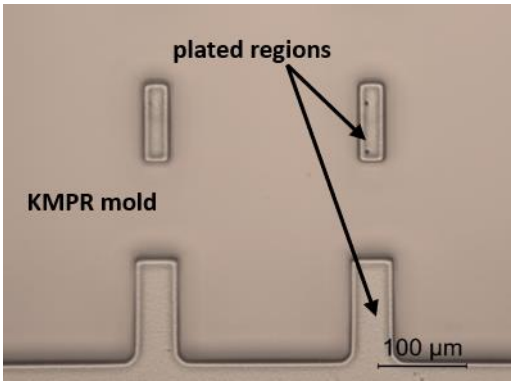

Figure 3.11: Optical microscopic image of copper electroplated around the KMPR mold before the mold removal step (bottom structure of the SWS).

Pulse copper electroplating experiments were conducted onto the KMPR molds and up to their height, provided with the current density of 15 mA/cm^2. Figure 3.11 shows the electroplated plated copper into the KMPR mold. Over deposition of copper was observed in some regains on the wafer, due to the difference in voltage potential. The electroplated wafers were diced using a DAD3240 (disco) dicer with a diamond blade to perform dice-level polishing and bonding in later stages. The bottom and top structures were diced in equal sizes. The individual dices were planarized to the desired thicknesses that define the 113 µm height of E-plane corrugations with side walls for the bottom structure and 141 µm for the top structure. A SiC-based sandpaper on a MultiPrepTM polisher from Allied was used with 0.1µm-Aluminum lubricant. After polishing, KMPR mold was stripped off in Remover PG. The Remover PG is a proprietary N-methyl pyrrolidinone (NMP) based solvent stripper. The solution was heated at 80 $^{\circ}$C for 30-40

minutes, and ultrasonic agitation was used to speed up the stripping time. After the stripping is done, the samples were soaked in IPA for 1-2 hrs and then in DI water for 30 min. The bottom and top metal structures after removing the mold are shown in figure 3.12 and 3.13, respectively. From these SEM images, it was evident that no residue of mold material was left, and no damaged metal features were observed.

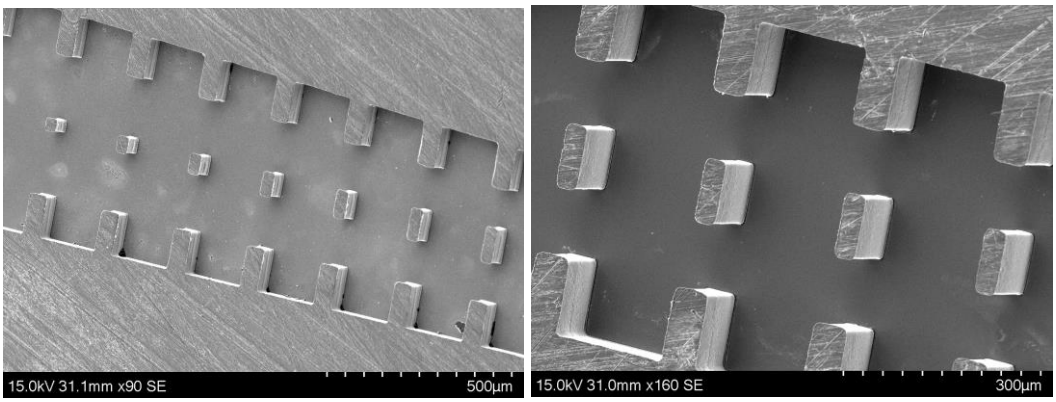

Figure 3.12: SEM image of the bottom copper structure of the SWS at a current density of 10 mA/cm^2.

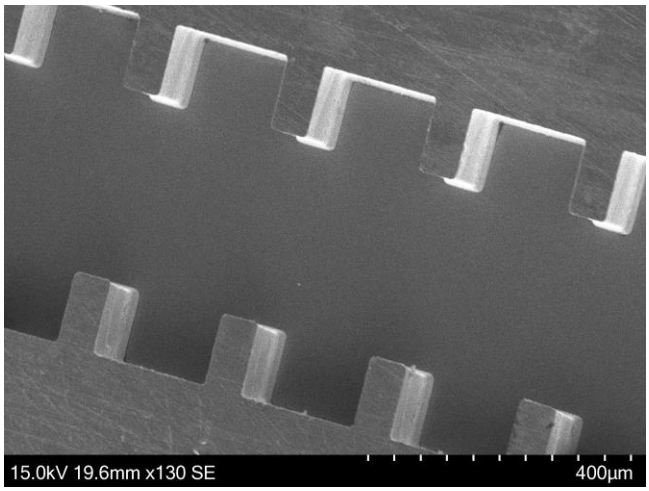

Figure 3.13: SEM image of the top copper structure of the SWS current density of 10 mA/cm^2.

3.2.3 Surface study

The applicability of the LIGA technique to the THz devices was studied by quantitative analysis of surface roughness on the sidewall of the processed samples. The optical microscope and atomic force microscope (AFM) were used for this analysis. The

electroplating experiments were performed for different values of current density, such as 5 mA/cm^2, 10 mA/cm^2 and 20 mA/cm^2 and keeping the other pulse parameters constant. The raw surfaces of the electroplated copper were investigated under the optical microscope. It is evident from figure 3.14 that the electroplated copper had a better and smoother surface when the current density was low, 5 mA/cm^2. This is because of the grain growth was done at a slower rate.

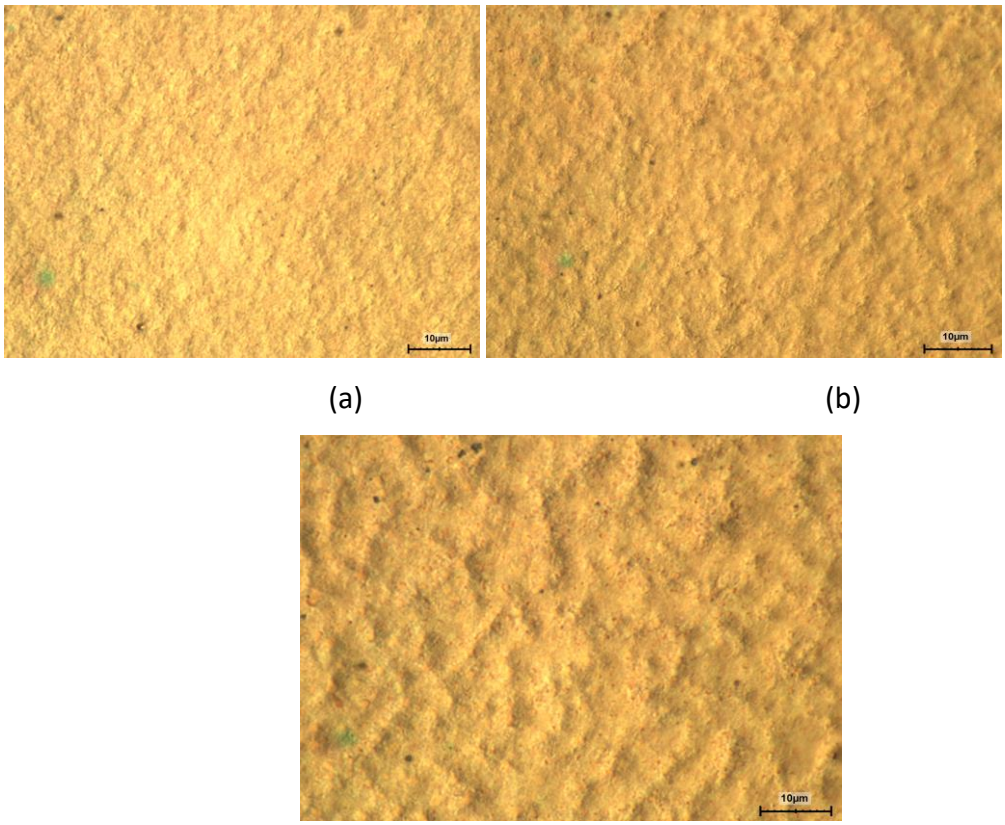

(a) (b)

(c)

Figure 3.14: Optical microscopic images of raw surfaces of the electropated copper: (a) 5 mA/cm^2, (b) 10 mA/cm^2, and (c) 20 mA/cm^2.

Moreover, the study of the surface roughness on the interior walls is of great importance. LIGA-processed samples were prepared separately to perform this study using AFM. For this study, the samples were diced across the open region in the copper microstructure so that interior metal walls can be seen with the cantilever tip when it is positioned 90^0 facing the sidewall towards the cantilever tip, as shown figure 13.15(a). Before performing the AFM measurements, the samples were cleaned thoroughly using

solvents to rid of all unwanted dust particles on the surfaces. The surface roughness profiles on sidewalls of the fabricated samples with different current density are shown in figure 13.15 (b), (c), and (d). The measured surface roughness in the range of 20-40 nm for 5 mA/cm^2 was well below the multiple times the skin-depth at operating frequency range, 360 GHz - 440 GHz.

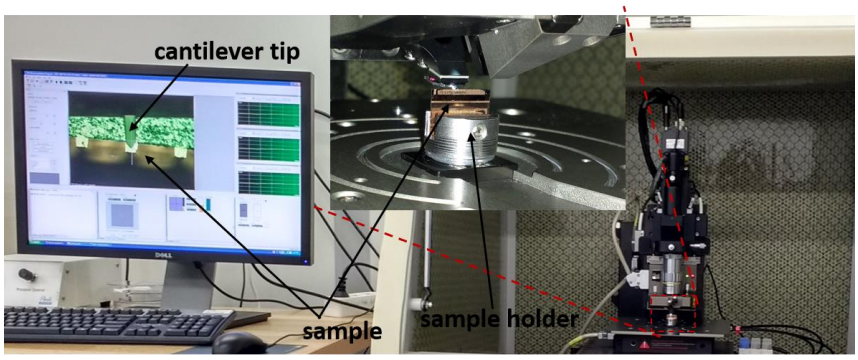

(a)

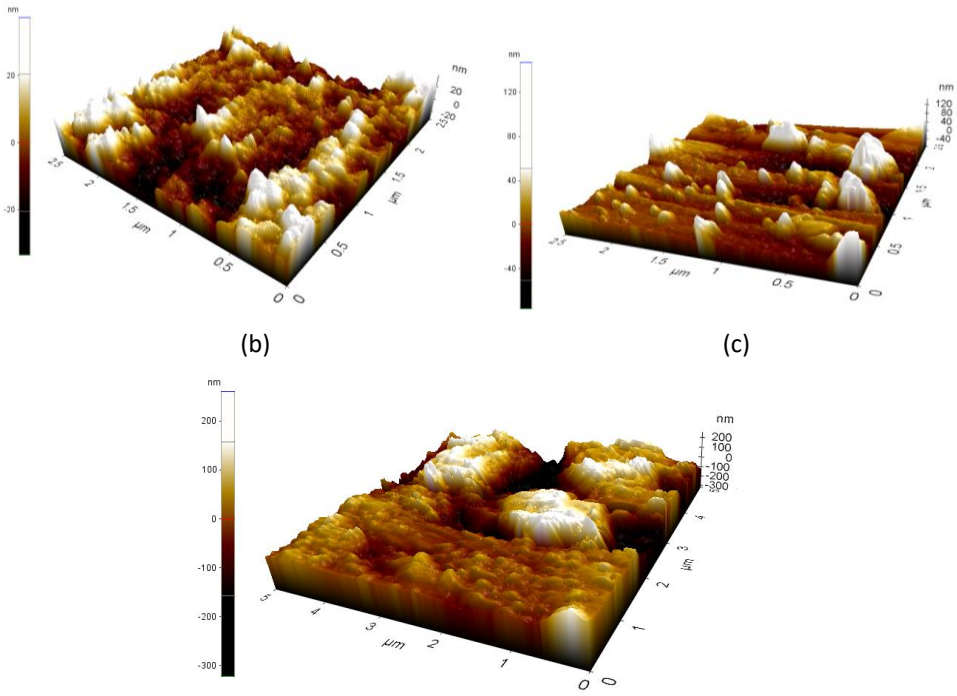

(b) (c)

(d)

Figure 3.15: AFM images of surface roughness of sidewalls: (a) sample being measured under AFM, (b) 5 mA/cm^2, (c) 10 mA/cm^2, and (d) 20 mA/cm^2.

3.2.4 Diffusion bonding

A simple technique of diffusion bonding was employed to connect the two copper structures face to face. For diffusion bonding, heat and force were simultaneously applied to bring the surfaces in contact; thereby causing an atomic motion to occur at the contact interface. This technique is quite popular in the semiconductor and MEMS industries where it is used for device packaging, connecting device layers in vertical integration, and integrating MEMS and CMOS ICs. It is also widely used in vacuum electron technology to assemble different tube parts. The essential parameters in diffusion bonding are temperature, pressure, bond time, bond ambient, and bond sequence. The bond sequence refers to the specific order in which the dices are heated, contacted, pressed and then unloaded. The samples with 50-µm-thick copper structures were prepared for the bonding experiments.

Prior to the bonding, the samples were immersed in 20% concentrated hydrochloric acid (HCl) for 20 sec to remove oxides on bonding surfaces since the oxidation of surfaces detrimental to the bonding process. First, a pair of samples, bottom and top structures, was aligned face-to-face. The aligned sample pair was subjected to heat in the vacuum chamber and provided the clamping force (3150 mbar) to ensure close contact. After bonding, the sample was annealed in Argon (Ar) environment at 400 ˚C for 45 min, with 26 ˚C/min ramping. The annealing step further improved the diffusion and recrystallization of copper atoms at the interface so that an enhanced bonding strength can be achievable.

A bonding at 400 °C produced a void-free bonding interface across the sample length, as shown in figure 3.16. For temperature above 400 °C, the metal interface acquired sufficient energy need for the interdiffusion at the contact interface. For the bonding temperature below 400 °C, such as at 250 °C, 300 °C, 350 °C, unbonded interfaces were noticed under SEM. This is due to the uneven distribution of pressure across the contact area. Therefore, it must be given more attention if the size of the samples is increased.

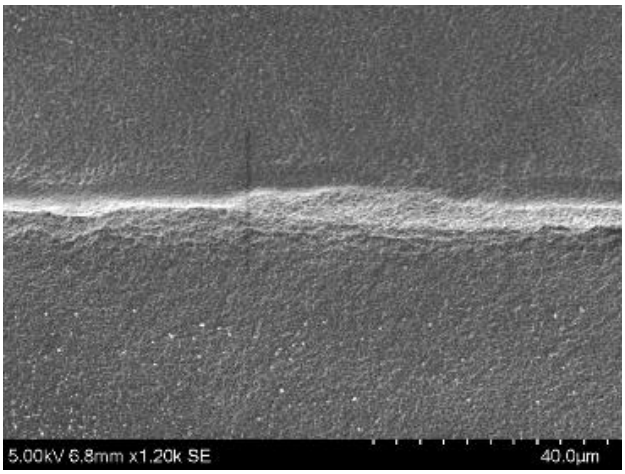

Figure 3.16: SEM image showing the bonding interface between copper parts at 400 ˚C bonding temperature.

The shear test was conducted using a Nordsondage 4000plus shear-tester for evaluating the bonding strength, is shown in figure 13.15(a). For this testing, the force-driving tip of the tester was positioned at a test height of 110 µm for the bonded interface and applied at a test speed of 10 µm/s. The test equipment determines the fracture point automatically by recording the force-time plot. The force at which fracture occurs is related to deboned energy according to the equation below (3.1).

$$\text{shear strength} = \frac{F_S}{A} \qquad (3.1)$$

Where F_s is the recorded shear force when the fracture occurs, and A is a bonded area. According to the test results, a maximum bonding strength of approximately 12 MPa was achieved when the bonding was processed at 400 ˚C. The trend of shear test results for different bonding temperatures is shown in figure 3.14 (b). For the TWT operation, the SWS requires to hold ultra-vacuum range, 10^{-7}-10^{-8} mbar. Therefore, the bonded sample must be performed the vacuum leak test. However, here, bonding experiments were conducted to have electrical contact for measuring the S-parameters.

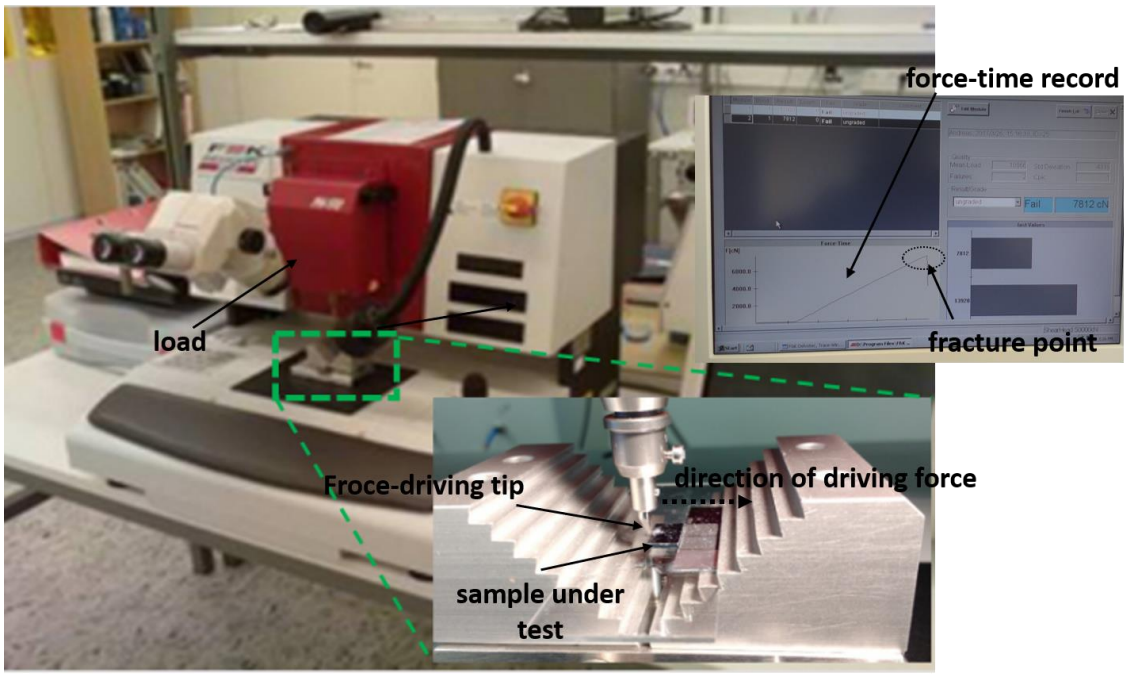

(a)

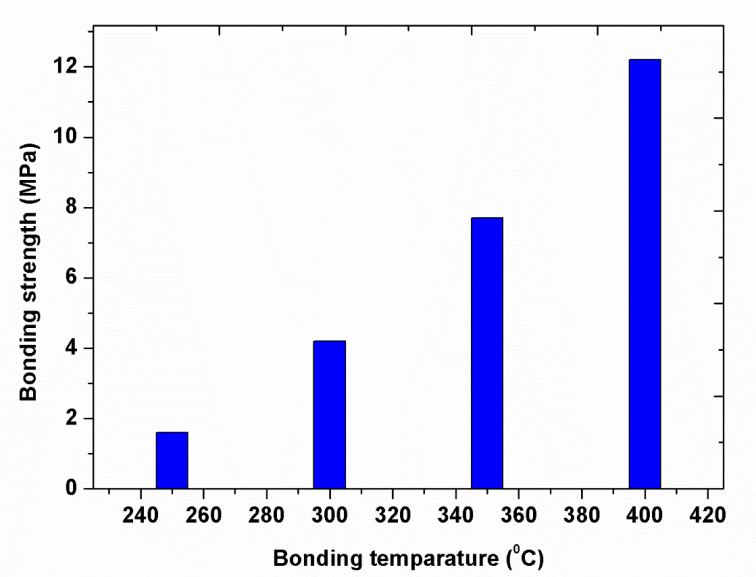

(b)

Figure 3.17: (a) Nordsondage 4000 plus shear-tester with sample being under test, (b)The trend of the bonding stregth between two copper structures is measured using the strear test.

Chapter 4

4 CNC-milled H-plane and E-plane loaded SWS and test results

The cold-test experimental results of H-plane and E-plane loaded SWS is reported in this chapter. For the experimental study, a scale-up model of the SWS at W-band (89 GHz – 101GHz) is designed and manufactured using CNC milling. Together with measurements, PiC simulations are also performed to demonstrate the W-band TWT performance using H-plane and E-plane loaded SWS. A modified sheet-beam geometry is employed to reduce the edge curling effect.

4.1 W-band SWS design

Chapter-2 reported the design and simulation of the H-plane and E-plane loaded SWS for 400-GHz TWT. The 400-GHz SWS was fabricated using the LIGA technique through fully controlled process conditions. Due to limited resources, testing the electromagnetic characteristics to the LIGA-fabricated SWS could not be done. As proof of concept, a scale-up model of the SWS is designed at a lower frequency (W-band). This scale-up model has features in the range of mm and sub-mm-range, which can be manufactured using advanced CNC milling. The LIGA technique is not very efficient for these feature sizes, in particular, for prototype device realization. This technique required optimization of a multitude of the lithography process conditions as well as requiring a time-consuming electroplating process to grow millimetre-thick for metal parts. In this case, the CNC milling is a more efficient, quicker and less expensive method; however, and it may not be preferable for mass production. The simulation models used for 400-GHz TWT design are adopted for the W-band TWT analysis. The frequency scaling law is not precisely applicable, as the SWS parameters are optimized to achieve desired amplifier performance and at the same time these parameters are selected in agreement with manufacturing feasibility. Table 4.1 is given the parameters of the SWS at the W-band (schematically is shown in figure 4.1). The tool size mainly depends on

the required feature size and the space between the parts being manufactured. The micron-sized parts demand expensive CNC tools. Therefore, during the design stage, the geometry dimensions are chosen to be done by low-cost CNC tools. Hence, it is also necessary for the design to select a sufficiently large value of the width-depth ratio of the parts. For instance, the space between corrugations in the x-direction is maintained in excess of 200 µm. The period length is determined by the operating beam voltage. For easing the manufacturing and operating tube at a modest voltage of about 21 kV, a period length of 1.1 mm is chosen.

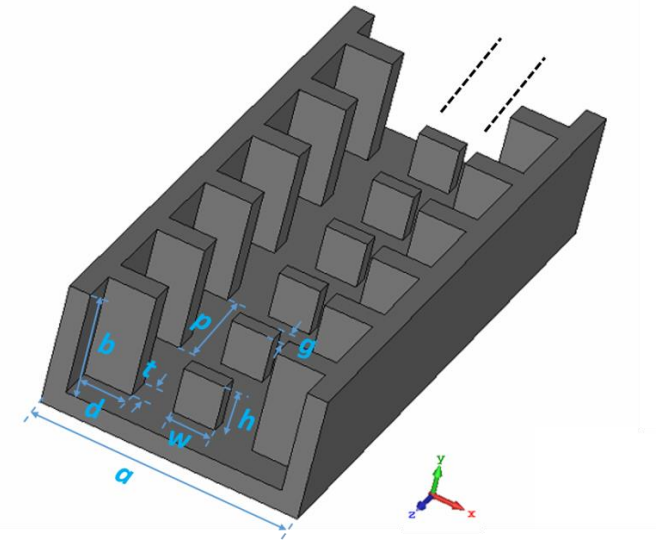

Figure 4.1: H-plane and E-plane loaded SWS for G-band TWT (top metal cover is not shown).

Table 4.1: Design parameters of the unit period of the SWS for W-band TWT.

Parameters	Dimension(mm)
a	2.45
b	1.75
p	1.1
w	0.6
g	0.31
h	0.46
d	0.535
t	0.58

From the Eigenmode simulations, the dispersion plot and field components are obtained. Figure 4.2 shows the fundamental mode dispersion curve superimposed with a beam-line. A frequency range of 80.4 GHz -104.2 GHz from the dispersion curve indicates a passband of the SWS in the fundamental mode. The interception of beam-line with dispersion curve assures the synchronism condition for beam-wave interaction. It covers a frequency of 87 GHz to 99 GHz, for the first space harmonics (phase=360^o to 540^o). Pierce interaction impedance is calculated using an equation (2.23). In the interaction impedance calculations, first spatial harmonics electric fields are used across a cross-section of 0.6 mm×0.3 mm which is located a 0.08 mm above the tip of the E-plane corrugation. To accommodate a high beam current at the same time maintaining a low current density, enlarged beam cross-section is needed. The larger beam current can yield more output power in the tube when it sees strong interaction fields during the beam-wave interaction. Hence, the width of beam cross-section is increased from the 0.6 mm to 1.0 mm. The interaction impedance for the beam width of 0.6 mm and 1.0 beam is shown in figure 4.3. For the enlarged beam cross-section, the interaction impedance was better than 1 Ohm over the frequency of interest, which is enough for obtaining the desired gain.

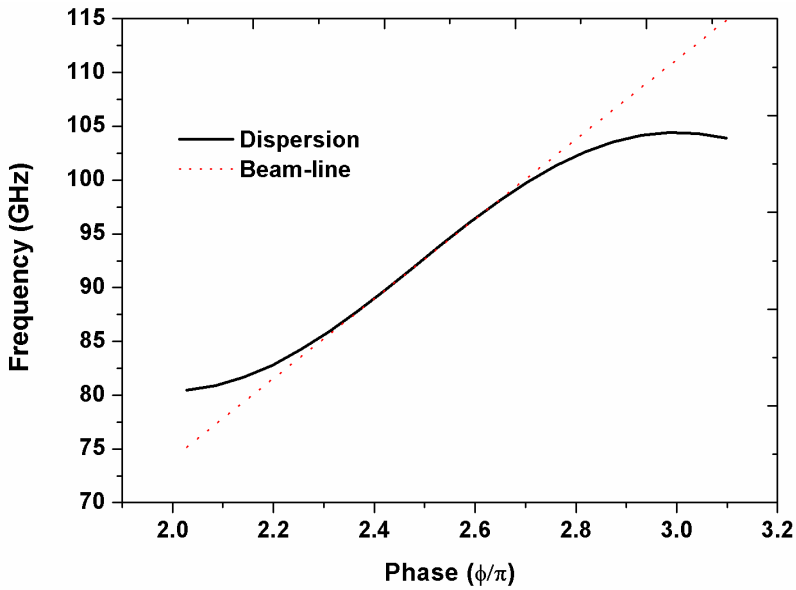

Figure 4.2: Dispersion curve of the SWS for W-band TWT.

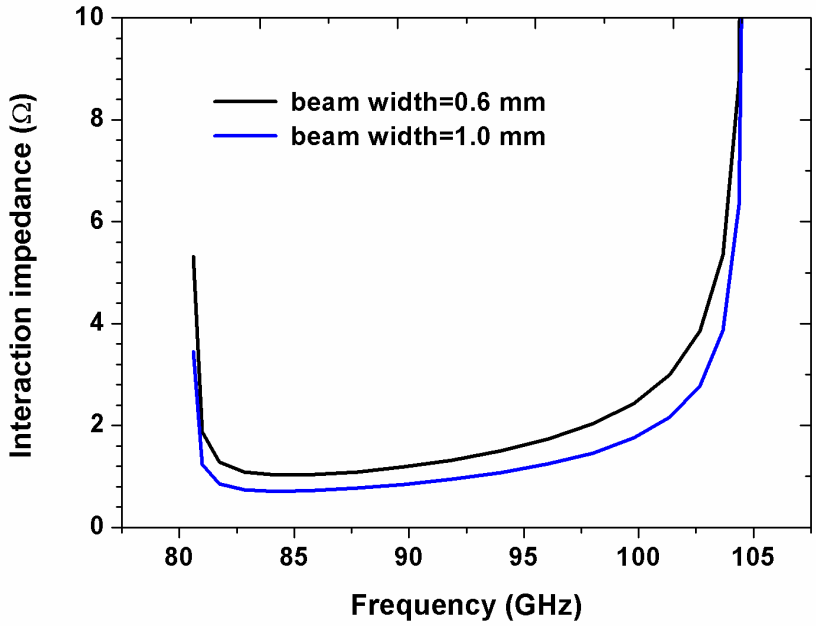

Figure 4.3: Interaction impedance for different sizes of beam cross-section.

The coupler design for input and output section is shown in figure 4.4 (a). This kind of tapering configuration helps for the smooth transition of electromagnetic fields components between TE_{10} and slow-wave mode inside the SWS. In addition, it takes advantage of using the full intrinsic bandwidth of the SWS. In the coupler design, the SWS is composed of nine periods of tapered corrugations at each input end and the output end of the SWS. The number of tapered corrugation periods and the width of the corrugations are optimized through simulations, taking into consideration of manufacturing feasibility and to achieve good wave matching behaviour. Ten periods of uniform corrugation sets are used in the interaction section.

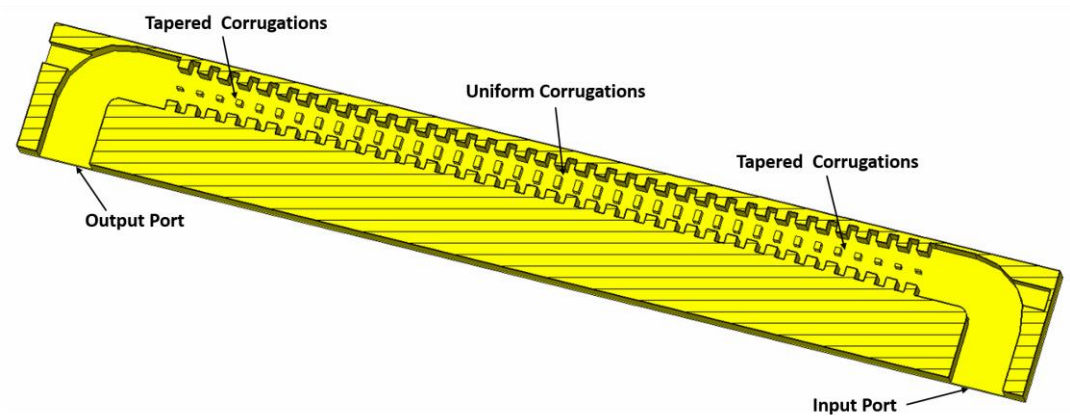

(a)

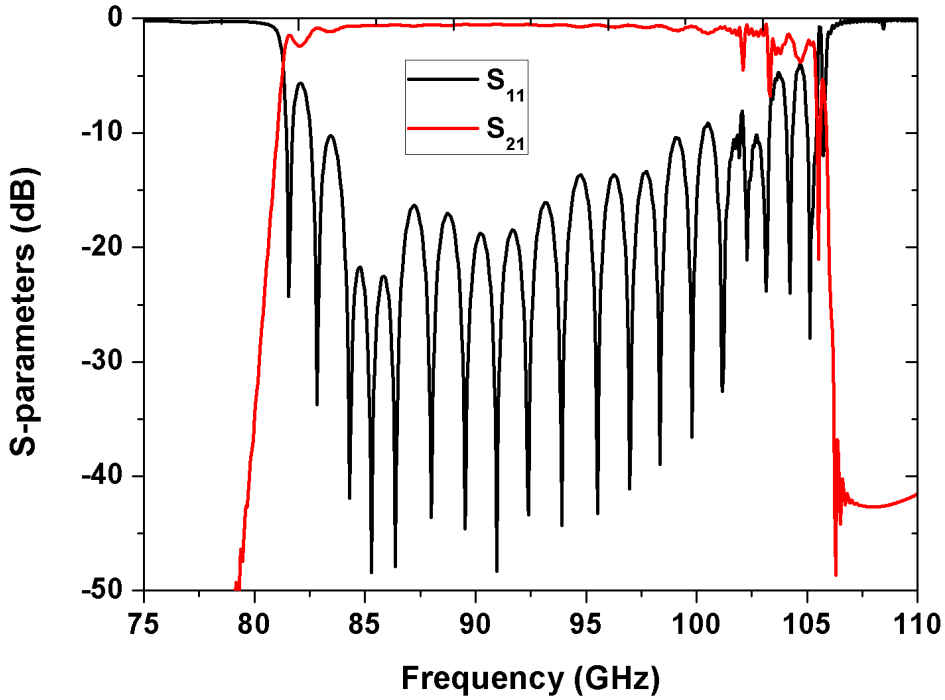

(b)

Figure 4.4: W-band H-plane and E-plane SWS with integrated coupler: (a) Design model, and (b) S-parameters.

Figure 4.4 (b) shows the S-parameters of the SWS along with the input and output coupler. The reflection coefficient, S_{11}, is better than -15 dB over a range of 84.5 GHz–98 GHz, which indicates excellent wave matching condition without any wave reflections back to the input. The transmission coefficient, S_{21}, shows excellent wave propagation characteristics (0.52 dB loss for 5.98×10^7 S/m) over the intrinsic bandwidth.

4.2 CNC milling and cold-test measurements

Advanced CNC mills are capable of producing complex 3D parts, which are larger than 500-micron features. When it is dealt with on a micron scale, for example, smaller than 500 microns features, the CNC milling undergoes challenges. The W-band SWS has to limit the manufacturing tolerance less than tens of microns.

The tolerances are limited by tool radius, tool vibrations, and spindle speed. The small radius tools often suffer from tool wear and tool deflection. The nano-scale surface finishing off of the interior parts is impossible to achieve with low-cost CNC tools. The design was made after accounting for these limitations and for inexpensive CNC tools.

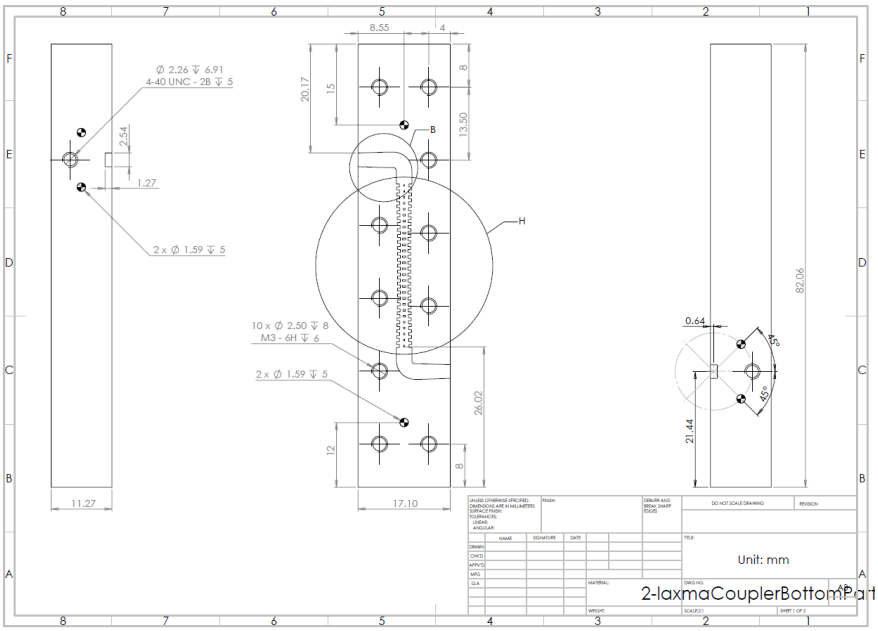

Figure 4.5: Drawings for CNC-milling.

The SWS drawings for CNC milling are shown in figure 4.5, which includes a 10-period length of SWS and 9 periods of tapered corrugation at each input and output section. The dimensions of the interior features were devised to make sure that there is enough room for tooling to mill small features, considering its width-to-height ratio. The placement of screw holes, alignment pins, and flange holes for the top metal cover was also designed to align to the bottom part. The two parts of the SWS were clamped tightly with screws and nuts for obtaining proper conduction path for RF signals transmitted through the device. This method makes assembly easy, and there was no problem of misalignment between parts. However, for hot test measurements, the parts must be attached for an ultra vacuum tight and vacuum compatible bonding methods must be employed.

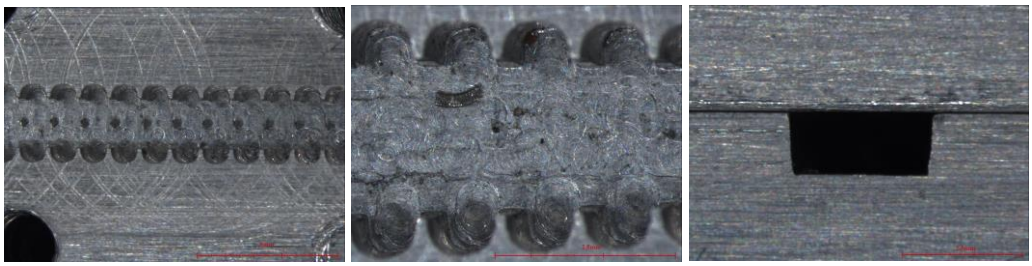

Figure 4.6: Optical microscope image of the first test structure on the aluminium block.

Initial milling trials were done in aluminium with a low-cost carbide tool. Specifications of the toll are 0.010" cutter diameter, 0.050" length of the cut, 0.050" overall reach and 3 flutes. The selection of the tool was made based on the space between them. The diameter of the tool must be less than the space between the parts to be made. The manufacturing and measurements were done with the facilities at Lancaster University. The initial trails produced a very poor quality of parts. The optical images revealed the manufacturing errors, such as missing small features of the E-plane corrugations in the coupler region, improper vertical profiles of the parts, curved 90^0 corners, and a very poor surface finish. The errors are due to the cutting force induced errors, servo errors, force and stress, and the geometrical deviation of the machine tool structure.

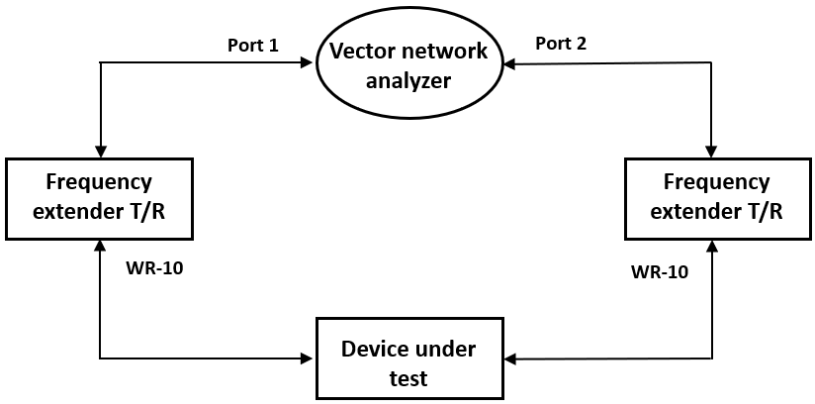

Figure 4.7: Schematic representation of the cold-test measurement setup using vector network analyzer.

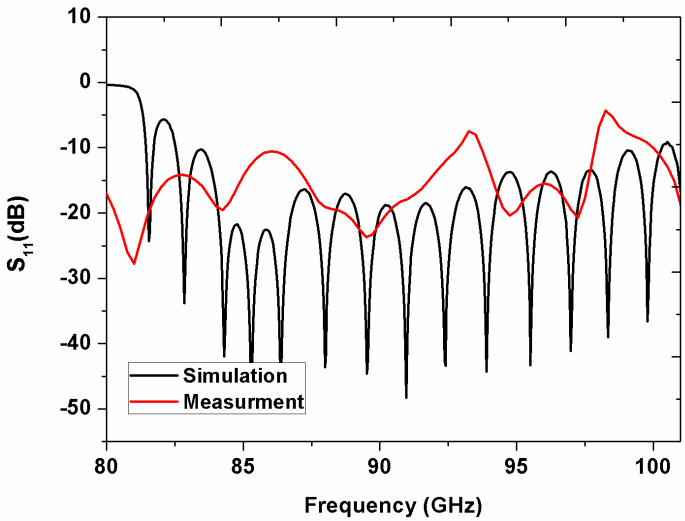

Figure 4.8: The first test results (S_{11}) of the SWS manufactured on aluminium.

Cold-test measurements (S-parameters) were done using a vector network analyser (VNA) with WR-10 port connectors (2.54 mm×1.27mm). Configuration of the cold-test measurement setup is shown in figure 4.7. Figure 4.8 shows the reflection characteristics of the SWS. The lower cut-off frequency approximately 65 GHz and upper cut-off frequency below the 110 GHz were obtained. The transmission loss was more the 10 dB. The measured results were not matched with the simulated data. The very poor transmission was due to the mismatch at the waveguide mating with the SWS and the defective features.

By controlling the machining process, an improvement in the quality of the features was achieved. The milling was done in copper alloy material (H62 grade). A tool radius of 0.1 mm was used and milling was done at a spindle speed of 42000 rpm. Excellent manufacturing parts were turned out with this milling process, as shown in figure 4.9.

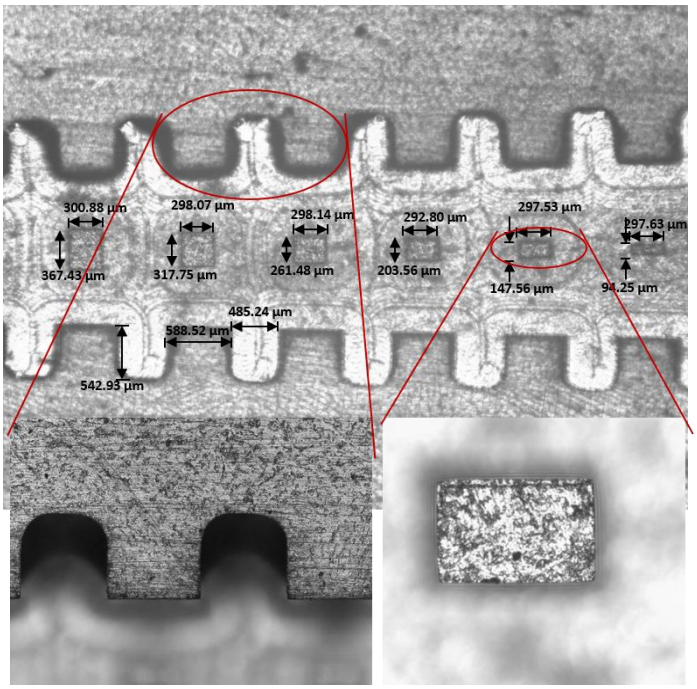

Figure 4.9: Optical microscope image of the SWS manufactured on copper alloy material.

The optical images of the manufactured parts confirmed that there were no missing parts and no damages to the small-sized corrugations in the coupler section. The manufactured parts were also produced with ideally 90^{o} corners inside the SWS. The accuracy of the dimensional tolerances was within the ±10 µm.

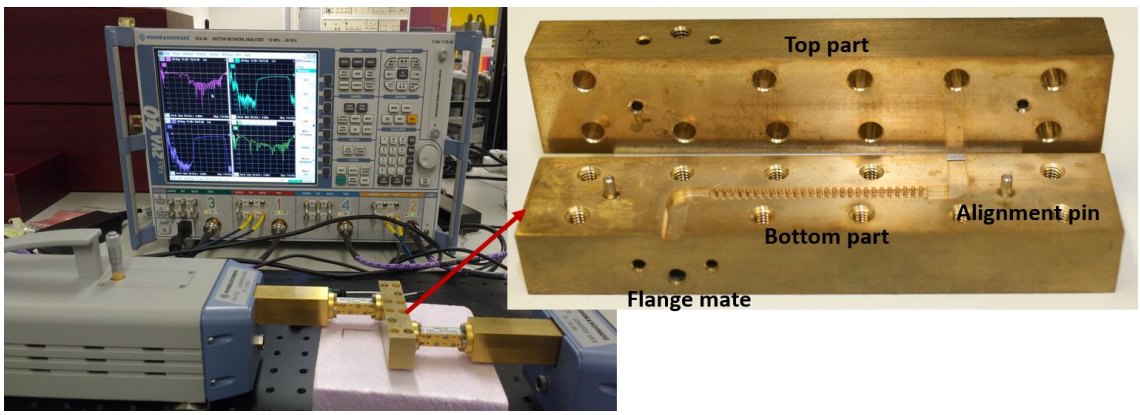

Figure 4.10: The CNC-milled SWS being tested using VNA (inserted camera photo of the SWS parts).

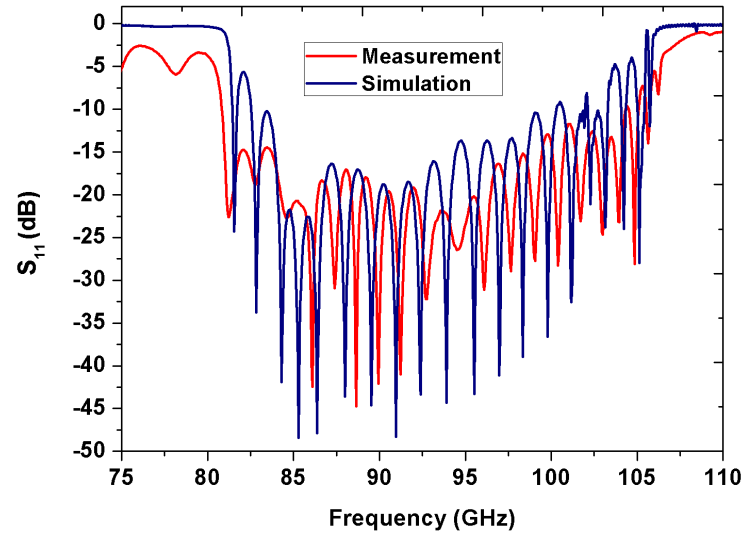

(a)

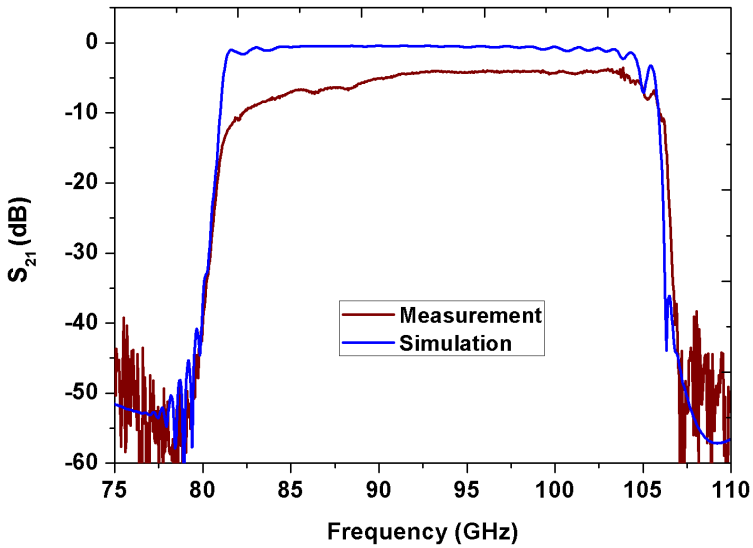

(b)

Figure 4.11: Test results of the SWS manufactured on copper alloy block and compared with simulations (σ =2.89×10^{-7} S/m): (a) reflection coefficient, S_{11}, and (b) transmission coefficient, S_{21}.

Before conducting the measurements, the manufacturing parts were ultrasonically cleaned sequentially in acetone, IPA and DI water, for digressing and getting rid of the machining bars and debrides. Following this, parts were dipped into the acid mixture solution to remove the surface oxides. It was verified from the test results that the lower and the upper cut off frequencies were an agreement with the simulation results,

except for a small difference of about 2 GHz. The reflection coefficient (S_{11}) was more than 15 dB over the operating bandwidth, 91 GHz - 98 GHz. The RF transmission loss in the SWS was measured at about 4.5 dB for a frequency of between 91 GHz and 98 GHz. The mismatch in transmission loss as compared with the simulation data was due to the rough surface finish of the internal metal walls, which was estimated at a roughness of multiple times of RF skin-depth (214 nm at 95 GHz for OFHC copper). Achieving the nano-level surface finish from the low-cost tool is nearly impossible. The presence of burrs and metal residues also contributed to some RF transmission loss. However, the fabrication and test results were significantly better than the initial test results on aluminium.

4.3 W-band TWT Particle-in-cell simulations

In order to demonstrate the W-band TWT performance based on the H-plane and E-plane loaded SWS, PiC simulations are performed for 85-periods interaction length. The simulations are done, by adopting the same modelling approach employed for 400-GHz TWT. The design of the interaction section and coupler section for this simulation follows the same parameters that are optimized in Eigenmode simulations and transient simulations in the earlier section of this chapter. The input and output RF ports are defined according to the WR-10 waveguide standards. The input port is excited with a small signal continuous sinusoidal wave and has 10 mW power. A uniform magnetic field of 0.9 T is applied for electron beam focusing. The beam voltage is predicted at about 21 kV, and 0.45 A beam current. The dimensions of the sheet-beam emitting surface (rectangular geometry) are 1.0 mm×0.30 mm, which is a distance of 0.23mm from the top of E-plane corrugation to the axis of the beam emission. It is calculated as a 150 mA/cm^2 current density for the beam parameters. Such a low current density gun makes development much easier. It also reduces the space charge effect during the beam-wave interaction.

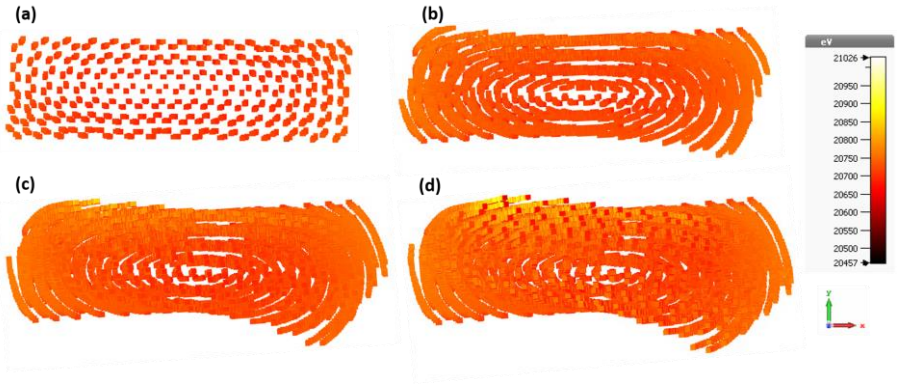

Figure 4.12 : Modulated sheet beam cross-section (rectangular geometry) SWS at instance along the SWS: (a) 0 mm, (b) 30.8 mm, (c) 61.6 mm, and (d) 82.5 mm.

The cross-section view of the modulated beam during the beam-wave interaction process for a 95 GHz input RF, at the different instances in length, is shown in figure 4.12. The curling edges of the beam cross-section are noticed as the beam progresses towards the end. The effect of the curling edges shows the worst beam shape as the electron particles intensified velocity modulation and bunching at the trailing end of the SWS. This curling edge is due to the $\vec{E} \times \vec{B}$ effect, where *E* is the space charge field, and *B* is the axial magnetic field. The $\vec{E} \times \vec{B}$ force is always along the equipotential line, and the electron will drift following the equipotential line. To minimize the $\vec{E} \times \vec{B}$ effects, the shape of the electron beam must match with the equipotential line. As shown in figure 4.13, a modified beam shape with round edges, such a shape can match with potential contour lines.

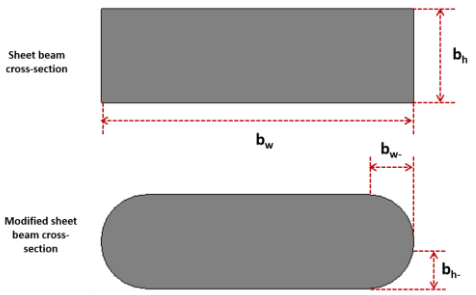

Figure 4.13: Electron particle emitting surface shapes.

The modified cross-section of the beam emitting surface is employed, which has curved edges in the rectangular beam emitting surface, b_{h-} = 0.14 mm and b_{w-}=0.14 mm.

Keeping the same beam current and voltage values used in case of rectangular beam simulation, the PiC simulations were performed with a modified beam cross-section.

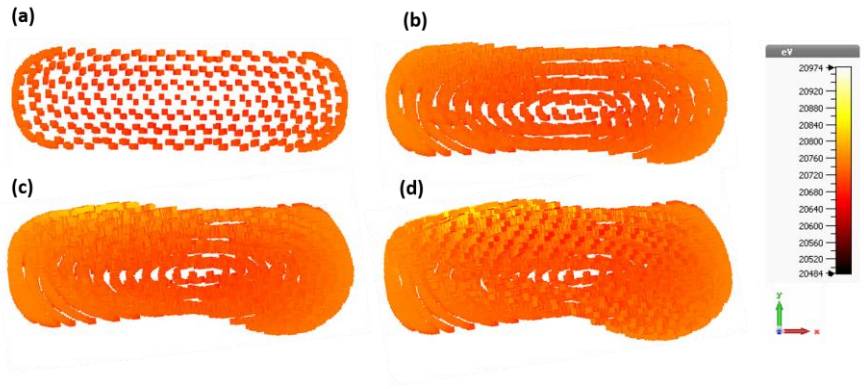

Figure 4.14: The modulated sheet beam cross-section of the modified beam geometry at instances along the SWS: (a) 0 mm, (b) 30.8 mm, (c) 61.6 mm, and (d) 82.5 mm.

Figure 4.14 shows the beam cross-section at different locations along the SWS length. In this case, it is evident that the beam edge curling effect has been mitigated. The elliptically shaped beam can also reduce the $\vec{E} \times \vec{B}$ impact, however, it will carry a lesser current than the rectangular beam shape.

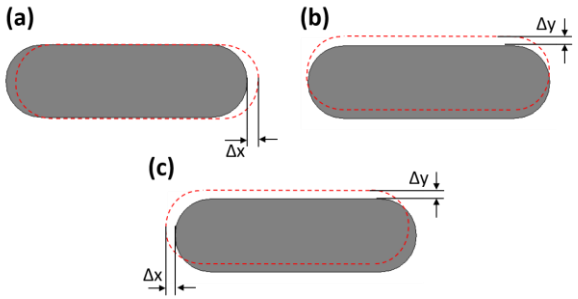

Figure 4.15: The topologies of beam offset: (a) horizontal offset, (b) vertical offset, and (c) horizontal and vertical offset.

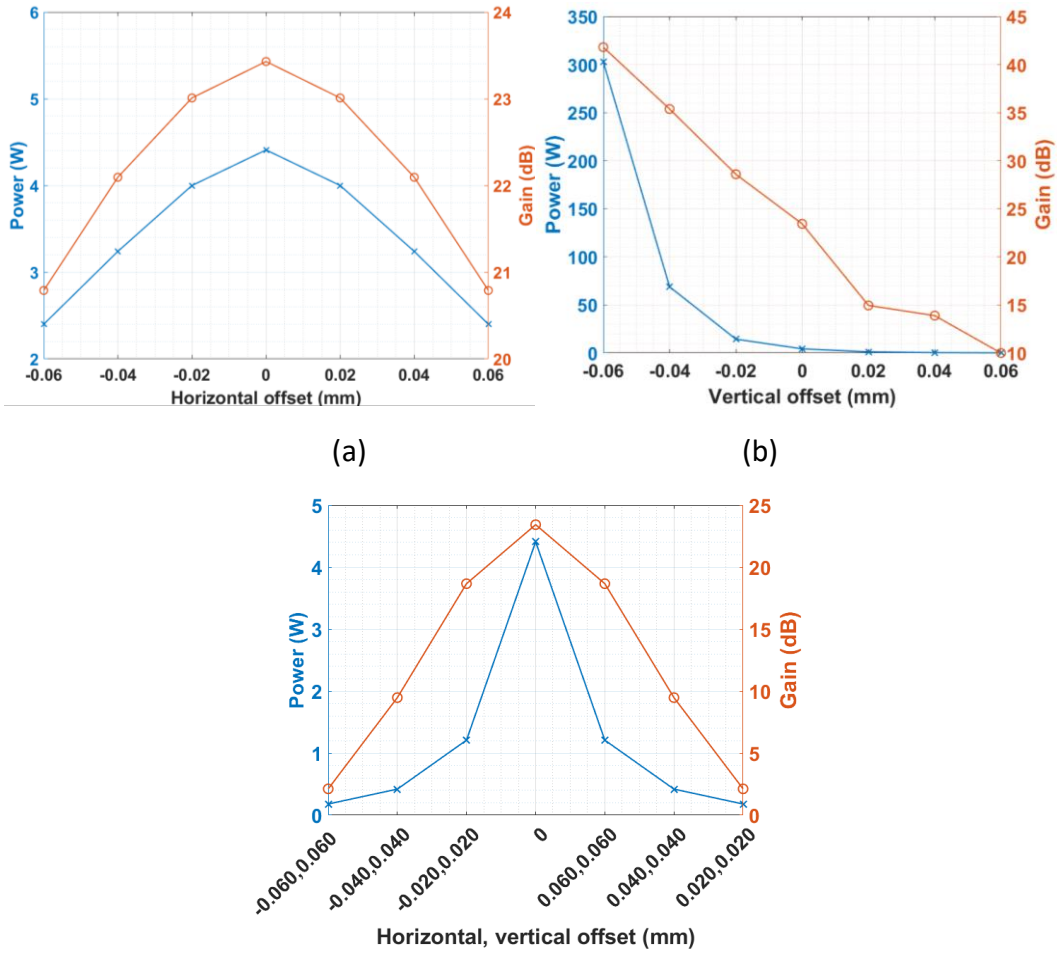

Figure 4.16: The change in power and gain vs. beam offset: (a) horizontal offset, (b) vertical offset, and (c) horizontal and vertical offset.

The electron gun and the SWS during the tube assembly can be misaligned. This misalignment causes dislocation of the beam waist when the electron beam enters the SWS. Therefore, in the PiC simulations, the effect of beam offset on the TWT power output is studied. The offset is considered along the horizontal (x-axis), vertical (y-axis), and both horizontal and vertical directions, as shown in figure 4.15. There is a significant change in the output power if there is a horizontal offset. For example, when the horizontal offset of 20 µm and 60 µm length, the percentage change in power is 9.3%, and 45.58%, respectively (figure 4.16(a)). It is also noted that for vertical offset moving away from the E-plane corrugation, the power output diminishes. On the other hand, if the vertical offset moves towards the E-plane corrugation top plane, an increased

output power is observed. This decreasing and increasing trend is due to the axial electric fields being denser near the E-plane corrugation top plane and it becoming weaker as they go away from the E-plane corrugation top. For example, the beam offset of 60 µm toward the E-plane corrugation caused a very large gain of 41.83 dB. As the beam gets closer to the E-plane corrugation, the modulated beam intercepts the E-plane corrugations, thereby losing beam energy. In the case of vertical beam offset of 60 µm away from the E-plane corrugation, an extremely weak beam-wave interaction and drop in output power to 0.2 W from 4.41 W occurred. Hence, the vertical offset must be precisely controlled.

To obtain a 3-dB bandwidth, simulations are performed for different frequency points covering the passband range The gain is about 24 dB from the 91 GHz to 98GHz, with 9 GHz 3-dB bandwidth, as shown in figure 4.17.

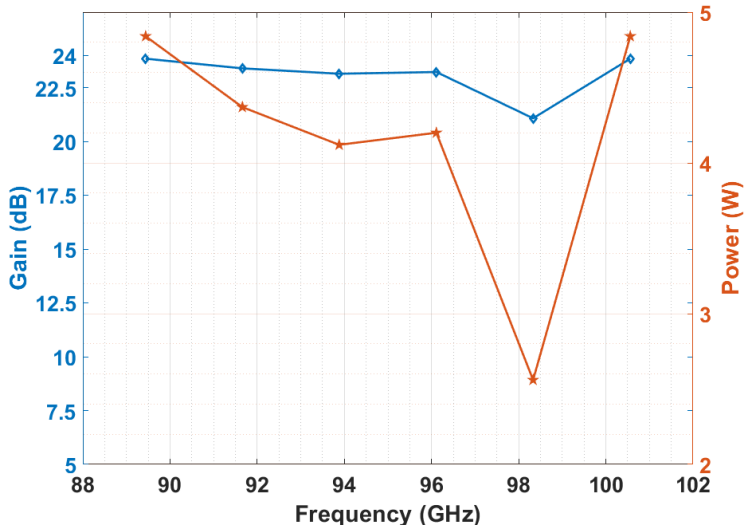

Figure 4.17: Small-signal gain and power vs. frequency of W-band TWT.

The two-section SWS with sever implementation can increase the output power levels and the gain of the TWT. If the TWT operates with a large input signal it can also produce higher output power. However, such large signal operation causes back-wave oscillations and harmonic oscillations in the tube, which made the device operation unstable. It is always preferred to operate any amplifier with a low input signal mode and in the linear condition.

Chapter 5

5 Conclusion and Future work

Conclusion:

The current market demands affordable and powerful signal generators and amplifiers capable of tens of watts or more of output power with at least one-octave bandwidth at frequencies beyond 90 GHz. Vacuum electron devices, particularly TWTs, can fulfil this need. The introduction of better SWSs could enhance the performance of the TWTs.

The main contributions of this research work are:

- A novel design of H-plane and E-plane loaded SWS for THz TWT amplifier was proposed.
- The performance metrics of this SWS (at 400-GHz band) was explored through the use of 3D electromagnetic solvers and PiC solver.
- An efficient coupler was devised for the H-plane and E-plane loaded SWS that is feasible to be fabricated as an integral part of the SWS using the same technological processes.
- Through interactive fabrication runs of the LIGA-like process and characterizing processes using metrological tools, we have developed well-controlled process protocols which can produce high-quality structures with tolerances within the limitations.
- Nano-scale surfaces roughness on the inner planes of the copper structure were achieved to meet the desired electromagnetic wave propagation at THz frequencies.
- A scaled-up version of the SWS for the W-band was designed and manufactured using the CNC milling. Measurement results verified the S-parameters of the SWS along with the couplers.

Future work:

In this thesis, the simulation and cold-test experimental results of the H-plane and E-plane loaded SWS for THz TWT amplifier have demonstrated the effectiveness of this SWS for sheet-beam technology in the high frequency of operation, which facilitates easy fabrication by the available microfabrication techniques. However, there are other parts of the TWT which must be designed, and some potential challenges that need to be addressed.

- The simulation considered the use of 17 kV, 20 mA electron gun, producing 100 µm × 60 µm rectangular beam. Such an electron gun manufacturing and/or procurement might be difficult. Because the electron gun with such parameters requires a sophisticated cathode, and assembly of the gun must follow very tight tolerances (accurate positioning of the cathode, focusing electrode, and anode) in order to meet the design requirements.
- Manufacturing of the magnetic focusing system using PPM configuration with 0.6 T integrated with the SWS pose challenges at the THz frequencies. A little drift in the magnetic field and pole piece placement causes significant change in the net magnetic field value that leads to the deterioration of the electron beam transmission and the possibility of intercepting the SWS.
- For improved efficiency of the tube, the multi-depressed collector is needed with an efficient cooling system. It is important to study the thermal analysis of the collector as well as the entire tube.
- There are several factors that need to be considered for building a complete tube; techniques required for attaching sub-parts, ultra-high vacuum pumping, vacuum windows and high voltage supply circuitry design.

References

[1] S. Dhillon *et al.*, "The 2017 terahertz science and technology roadmap," *Journal of Physics D: Applied Physics,* vol. 50, no. 4, p. 043001, 2017.

[2] M. Tonouchi, "Cutting-edge terahertz technology," *Nature photonics,* vol. 1, no. 2, p. 97, 2007.

[3] D. Dragoman and M. Dragoman, "Terahertz fields and applications," *Progress in Quantum Electronics,* vol. 28, no. 1, pp. 1-66, 2004.

[4] W. L. Chan, J. Deibel, and D. M. Mittleman, "Imaging with terahertz radiation," *Reports on progress in physics,* vol. 70, no. 8, p. 1325, 2007.

[5] H. B. Wallace, "Analysis of RF imaging applications at frequencies over 100 GHz," *Applied optics,* vol. 49, no. 19, pp. E38-E47, 2010.

[6] J. F. Federici, "Review of moisture and liquid detection and mapping using terahertz imaging," *Journal of Infrared, Millimeter, and Terahertz Waves,* vol. 33, no. 2, pp. 97-126, 2012.

[7] B. Ferguson and X.-C. Zhang, "Materials for terahertz science and technology," *Nature materials,* vol. 1, no. 1, p. 26, 2002.

[8] P. H. Siegel, "Terahertz technology in biology and medicine," *IEEE transactions on microwave theory and techniques,* vol. 52, no. 10, pp. 2438-2447, 2004.

[9] A. G. Davies, A. D. Burnett, W. Fan, E. H. Linfield, and J. E. Cunningham, "Terahertz spectroscopy of explosives and drugs," *Materials today,* vol. 11, no. 3, pp. 18-26, 2008.

[10] B. B. Hu and M. C. Nuss, "Imaging with terahertz waves," *Optics Letters,* vol. 20, no. 16, pp. 1716-1718, 1995.

[11] A. A. Penzias and C. A. Burrus, "Millimeter-Wavelength Radio-Astronomy Techniques," *Annual Review of Astronomy and Astrophysics,* vol. 11, no. 1, pp. 51-72, 1973.

[12] R. Appleby and H. B. Wallace, "Standoff Detection of Weapons and Contraband in the 100 GHz to 1 THz Region," *IEEE Transactions on Antennas and Propagation,* vol. 55, no. 11, pp. 2944-2956, 2007.

[13] R. J. Trew, "High-frequency solid-state electronic devices," *IEEE Transactions on Electron Devices,* vol. 52, no. 5, pp. 638-649, 2005.

[14] K. W. Brown, D. M. Gritters, and H. Kazemi, "W-and G-band solid state power combining," in *Compound Semiconductor Integrated Circuit Symposium (CSICS), 2015 IEEE*, 2015, pp. 1-4: IEEE.

[15] S. Francis and R. van Zyl, "Evaluating the microwave performance of a two domain GaN Gunn diode for THz applications," *Terahertz Sci. Technol,* vol. 8, no. 1, pp. 1941-7411, 2015.

[16] A. S. Hajo, O. Yilmazoglu, F. Kiippers, and A. Dadgar, "Reliability Improvement of High-Power THz GaN Gunn Sources for Active Imaging Systems," in *2018 43rd International Conference on Infrared, Millimeter, and Terahertz Waves (IRMMW-THz)*, 2018, pp. 1-2: IEEE.

[17] Z. Griffith, M. Urteaga, P. Rowell, and R. Pierson, "A 6–10 mW power amplifier at 290–307.5 GHz in 250 nm InP HBT," *IEEE Microwave and Wireless Components Letters,* vol. 25, no. 9, pp. 597-599, 2015.

[18] M. S. Vitiello, G. Scalari, B. Williams, and P. De Natale, "Quantum cascade lasers: 20 years of challenges," *Optics express,* vol. 23, no. 4, pp. 5167-5182, 2015.

[19] J. Hebling, K. Yeh, M. C. Hoffmann, and K. A. Nelson, "High-Power THz Generation, THz Nonlinear Optics, and THz Nonlinear Spectroscopy," *IEEE Journal of Selected Topics in Quantum Electronics,* vol. 14, no. 2, pp. 345-353, 2008.

[20] R. Abrams, B. Levush, A. Mondelli, and R. Parker, "Vacuum electronics for the 21st century," *IEEE Microwave magazine,* vol. 2, no. 3, pp. 61-72, 2001.

[21] R. K. Parker, R. H. Abrams, B. G. Danly, and B. Levush, "Vacuum electronics," *IEEE transactions on microwave theory and techniques,* vol. 50, no. 3, pp. 835-845, 2002.

[22] S. H. Gold and G. S. Nusinovich, "Review of high-power microwave source research," *Review of Scientific instruments,* vol. 68, no. 11, pp. 3945-3974, 1997.

[23] J. H. Booske, "Plasma physics and related challenges of millimeter-wave-to-terahertz and high power microwave generation," *Physics of plasmas,* vol. 15, no. 5, p. 055502, 2008.

[24] C. Paoloni *et al.*, "Design and fabrication of a 1 THz backward wave amplifier," *Terahertz Science and Technology,* vol. 4, pp. 149-163, 2011.

[25] N. E. Lindenblad, "High voltage generator," ed: Google Patents, 1942.

[26] R. Kompfner, "The traveling-wave tube as amplifier at microwaves," *Proceedings of the IRE,* vol. 35, no. 2, pp. 124-127, 1947.

[27] J. Pierce and L. M. Field, "Traveling-wave tubes," *Proceedings of the IRE,* vol. 35, no. 2, pp. 108-111, 1947.

[28] J. Pierce, "Theory of the beam-type traveling-wave tube," *Proceedings of the IRE,* vol. 35, no. 2, pp. 111-123, 1947.

[29] J. H. Booske *et al.*, "Vacuum electronic high power terahertz sources," *IEEE Transactions on Terahertz Science and Technology,* vol. 1, no. 1, pp. 54-75, 2011.

[30] Y. Zheng, D. Gamzina, and N. C. Luhmann, "0.2-THz Dual Mode Sheet Beam Traveling Wave Tube," *IEEE Transactions on Electron Devices,* vol. 64, no. 4, pp. 1767-1773, 2017.

[31] H. Liang *et al.*, "Integrated Planar Three-Beam Electron Optics System for 220-GHz Folded Waveguide TWT," *IEEE Transactions on Electron Devices,* vol. 65, no. 1, pp. 270-276, 2018.

[32] J.-x. Bao and B.-f. Wan, "The tungsten powder study of the dispenser cathode," *Applied Surface Science,* vol. 252, no. 16, pp. 5873-5876, 2006.

[33] J. Zhao *et al.*, "High current density and long-life nanocomposite scandate dispenser cathode fabrication," *IEEE Transactions on Electron Devices,* vol. 58, no. 4, pp. 1221-1228, 2011.

[34] N. Li, N. Luhmann Jr, D. Gamzina, G. Soekland, M. Banducci, and M. Gonzalez, "Study on the compositions of emission active materials and the emission properties of dispenser cathodes made from Scandia-doped powders," *Advanced Powder Technology,* vol. 27, no. 5, pp. 1933-1940, 2016.

[35] J. E. Atkinson *et al.*, "8.3: A high aspect ratio, high current density sheet beam electron gun," in *2010 IEEE International Vacuum Electronics Conference (IVEC)*, 2010, pp. 97-98.

[36] Y. Zheng, D. Gamzina, B. Popovic, and N. C. Luhmann, "Electron Beam Transport System for 263-GHz Sheet Beam TWT," *IEEE Transactions on Electron Devices,* vol. 63, no. 11, pp. 4466-4472, 2016.

[37] K. T. Nguyen, J. A. Pasour, T. M. Antonsen, P. B. Larsen, J. J. Petillo, and B. Levush, "Intense sheet electron beam transport in a uniform solenoidal magnetic field," *IEEE Transactions on Electron Devices,* vol. 56, no. 5, pp. 744-752, 2009.

[38] J. H. Booske and M. A. Basten, "Demonstration via simulation of stable confinement of sheet electron beams using periodic magnetic focusing," *IEEE transactions on plasma science,* vol. 27, no. 1, pp. 134-135, 1999.

[39] X. Shi *et al.*, "Theoretical and experimental research on a novel small tunable PCM system in staggered double vane TWT," *IEEE Transactions on electron devices,* vol. 62, no. 12, pp. 4258-4264, 2015.

[40] S. Coco, F. Emma, A. Laudani, S. Pulvirenti, and M. Sergi, "COCA: a novel 3-D FE simulator for the design of TWT's multistage collectors," *IEEE Transactions on Electron Devices,* vol. 48, no. 1, pp. 24-31, 2001.

[41] A. M. Latha and S. Ghosh, "An Asymmetric Highly Efficient Multistage Depressed Collector for Space TWTs," *IEEE Transactions on Electron Devices,* vol. 63, no. 5, pp. 2139-2144, 2016.

[42] P. R. R. Rao, S. Datta, V. Deshmukh, and L. Kumar, "Simulation of collectors for TWT including the effects of SEE using PIERCE," in *Vacuum Electronics Conference (IVEC), 2011 IEEE International*, 2011, pp. 509-510: IEEE.

[43] D. M. Springmann *et al.*, "Potential use of UNCD membranes as broadband vacuum windows at W-band frequencies," in *Vacuum Electronics Conference, 2008. IVEC 2008. IEEE International*, 2008, pp. 316-317: IEEE.

[44] C. L. Kory and J. A. Dayton, "Design of 650 GHz helical BWO using CST studio suite," in *Vacuum Electronics Conference, 2008. IVEC 2008. IEEE International*, 2008, pp. 392-393: IEEE.

[45] J. A. Dayton, C. L. Kory, G. T. Mearini, D. Malta, M. Lueck, and K. Gilchrist, "Applying microfabrication to helical vacuum electron devices for THz applications," in *Vacuum Electronics Conference, 2009. IVEC'09. IEEE International*, 2009, pp. 41-44: IEEE.

[46] J. A. Dayton, C. L. Kory, G. T. Mearini, D. Malta, M. Lueck, and C. A. Bower, "A 650 GHz helical BWO," in *Vacuum Electronics Conference, 2008. IVEC 2008. IEEE International*, 2008, pp. 396-397: IEEE.

[47] J. A. Dayton, C. L. Kory, G. T. Mearini, D. Malta, M. Lueck, and B. Vancil, "Fabrication and testing of the 0.650 THz helical BWO," in *Vacuum Electronics Conference (IVEC), 2012 IEEE Thirteenth International*, 2012, pp. 33-34: IEEE.

[48] C. L. Kory *et al.*, "95 GHz helical TWT design," in *Vacuum Electronics Conference, 2009. IVEC'09. IEEE International*, 2009, pp. 125-126: IEEE.

[49] J. A. Dayton, C. L. Kory, and G. T. Mearini, "Microfabricated mm-wave TWT platform for wireless Backhaul," in *Vacuum Electronics Conference (IVEC), 2015 IEEE International*, 2015, pp. 1-2: IEEE.

[50] C. Chua, S. Aditya, J. M. Tsai, M. Tang, and Z. Shen, "Microfabricated planar helical slow-wave structures based on straight-edge connections for THz vacuum electron devices," *Int. J. Terahertz Sci. Technol.,* vol. 4, no. 4, pp. 208-229, 2011.

[51] C. Chua *et al.*, "Microfabrication and characterization of W-band planar helix slow-wave structure with straight-edge connections," *IEEE Transactions on Electron Devices,* vol. 58, no. 11, pp. 4098-4105, 2011.

[52] C. Zhao, S. Aditya, and C. Chua, "Connected pair of planar helices with straight-edge connections for application in TWTs," *IEEE Transactions on Electron Devices,* vol. 61, no. 6, pp. 1692-1698, 2014.

[53] K. Swaminathan, C. Zhao, C. Chua, and S. Aditya, "Vane-loaded planar helix slow-wave structure for application in broadband traveling-wave tubes," *IEEE Transactions on Electron Devices,* vol. 62, no. 3, pp. 1017-1023, 2015.

[54] G. Dohler, D. Gagne, D. Gallagher, and R. Moats, "Serpentine waveguide TWT," in *1987 International Electron Devices Meeting*, 1987, pp. 485-488.

[55] D. B. Lyon and A. J. Theiss, "Litton folded-waveguide high-power millimeter-wave TWTs," in *Proceedings of 1994 IEEE International Electron Devices Meeting*, 1994, pp. 918-920.

[56] H.-J. Ha *et al.*, "Experimental Investigation of Ku-Band Folded Waveguide TWT," *International Journal of Infrared and Millimeter Waves,* vol. 20, no. 12, pp. 2099-2106, 1999.

[57] J. H. Booske *et al.*, "Accurate parametric modeling of folded waveguide circuits for millimeter-wave traveling wave tubes," *IEEE Transactions on Electron Devices,* vol. 52, no. 5, pp. 685-694, 2005.

[58] H. Gong *et al.*, "A 1-kW 32–34-GHz folded waveguide traveling wave tube," *IEEE Transactions on Plasma Science,* vol. 42, no. 1, pp. 8-12, 2014.

[59] J. Cai, J. Feng, Y. Hu, X. Wu, Y. Du, and J. Liu, "10 GHz bandwidth 100 watt W-band folded waveguide pulsed TWTs," *IEEE Microwave and Wireless Components Letters,* vol. 24, no. 9, pp. 620-621, 2014.

[60] J. Feng *et al.*, "Development of W-band folded waveguide pulsed TWTs," *IEEE Transactions on Electron Devices,* vol. 61, no. 6, pp. 1721-1725, 2014.

[61] Y. Hu *et al.*, "Design and experimental study of a widebandwidth W-band folded waveguide continuous-wave TWT," *IEEE Transactions on Plasma Science,* vol. 42, no. 10, pp. 3380-3386, 2014.

[62] X. Zhang *et al.*, "Design and Experimental Study of 250-W W-band Pulsed TWT With 8-GHz Bandwidth," *IEEE Transactions on Electron Devices,* vol. 64, no. 12, pp. 5151-5156, 2017.

[63] L. Wenqiang *et al.*, "Development of D-band continuous-wave folded waveguide traveling-wave tube," in *2015 IEEE International Vacuum Electronics Conference (IVEC)*, 2015, pp. 1-3.

[64] P. Pan *et al.*, "Development of G band folded waveguide TWTs," in *Vacuum Electronics Conference (IVEC), 2016 IEEE International*, 2016, pp. 1-2: IEEE.

[65] C. D. Joye *et al.*, "Demonstration of a high power, wideband 220-GHz traveling wave amplifier fabricated by UV-LIGA," *IEEE Transactions on Electron Devices,* vol. 61, no. 6, pp. 1672-1678, 2014.

[66] K. E. Kreischer, J. C. Tucek, M. A. Basten, and D. A. Gallagher, "220 GHz power amplifier testing at Northrop Grumman," in *2013 IEEE 14th International Vacuum Electronics Conference (IVEC)*, 2013, pp. 1-2.

[67] M. Basten *et al.*, "A multiple electron beam array for a 220 GHz amplifier," in *2009 IEEE International Vacuum Electronics Conference*, 2009, pp. 110-111.

[68] M. A. Basten, J. C. Tucek, D. A. Gallagher, and K. E. Kreischer, "233 GHz high Power amplifier development at Northrop Grumman," in *2016 IEEE International Vacuum Electronics Conference (IVEC)*, 2016, pp. 1-2.

[69] P. Hu *et al.*, "Development of a 0.32-THz Folded Waveguide Traveling Wave Tube," *IEEE Transactions on Electron Devices,* 2018.

[70] J. Tucek, K. Kreischer, D. Gallagher, R. Vogel, and R. Mihailovich, "Development and Operation of a 650 GHz Folded Waveguide Source," in *2007 IEEE International Vacuum Electronics Conference*, 2007, pp. 1-2.

[71] J. C. Tucek *et al.*, "A 100 mW, 0.670 THz power module," in *IVEC 2012*, 2012, pp. 31-32.

[72] M. A. Basten, J. C. Tucek, D. A. Gallagher, K. E. Kreischer, and R. Mihailovich, "A 0.85 THz vacuum-based power amplifier," in *IVEC 2012*, 2012, pp. 39-40.

[73] J. C. Tucek, M. A. Basten, D. A. Gallagher, and K. E. Kreischer, "0.850 THz vacuum electronic power amplifier," in *IEEE International Vacuum Electronics Conference*, 2014, pp. 153-154.

[74] G. Dohler, D. Gagne, D. Gallagher, and R. Moats, "Serpentine waveguide TWT," in *1987 International Electron Devices Meeting*, 1987, vol. 33, pp. 485-488.

[75] C. L. Kory, M. E. Read, R. L. Ives, J. H. Booske, and P. Borchard, "Design of Overmoded Interaction Circuit for 1-kW 95-GHz TWT," *IEEE Transactions on Electron Devices,* vol. 56, no. 5, pp. 713-720, 2009.

[76] E. J. Kowalski, M. A. Shapiro, and R. J. Temkin, "An Overmoded W-Band Coupled-Cavity TWT," *IEEE Transactions on Electron Devices,* vol. 62, no. 5, pp. 1609-1616, 2015.

[77] Y. Gong *et al.*, "A 140-GHz Two-Beam Overmoded Folded-Waveguide Traveling-Wave Tube," *IEEE Transactions on Plasma Science,* vol. 39, no. 3, pp. 847-851, 2011.

[78] S. Yan, W. Su, Y. Wang, and A. Xu, "Design and Theoretical Analysis of Multibeam Folded Waveguide Traveling-Wave Tube for Subterahertz Radiation," *IEEE Transactions on Plasma Science,* vol. 43, no. 1, pp. 414-421, 2015.

[79] S.-m. Yan, W. Su, and G.-l. Zhang, "Design and fabrication of a sub-millimeter multi-beam folded waveguide structure," *Optoelectronics Letters,* vol. 13, no. 1, pp. 33-37, 2017.

[80] K. T. Nguyen *et al.*, "Design Methodology and Experimental Verification of Serpentine/Folded-Waveguide TWTs," *IEEE Transactions on Electron Devices,* vol. 61, no. 6, pp. 1679-1686, 2014.

[81] D. Chernin *et al.*, "TWT stability for frequencies near a band edge," in *2013 IEEE 14th International Vacuum Electronics Conference (IVEC)*, 2013, pp. 1-2: IEEE.

[82] J. Cai, J. Feng, and X. Wu, "Folded Waveguide Slow Wave Structure With Modified Circular Bends," *IEEE Transactions on Electron Devices,* vol. 61, no. 10, pp. 3534-3538, 2014.

[83] S. Liu, J. Cai, J. Feng, and X. Wu, "Characteristics Study of 3pi Stopbands of Folded Waveguide Slow-Wave Structures in V-band Traveling-Wave Tubes," *IEEE Transactions on Electron Devices,* vol. 63, no. 3, pp. 1294-1298, 2016.

[84] J. He, Y. Wei, Y. Gong, W. Wang, and G. S. Park, "Investigation on a W Band Ridge-Loaded Folded Waveguide TWT," *IEEE Transactions on Plasma Science,* vol. 39, no. 8, pp. 1660-1664, 2011.

[85] Y. Wei *et al.*, "Novel W-Band Ridge-Loaded Folded Waveguide Traveling Wave Tube," *IEEE Electron Device Letters,* vol. 35, no. 10, pp. 1058-1060, 2014.

[86] M. Sumathy, K. J. Vinoy, and S. K. Datta, "Analysis of Ridge-Loaded Folded-Waveguide Slow-Wave Structures for Broadband Traveling-Wave Tubes," *IEEE Transactions on Electron Devices,* vol. 57, no. 6, pp. 1440-1446, 2010.

[87] Y. Hou *et al.*, "A Novel Ridge-Vane-Loaded Folded-Waveguide Slow-Wave Structure for 0.22-THz Traveling-Wave Tube," *IEEE Transactions on Electron Devices,* vol. 60, no. 3, pp. 1228-1235, 2013.

[88] M. Liao, Y. Wei, Y. Gong, J. He, W. Wang, and G. S. Park, "A Rectangular Groove-Loaded Folded Waveguide for Millimeter-Wave Traveling-Wave Tubes," *IEEE Transactions on Plasma Science,* vol. 38, no. 7, pp. 1574-1578, 2010.

[89] J. He and Y. Wei, "Study of the Slow-Wave Properties of a Rectangular Groove-Loaded Folded Waveguide for Millimeter Traveling-Wave Tubes," *IEEE Transactions on Plasma Science,* vol. 42, no. 1, pp. 55-61, 2014.

[90] H. Gong, G. Travish, J. Xu, Y. Wei, J. Feng, and Y. Gong, "High-Power Tunable Terahertz Radiation by High-Order Harmonic Generation," *IEEE Transactions on Electron Devices,* vol. 60, no. 1, pp. 482-486, 2013.

[91] D. J. Bates and E. L. Ginzton, "A Traveling-Wave Frequency Multiplier," *Proceedings of the IRE,* vol. 45, no. 7, pp. 938-944, 1957.

[92] Y. Tian *et al.*, "A Novel Slow-Wave Structure Folded Rectangular Groove Waveguide for Millimeter-Wave TWT," *IEEE Transactions on Electron Devices,* vol. 59, no. 2, pp. 510-515, 2012.

[93] Y. Tian, L. Yue, Q. Zhou, Y. Wei, Y. Wei, and Y. Gong, "Investigation on Sheet Beam Folded V-Shape Groove Waveguide for Millimeter-Wave TWT," *IEEE Transactions on Plasma Science,* vol. 44, no. 8, pp. 1363-1368, 2016.

[94] Y. Tian *et al.*, "Investigation of Ridge-Loaded Folded Rectangular Groove Waveguide Slow-Wave Structure for High-Power Terahertz TWT," *IEEE Transactions on Electron Devices,* vol. 65, no. 6, pp. 2170-2176, 2018.

[95] M. Mineo and C. Paoloni, "Corrugated rectangular waveguide tunable backward wave oscillator for terahertz applications," *IEEE Transactions on Electron Devices,* vol. 57, no. 6, pp. 1481-1484, 2010.

[96] C. D. Joye, J. P. Calame, M. Garven, D. Park, R. Bass, and B. Levush, "UV-LIGA and DRIE grating microfabrication and testing for sheet beam amplifiers at 220 GHz," in *Infrared Millimeter and Terahertz Waves (IRMMW-THz), 2010 35th International Conference on*, 2010, pp. 1-2: IEEE.

[97] D. J. Colin, P. C. Jeffrey, G. Morag, and L. Baruch, "UV-LIGA microfabrication of 220 GHz sheet beam amplifier gratings with SU-8 photoresists," *Journal of Micromechanics and Microengineering,* vol. 20, no. 12, p. 125016, 2010.

[98] M. Mineo and C. Paoloni, "Narrow corrugation rectangular waveguide for terahertz TWTs," *Electronics Letters,* vol. 46, no. 13, pp. 927-928, 2010.

[99] M. Mineo, A. Di Carlo, and C. Paoloni, "Analytical design method for corrugated rectangular waveguide SWS THz vacuum tubes," *Journal of Electromagnetic Waves and Applications,* vol. 24, no. 17-18, pp. 2479-2494, 2010.

[100] M. Mineo and C. Paoloni, "Comparison of THz backward wave oscillators based on corrugated waveguides," *Progress In Electromagnetics Research,* vol. 30, pp. 163-171, 2012.

[101] Y. M. Shin, L. R. Barnett, and N. C. Luhmann, "Phase-Shifted Traveling-Wave-Tube Circuit for Ultrawideband High-Power Submillimeter-Wave Generation," *IEEE Transactions on Electron Devices,* vol. 56, no. 5, pp. 706-712, 2009.

[102] Y.-M. Shin, A. Baig, L. R. Barnett, W.-C. Tsai, and N. C. Luhmann, "System design analysis of a 0.22-THz sheet-beam traveling-wave tube amplifier," *IEEE Transactions on Electron Devices,* vol. 59, no. 1, pp. 234-240, 2012.

[103] Y.-M. Shin, L. R. Barnett, and N. C. Luhmann Jr, "Strongly confined plasmonic wave propagation through an ultrawideband staggered double grating waveguide," *Applied Physics Letters,* vol. 93, no. 22, p. 221504, 2008.

[104] A. Baig *et al.*, "Design fabrication and RF testing of near-THz sheet beam TWTA," *IEEE Trans. Terahertz Sci. Technol.,* vol. 4, no. 4, pp. 181-207, 2011.

[105] A. Baig *et al.*, "Performance of a Nano-CNC Machined 220-GHz Traveling Wave Tube Amplifier," *IEEE Transactions on Electron Devices,* vol. 64, no. 5, pp. 2390-2397, 2017.

[106] C. Ruan *et al.*, "W -Band Multiple Beam Staggered Double-Vane Traveling Wave Tube With Broad Band and High Output Power," *IEEE Transactions on Plasma Science,* vol. 43, no. 7, pp. 2132-2139, 2015.

[107] X. Shi *et al.*, "Study on wideband sheet beam traveling wave tube based on staggered double vane slow wave structure," *IEEE Transactions on Plasma Science,* vol. 42, no. 12, pp. 3996-4003, 2014.

[108] Q.-L. Liu, Z.-C. Wang, P.-K. Liu, C.-H. Du, H.-Q. Li, and A.-Y. Xu, "A THz backward-wave oscillator based on a double-grating rectangular waveguide," *IEEE Transactions on Electron Devices,* vol. 60, no. 4, pp. 1463-1468, 2013.

[109] X. Xu *et al.*, "Sine waveguide for 0.22-THz traveling-wave tube," *IEEE Electron Device Letters,* vol. 32, no. 8, pp. 1152-1154, 2011.

[110] W. Xie, Z.-C. Wang, J. Luo, and D. Zhao, "A 3-D Large signal model for sheet beam traveling wave tubes," *IEEE Transactions on Electron Devices,* vol. 62, no. 3, pp. 1010-1016, 2015.

[111] M. Mineo and C. Paoloni, "Double-corrugated rectangular waveguide slow-wave structure for terahertz vacuum devices," *IEEE Transactions on Electron Devices,* vol. 57, no. 11, pp. 3169-3175, 2010.

[112] J. F. David, A. J. Durand, M. Mineo, and C. Paoloni, "Design of a terahertz cascade backward wave amplifier," *IEEE Transactions on Electron Devices,* vol. 61, no. 6, pp. 1715-1720, 2014.

[113] C. Paoloni and M. Mineo, "Double corrugated waveguide for G-band traveling wave tubes," *IEEE Transactions on Electron Devices,* vol. 61, no. 12, pp. 4259-4263, 2014.

[114] C. Paoloni, M. Mineo, M. Henry, and P. G. Huggard, "Double corrugated waveguide for ka-band traveling wave tube," *IEEE Transactions on Electron Devices,* vol. 62, no. 11, pp. 3851-3856, 2015.

[115] X. Li, X. Huang, S. Mathisen, R. Letizia, and C. Paoloni, "Design of 71–76 GHz Double-Corrugated Waveguide Traveling-Wave Tube for Satellite Downlink," *IEEE Transactions on Electron Devices,* vol. 65, no. 6, pp. 2195-2200, 2018.

[116] J. A. Dayton *et al.*, "Assembly and preliminary testing of the prototype 650 GHz BWO," in *Vacuum Electronics Conference, 2008. IVEC 2008. IEEE International*, 2008, pp. 394-395: IEEE.

[117] J. Dayton, G. Mearini, C. Kory, and C. Bower, "Fabrication of diamond-based 300 and 650 GHz BWOs," in *Vacuum Electronics Conference, 2007. IVEC'07. IEEE International*, 2007, pp. 1-2: IEEE.

[118] G. A. O. Vela, M. S. Miller, and R. W. Grow, "9.1: Terahertz backward-wave oscillator slow-wave circuits," in *Vacuum Electronics Conference (IVEC), 2010 IEEE International*, 2010, pp. 179-180: IEEE.

[119] W.-S. Chang and C.-Y. Chang, "A high slow-wave factor microstrip structure with simple design formulas and its application to microwave circuit design," *IEEE Trans. Microw. Theory Tech.,* vol. 60, no. 11, pp. 3376-3383, 2012.

[120] F. Shen *et al.*, "A novel V-shaped microstrip meander-line slow-wave structure for W-band MMPM," *IEEE Transactions on Plasma Science,* vol. 40, no. 2, pp. 463-469, 2012.

[121] F. Shen *et al.*, "140-GHz V-shaped microstrip meander-line traveling wave tube," *Journal of Electromagnetic Waves and Applications,* vol. 26, no. 1, pp. 89-98, 2012.

[122] F. Shen *et al.*, "Symmetric double V-shaped microstrip meander-line slow-wave structure for W-band traveling-wave tube," *IEEE Transactions on Electron Devices,* vol. 59, no. 5, p. 1551, 2012.

[123] G. Ulisse and V. Krozer, " W-band Traveling Wave Tube Amplifier Based on Planar Slow Wave Structure," *IEEE Electron Device Letters,* vol. 38, no. 1, pp. 126-129, 2017.

[124] L. B. Nguyen, T. M. Antonsen, and G. S. Nusinovich, "Planar slow-wave structure with parasitic mode control," *IEEE Transactions on Electron Devices,* vol. 61, no. 6, pp. 1655-1660, 2014.

[125] R. L. Ives, "Microfabrication of high-frequency vacuum electron devices," *IEEE Transactions on plasma science,* vol. 32, no. 3, pp. 1277-1291, 2004.

[126] S. Sengele, H. Jiang, J. H. Booske, C. L. Kory, D. W. Van der Weide, and R. L. Ives, "Microfabrication and characterization of a selectively metallized W-band meander-line TWT circuit," *IEEE Transactions on Electron Devices,* vol. 56, no. 5, pp. 730-737, 2009.

[127] N. M. Ryskin *et al.*, "Planar Microstrip Slow-Wave Structure for Low-Voltage V-Band Traveling-Wave Tube With a Sheet Electron Beam," *IEEE Electron Device Letters,* vol. 39, no. 5, pp. 757-760, 2018.

[128] E. Becker, W. Ehrfeld, P. Hagmann, A. Maner, and D. Münchmeyer, "Fabrication of microstructures with high aspect ratios and great structural heights by synchrotron radiation lithography, galvanoforming, and plastic moulding (LIGA process)," *Microelectronic engineering,* vol. 4, no. 1, pp. 35-56, 1986.

[129] D. Tolfree, "Microfabrication using synchrotron radiation," *Reports on Progress in Physics,* vol. 61, no. 4, p. 313, 1998.

[130] A. Rogner, J. Eicher, D. Munchmeyer, R.-P. Peters, and J. Mohr, "The LIGA technique-what are the new opportunities," *Journal of Micromechanics and Microengineering,* vol. 2, no. 3, p. 133, 1992.

[131] C. K. Malek and V. Saile, "Applications of LIGA technology to precision manufacturing of high-aspect-ratio micro-components and -systems: a review," *Microelectronics Journal,* vol. 35, no. 2, pp. 131-143, 2004.

[132] H. Seong-Tae *et al.*, "Investigations on a microfabricated FWTWT oscillator," *IEEE Transactions on Electron Devices,* vol. 52, no. 5, pp. 702-708, 2005.

[133] H. Seong-Tae *et al.*, "Experimental investigations on miniaturized high-frequency vacuum electron devices," *IEEE Transactions on Plasma Science,* vol. 33, no. 2, pp. 679-684, 2005.

[134] Y.-M. Shin *et al.*, "Microfabrication of millimeter wave vacuum electron devices by two-step deep-etch x-ray lithography," *Applied Physics Letters,* vol. 88, no. 9, p. 091916, 2006.

[135] L. Jian *et al.*, "SU-8-based deep x-ray lithography/LIGA," in *Micromachining and Microfabrication*, 2003, vol. 4979, p. 8: SPIE.

[136] O. V. Makarova, R. Divan, J. Tucek, K. Kreischer, and C.-M. Tang, "Fabrication of solid copper two-level waveguide circuits for a THz radar system by UV lithography," in *2016 IEEE International Vacuum Electronics Conference (IVEC)*, 2016, pp. 1-2: IEEE.

[137] A. Malekabadi and C. Paoloni, "UV-LIGA microfabrication process for sub-terahertz waveguides utilizing multiple layered SU-8 photoresist," *Journal of Micromechanics and Microengineering,* vol. 26, no. 9, p. 095010, 2016.

[138] H. Lorenz, M. Despont, N. Fahrni, J. Brugger, P. Vettiger, and P. Renaud, "High-aspect-ratio, ultrathick, negative-tone near-UV photoresist and its applications for MEMS," vol. 64, no. 1, pp. 33-39-33-39, 1998.

[139] H. Lorenz, M. Laudon, and P. Renaud, "Mechanical characterization of a new high-aspect-ratio near UV-photoresist," *Microelectronic Engineering,* vol. 41-42, pp. 371-374, 1998.

[140] J. Feng, D. Ren, H. Li, Y. Tang, and J. Xing, "Study of high frequency folded waveguide BWO with MEMS technology," *Terahertz Science and Technology,* vol. 4, no. 4, pp. 164-180, 2011.

[141] J. Cai *et al.*, "Development of W-band folded waveguide pulsed TWT," in *2013 IEEE 14th International Vacuum Electronics Conference (IVEC)*, 2013, pp. 1-2: IEEE.

[142] X. Fuqiang, D. Guifu, Z. Xiaolin, and C. Ping, "Design, fabrication and measurement of a novel 140 GHz folded waveguide based on SU-8 UV-LIGA technology," *Journal of Micromechanics and Microengineering,* vol. 25, no. 8, p. 085010, 2015.

[143] D. J. Colin, P. C. Jeffrey, T. N. Khanh, and G. Morag, "Microfabrication of fine electron beam tunnels using UV-LIGA and embedded polymer monofilaments for vacuum electron devices," *Journal of Micromechanics and Microengineering,* vol. 22, no. 1, p. 015010, 2012.

[144] P. Pan *et al.*, "Development of G band folded waveguide TWTs," in *2016 IEEE International Vacuum Electronics Conference (IVEC)*, 2016, pp. 1-2: IEEE.

[145] C. D. Joye *et al.*, "Demonstration of a High Power, Wideband 220-GHz Traveling Wave Amplifier Fabricated by UV-LIGA," *IEEE Transactions on Electron Devices,* vol. 61, no. 6, pp. 1672-1678, 2014.

[146] J. Tucek *et al.*, "220 GHz folded waveguide circuits for high power amplifiers," in *2009 IEEE International Vacuum Electronics Conference*, 2009, pp. 108-109: IEEE.

[147] Y.-M. Shin, L. R. Barnett, D. Gamzina, N. C. Luhmann Jr, M. Field, and R. Borwick, "Terahertz vacuum electronic circuits fabricated by UV lithographic molding and deep reactive ion etching," *Applied Physics Letters,* vol. 95, no. 18, p. 181505, 2009.

[148] C.-H. Ho, K.-P. Chin, C.-R. Yang, H.-M. Wu, and S.-L. Chen, "Ultrathick SU-8 mold formation and removal, and its application to the fabrication of LIGA-like micromotors with embedded roots," *Sensors and Actuators A: Physical,* vol. 102, no. 1, pp. 130-138, 2002/12/01/ 2002.

[149] H. Li, Y. Li, and J. Feng, "Fabrication of 340-GHz Folded Waveguides Using KMPR Photoresist," *IEEE Electron Device Letters,* vol. 34, no. 3, pp. 462-464, 2013.

[150] Y. Shin, D. Gamzina, L. R. Barnett, F. Yaghmaie, A. Baig, and N. C. Luhmann, "UV Lithography and Molding Fabrication of Ultrathick Micrometallic Structures Using a KMPR Photoresist," *Journal of Microelectromechanical Systems,* vol. 19, no. 3, pp. 683-689, 2010.

[151] K. E. Kreischer, J. C. Tucek, D. A. Gallagher, and R. E. Mihailovich, "Operation of a compact, 0.65 THz source," in *2008 33rd International Conference on Infrared, Millimeter and Terahertz Waves*, 2008, pp. 1-2: IEEE.

[152] J. C. Tucek, M. A. Basten, D. A. Gallagher, and K. E. Kreischer, "220 GHz power amplifier development at Northrop Grumman," in *IVEC 2012*, 2012, pp. 553-554: IEEE.

[153] J. C. Tucek, M. A. Basten, D. A. Gallagher, and K. E. Kreischer, "Testing of a 0.850 THz vacuum electronic power amplifier," in *2013 IEEE 14th International Vacuum Electronics Conference (IVEC)*, 2013, pp. 1-2: IEEE.

[154] D. K. Chung, K. H. Lee, J. Jeong, and C. N. Chu, "Machining characteristics on electrochemical finish combined with micro EDM using deionized water," *International Journal of Precision Engineering and Manufacturing,* journal article vol. 15, no. 9, pp. 1785-1791, 2014.

[155] H. S. Lim, Y. S. Wong, M. Rahman, and M. K. Edwin Lee, "A study on the machining of high-aspect ratio micro-structures using micro-EDM," *Journal of Materials Processing Technology,* vol. 140, no. 1, pp. 318-325, 2003.

[156] D. Gamzina *et al.*, "Nanoscale Surface Roughness Effects on THz Vacuum Electron Device Performance," *IEEE Transactions on Nanotechnology,* vol. 15, no. 1, pp. 85-93, 2016.

[157] Q. Zhou *et al.*, "Development of a 0.22THz folded waveguide travelling wave tube," in *2015 IEEE International Vacuum Electronics Conference (IVEC)*, 2015, pp. 1-2: IEEE.

[158] T. Horn *et al.*, "Additively manufactured WR-10 copper waveguide," in *2018 IEEE International Vacuum Electronics Conference (IVEC)*, 2018, pp. 409-410: IEEE.

[159] R.-J. Hwu, D. K. Kress, S. V. Judd, and L. P. Sadwick, "3D printing additive manufacturing of W-band vacuum tube parts," in *Vacuum Electronics Conference (IVEC), 2016 IEEE International*, 2016, pp. 1-2: IEEE.

[160] D. Gamzina *et al.*, "Additive vacuum electronics: Electron beam melting of copper," in *Vacuum Electronics Conference (IVEC), 2017 Eighteenth International*, 2017, pp. 1-2: IEEE.

[161] A. M. Cook, C. D. Joye, J. P. Calame, and D. K. Abe, "3D-printed mold electroforming for microfabrication of W-band TWT circuits," in *Vacuum Electronics Conference (IVEC), 2017 Eighteenth International*, 2017, pp. 1-2: IEEE.

[162] A. M. Cook, C. D. Joye, J. P. Calame, and D. K. Abe, "3D-printed mold electroforming for microfabrication of W-band TWT circuits," in *2017 Eighteenth International Vacuum Electronics Conference (IVEC)*, 2017, pp. 1-2: IEEE.

Journal paper 1

H-plane and E-plane loaded rectangular slow-wave structure for terahertz TWT amplifier

Laxma Reddy Billa, Muhammad Nadeem Akram, and Xuyuan Chen

IEEE Transaction on electron devices, volume 63, number 4, page 1722-1727

Papers omitted from the online publication due to publisher's restrictions

Journal paper 2

Improved design and microfabrication of H-plane and E-plane loaded rectangular slow-wave structure for THz TWT amplifier

Laxma Reddy Billa, Xianbao Shi, Muhammad Nadeem Akram, and Xuyuan Chen

IEEE Transaction on electron devices, Volume 64, number 4, page 1722-1727

Papers omitted from the online publication due to publisher's restrictions

Journal paper 3

UV-LIGA microfabricated terahertz slow-wave structures for vacuum electronics devices using KMPR photoresist

Laxma Reddy Billa, Muhammad Nadeem Akram, and Xuyuan Chen

IOP Journal of Micromechanics and Microengineering (manuscript submitted)

Papers omitted from the online publication due to publisher's restrictions

Journal paper 4

H- and E-plane loaded slow-wave structure for W-band TWT

Laxma Reddy Billa, Muhammad Nadeem Akram, Claudio Paoloni, and Xuyuan Chen

IEEE Transaction on electron devices (manuscript submitted)

Papers omitted from the online publication due to publisher's restrictions

Doctoral dissertation no. 49
2019
—

Simulation and microfabrication of MEMS vacuum electronic devices for terahertz technology

Dissertation for the degree of PhD

—

Laxma Reddy Billa

—

ISBN: 978-82-7860-398-7 (print)
ISBN: 978-82-7860-399-4 (online)

usn.no